research report

Influence of Support Attachment Pattern on the Out-of-Plane Buckling Capacity of Steel Deck

RESEARCH REPORT RP23-02

June 2023

American Iron and Steel Institute

DISCLAIMER

The material contained herein has been developed by researchers based on their research findings and is for general information only. The information in it should not be used without first securing competent advice with respect to its suitability for any given application. The publication of the information is not intended as a representation or warranty on the part of the American Iron and Steel Institute or of any other person named herein, that the information is suitable for any general or particular use or of freedom from infringement of any patent or patents. Anyone making use of the information assumes all liability arising from such use.

Influence of support attachment pattern on the out-of-plane buckling capacity of steel deck

Report submitted to the American Iron and Steel Institute on June 23rd, 2023

Divyansh R. Kapoor

Graduate Research Assistant and Ph.D. Candidate, University of Massachusetts Amherst

Brian Bogh

Industry advisor and Senior Research Engineer, NUCOR/Vulcraft Group

Kara D. Peterman

Associate Professor, University of Massachusetts Amherst

American Iron and Steel Institute

NUCOR VULCRAFT

CSC CANAM STEEL CORPORATION

UMass Amherst College of Engineering

Acknowledgments

This report was prepared on a small project fellowship from the American Iron and Steel Institute titled “Impact of Attachment Pattern on Out-of-Plane Buckling Strength in Steel Deck.” The steel deck for testing was donated by Nucor/Vulcraft Group and Canam Steel Corporation. The authors gratefully acknowledge the financial support provided by all our sponsors. Any opinions, findings, conclusions, or recommendations expressed in this publication are those of the authors and do not necessarily reflect the views of the sponsors.

The authors gratefully acknowledge Brian Bogh, Senior Research Engineer, Nucor/Vulcraft Group, who served as the industry advisor on the project and provided valuable technical feedback throughout the various phases of the project. The authors would also like to acknowledge the support of Mr. Mark Gauthier, Structural Labs Manager, UMass Amherst, for his guidance and help with the fabrication and testing of the specimens. Special thanks also go out to Brian Shea, Graduate Research Assistant at UMass Amherst, who assisted with the fabrication and testing of the specimens.

Table of contents

Acknowledgments 1
Table of contents 2
`List of figures 4
List of tables 7
1. Introduction 8
2. Relevant works 9
2.1 Easley (1975) 9
2.2 Wright and Hossain (1997) 10
2.3 Nunna (2011) 11
3 Design limit states and resultant design space 12
3.1 Connection limit states 12
3.1.1 Individual support and sidelap fastener strength 13
3.1.2 Edge connection (S_{ne}) 13
3.1.3 Interior connection (S_{ni}) 13
3.1.4 Corner connection (S_{nc}) 13
3.1.5 Connections along perpendicular edge (S_{np}) 14
3.1.6 Sample connection limit states 14
3.2 Panel buckling limit states (S_{nb}) 15
3.2.1 Global (Out-of-plane) buckling (S_{no}) 15
3.2.2 Local buckling (Web crippling) (S_{nl}) 15
3.3 Resultant design space 15
4 Experimental test matrix and measured properties 17
4.1 Test matrix 17
4.2 Measured properties and dimensions 17
5 Experimental Setup 19
5.1 Test Frame 19
5.2 Sensor locations 19
5.3 Specimen fabrication 20
5.4 Loading protocol and data acquisition 22
6 Results 23
6.1 Summary of experimental results 23
6.1.1 Estimation of peak load (P_{max}) and corrected displacement 27

6.1.2 Estimation of load (P_{nb}) and displacement (Δ_{nb}) level corresponding with onset of out-of-plane buckling 27
6.1.3 Estimation of Stiffness (G') 29
6.2 36-7 Fully attached specimen 30
6.3 36-5 Intermediately attached specimen 30
6.4 36-4 Skip pattern specimen 32
6.5 Influence on buckling capacity and displacement 32
6.6 Influence on stiffness 33
6.7 Influence on end-warping behavior 33
7 Experimental program conclusions 35
8 Finite element analysis (FEA) expansion 36
8.1 Numerical modelling matrix 36
8.2 FEA modelling methodology 36
8.2.1 Model geometry and material properties 36
8.2.2 Interactions and constraints 39
8.2.3 Meshing details 40
8.2.4 Solvers, boundary conditions, and applied loading/displacement 40
8.3 Comparison with experimental data 41
8.4 Parametric study summary results 47
8.5 Comparison with predictive methods 50
8.5.1 Comparison of predicted capacity from AISI S310 - 20 (AISI 2020) with ultimate capacity from FEA 50
8.5.2 Comparison of predicted stiffness from AISI S310 -20 (AISI 2020) with stiffness from FEA 51
8.6 FEA parametric study conclusions 52
9 Recommended future works 53
References 54
A. Appendix A – Test rig 55
B. Appendix B – Sensor layout and loading protocol 60
C. Appendix C – Detailed per-specimen experimental results 62
D. Appendix D – Estimation of P_{nb} 83
E. Appendix E – Detailed numerical results 85

List of figures

Figure 1: Diaphragm components and typical attachment patterns 8
Figure 2: Typical corrugation dimensions for Type B Deck (Luttrell 2015) 9
Figure 3: Summary of results of Easley test program (Adapted from Easley 1975) 10
Figure 4: Evaluated boundary conditions (adapted from Wright and Hossain 1997) 11
Figure 5: Comparison of existing equations 11
Figure 6: Comparison of current equation with historical test data 12
Figure 7: Connection limit states for 22 gauge Type B Deck 14
Figure 8: Resultant design space for panel buckling tests 16
Figure 9: Measured thickness (left) and supported lengths (right) 18
Figure 10: Cantilever test rig 19
Figure 11: Sensor locations on specimen 20
Figure 12: Perimeter framing members 21
Figure 13: Typical sidelap (VSC-II), support (Hex-14), and edge connections (Hex-14) 21
Figure 14: Construction platform for sidelap connections. The Punchlok – II tool was supported by the crane during specimen fabrication 22
Figure 15: Typical monotonic loading protocol (Δ_{max} = 3in) 22
Figure 16: Unprocessed actuator force displacement results summary 23
Figure 17: Processed force-shear displacement results summary 24
Figure 18: Summary of sensor force-out-of-plane displacement (Δ_z) 26
Figure 19: Estimation of corrected displacement [Adapted from AISI S907 (AISI 2017)] 27
Figure 20: Determining time step corresponding with onset of out-of-plane buckling. Bottom three plots represent insets of corresponding top three plots. 28
Figure 21: Determining force level (P_{nb}) corresponding with time step 28
Figure 22: (a) Determining displacement level Δ_{nb} (b)verification of P_{nb} 29
Figure 23: Estimation of diaphragm stiffness, G' (AISI 2017) 29
Figure 24: Observed post-peak failure modes in the 36/7 repititions: (a) 36/7-R1 (b) 36/7-R2 (c) 36/7-R3 30
Figure 25: Observed ultimate failure modes in the 36/5 repititions: (a) 36/5-R1 (b) 36/5-R2 (c) 36/5-R3 31
Figure 26: (a) Proper vs (b) improper sidelap connection at failure 31

Figure 27: Select ultimate failure modes in the 36/4 repititions: (a) 36/4-R1 – Pull over (b) 36/4-R2 – Bearing (c) 36/4-R3 – Edge tearout (d) 36/4-R3 – Tilting 32
Figure 28: Typical end-warping behavior observed in the 36/7 specimens 33
Figure 29: Typical end-warping behavior observed in the 36/5 specimens 34
Figure 30: Typical end-warping beavior observed in the 36/4 specimens 34
Figure 31: FEA idealization of test specimen 37
Figure 32: Repeating corrugation dimensions (in inches) 37
Figure 33: Cross-section dimensions of the support framing members (in inches) 38
Figure 34: Idealized bi-linear stress strain curve for FEA simulations 38
Figure 35: MPC constraints for loaded/ fixed supports and fasteners 39
Figure 36: Fastener behavior (orange) utilized in FEA models to improve stiffness 39
Figure 37: Contact definition locations in the model for panel ends and support members and panels edges and loaded/fixed beams 40
Figure 38: Discretization of steel deck panel and support framing members 40
Figure 39: Applied Boundary conditions for the non-linear analysis 41
Figure 40:Comparison of experimental and FEA force displacement response 42
Figure 41: Comparison of experimental and FEA force displacement response with bi-linear fastener data and increased ductility material models 43
Figure 42: Comparison of FEA and experimental deformed states for the 36/4 skip pattern specimen 44
Figure 43: Comparison of FEA and experimental deformed states for the 36/5 specimen 45
Figure 44: Comparison of FEA and experimental deformed states for the 36/7 fully attached specimen 46
Figure 45: FEA force-shear displacement results summary 47
Figure 46: Location of out-of-plane displacement measurements for determining onset of buckling 48
Figure 47: Comparison of out-of-plane displacement versus applied force for 22-gauge 36/7, 36/5, and 36/4 simulations 48
Figure 48: Summary of FEA out-of-plane displacement (Δ_z) of flutes at midspan versus applied force 49
Figure 49: Overall test-rig schematic (Castaneda 2022) 56

Figure 50: Fixed beam details (Castaneda 2022) 57
Figure 51: Free/Load beam details (Castaneda 2022) 58
Figure 52: Transverse beam details (Castaneda 2022) 59
Figure 53: Sensor layout and loading protocol 61
Figure 54: Actuator force displacement summary (Full page) 63
Figure 55: Shear force-displacement summary (Full page) 64
Figure 56: 36-7-R1: Actuator and Sensor force-displacement results 65
Figure 57: 36-7-R1: Actuator and Sensor displacement time data 66
Figure 58: 36-7-R2: Actuator and Sensor force-displacement results 67
Figure 59: 36-7-R2: Actuator and Sensor displacement time data 68
Figure 60: 36-7-R3: Actuator and Sensor force-displacement results 69
Figure 61: 36-7-R3: Actuator and Sensor displacement time data 70
Figure 62: 36-5-R1: Actuator and Sensor force-displacement results 71
Figure 63: 36-5-R1: Actuator and Sensor displacement time data 72
Figure 64: 36-5-R2: Actuator and Sensor force-displacement results 73
Figure 65: 36-5-R2: Actuator and Sensor displacement time data 74
Figure 66: 36-5-R3: Actuator and Sensor force-displacement results 75
Figure 67: 36-5-R3: Actuator and Sensor displacement time data 76
Figure 68: 36-4-R1: Actuator and Sensor force-displacement results 77
Figure 69: 36-4-R1: Actuator and Sensor displacement time data 78
Figure 70: 36-4-R2: Actuator and Sensor force-displacement results 79
Figure 71: 36-4-R2: Actuator and Sensor displacement time data 80
Figure 72: 36-4-R3: Actuator and Sensor force-displacement results 81
Figure 73: 36-4-R3: Actuator and Sensor displacement time data 82
Figure 74: 36-5-R3: Determination of P_{nb} 84
Figure 75: Force vs displacement results for parametric evaluation 86
Figure 76: Force vs Mid-span out-of-plane displacement results for parametric evaluation 87

List of tables

Table 1: Experimental configurations (Adapted from Easley 1975) 10
Table 2: Summary of tested assemblies and calculated limit states..... 17
Table 3: Summary of Results (Ultimate load and stiffness) 24
Table 4: Summary of results [initiation of buckling and comparison with AISI S310 Section D2 (AISI 2020)]..... 25
Table 5: summary of results [Stiffness comparison with AISI S310 Section D5 (AISI 2020)] ... 25
Table 6: Numerical modelling matrix for FEA Expansion 36
Table 7: Comparison of FEA and experimental peak strength and displacement 42
Table 8: Comparison of FEA and experimental stiffness and reduction in stiffness due to changing fastener pattern..... 42
Table 9: Summary of FEA predicted ultimate cpaacities and stiffness (non-linear analysis)..... 47
Table 10: Comparison of non-linear analysis predicted capacities and AISI S310 -20 Section D2 capacities (AISI 2020) 50
Table 11: Comparison of non-linear analysis predicted stiffness and AISI S310 – 20 stiffness (AISI 2020) 51

1. Introduction

Diaphragms (Figure 1) serve as a critical component of a building's lateral force resisting system (LFRS), transferring lateral loads from the façade of the structure to the designated vertical lateral force resisting system. Design guidance for profiled steel diaphragm panels can be found in AISI S310 – 20 (AISI 2020) and SDI DDM04 (Luttrell 2015) and are controlled by connection limit states or buckling limit states. Deck connectivity with the underlying frame can either be fully attached (For example 36/7), i.e. connected through the bottom of each flute, or partially attached (for example 36/5 or 36/4) where not all the flutes are attached to the frame (Figure 1). While adequate guidance is provided to account for the impact of support attachment patterns (Figure 1) on the connection limit states, the out of plane panel buckling limit state does not consider this impact. Existing research is also limited to the fully attached (36/7) attachment pattern and no comprehensive dataset exists where tests were specifically designed and performed to study the impact reducing support fasteners (36/5 and 36/4) can have on buckling capacity and behavior.

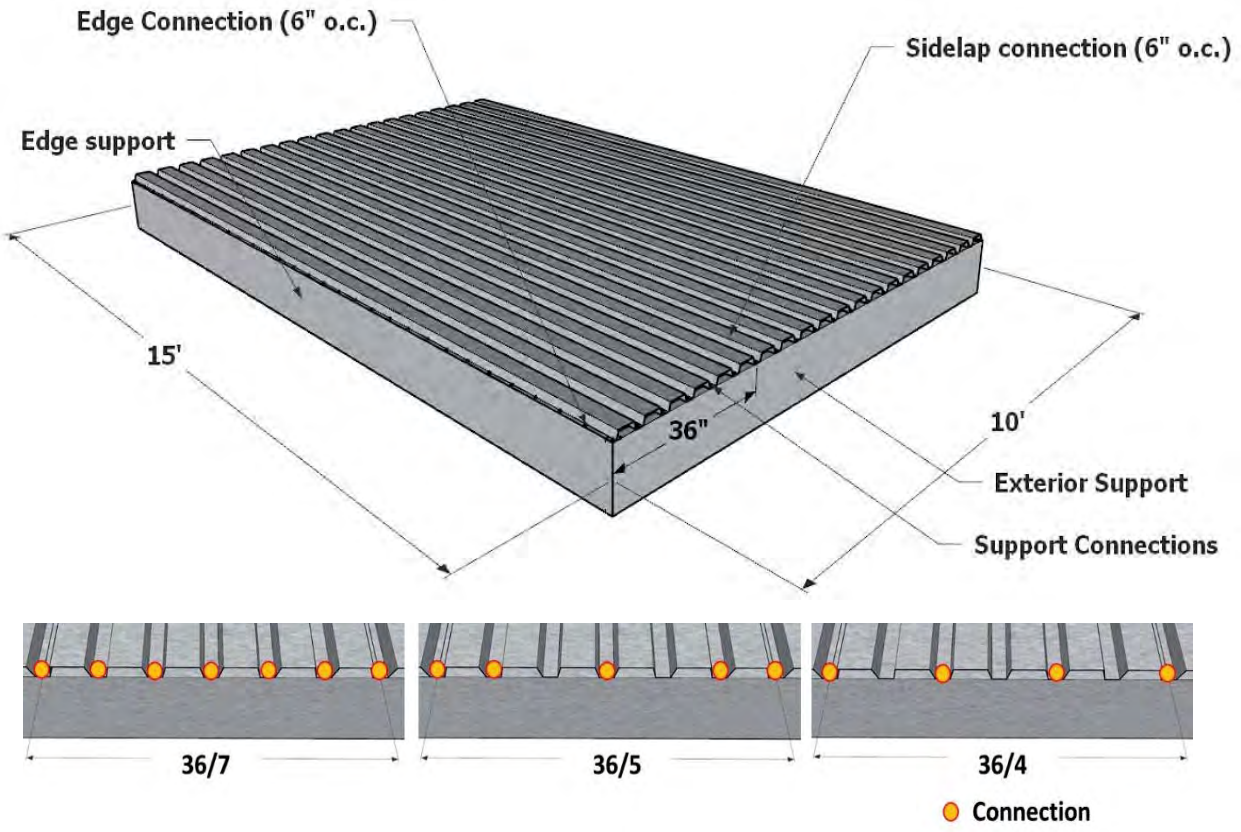

Figure 1: Diaphragm components and typical attachment patterns

To further understand the relationship between support attachment pattern and the out-of-plane buckling limit state, nine monotonic tests were conducted at the University of Massachusetts Amherst Robert B. Brack Structural testing facility. These tests were performed on the cantilever test frame and comprised of three unique configurations with three repetitions each. The specimens

were all constructed with 22 gauge (0.76 mm) Type B deck (Figure 2) and had identical span lengths (L_v), thickness (t), sidelap, and edge connections and only differed in the number of fasteners at the supports to simulate industry standard attachment patterns (Figure 1). This report summarizes the utilized test procedure, key results, and conclusions of this study.

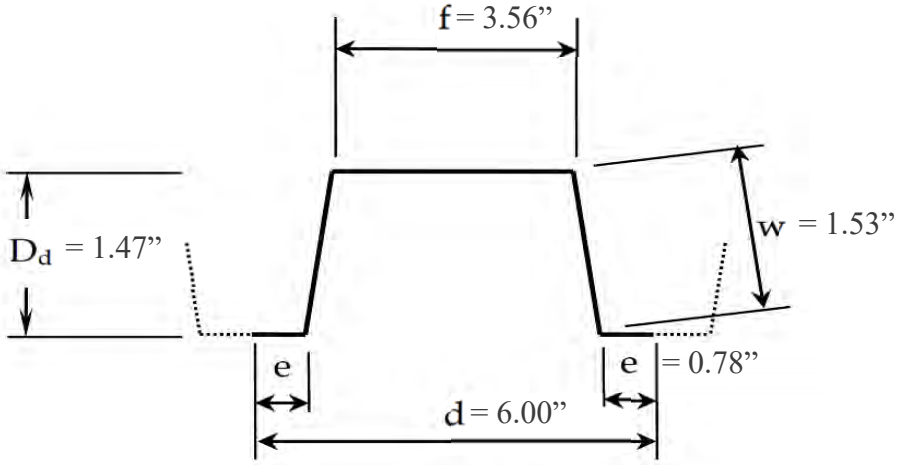

Figure 2: Typical corrugation dimensions for Type B Deck (Luttrell 2015)

2. Relevant works

Although there exists a wealth of literature which focuses on the strength and stiffness of diaphragm systems and applicable limit states, the works of Easley (Easley 1975), Wright and Hossain (Wright and Hossain 1997), and Nunna (Nunna 2011) are discussed below due to the unique insights they offer on the panel buckling limit state. Through the works of Easley (Easley 1975) and Nunna (Nunna 2011), the origin of the panel buckling equation is traced to its current calibrated and modified form. Wright and Hossain's (Wright and Hossain 1997) investigation on the impact of attachment method on end restraint coefficient β, has also been included to examine the differences end attachment methodology can have on strength.

2.1 Easley (1975)

The existing buckling limit state equation (Equation 1) is a modified and calibrated form of the elastic buckling equation developed by Easley and McFarland (Easley 1975). They developed elastic buckling equations (Equation 2) to predict critical shear load per unit length of a corrugated metal panel by utilizing the Ritz energy method. Panels were treated as plates with different flexural rigidities in the two perpendicular directions and the ends were assumed to be simply supported through the mid-plane of every flute. These equations were validated via a suite of eight experimental tests which varied in aspect ratio (Table 1 and Figure 3), corrugation pitch, and stiffness in the orthogonal directions. Tabs attached to the mid-plane of corrugations were utilized to apply load through the neutral axis of the panel. These tabs were clamped into the test frame in an attempt to create a simply supported condition.

$$S_{no} = \frac{7890}{\alpha {L_v}^2}\left(\frac{{I_{xg}}^3 t^3 d}{s}\right)^{(0.25)} \quad (1)$$

$$S_{no} = 36\beta \frac{{D_x}^{1/4} D y^{3/4}}{b^2} \quad (2)$$

Equation 2 predicted buckling capacities within 1.06 to 1.25 times the experimentally measured capacities. Easley discovered that tabs had an end restraining effect which caused deviation from the equation as the supports no longer behaved as purely simply supported connections. The restraining effect of the tabs were accounted for by the end restraint coefficient β which theoretically varied between 1.0 and 1.9 (Easley 1975, Hlavacek 1968). They concluded that the elastic buckling equation was accurate for simply supported panels (β = 1.0), but true variation of β with end restraint is unknown and depended upon the attachment conditions.

Table 1: Experimental configurations (Adapted from Easley 1975)

Specimen ID	Dimensions (in)			N_{cr} (lb/in)		β	βN_{cr} (lb/in)
	Length	Width	q	measured	tested		
2-1	30.00	30.00	3.48	27-28	23.60	1.12	26.4
4-1,2	26.00	34.00	5.55	17-18	13.30	1.25	16.6
5-1,2	26.00	34.00	2.37	23-30	23.90	1.07	25.6
7-1,2	34.00	26.00	4.04	31-33	28.40	1.13	32.1

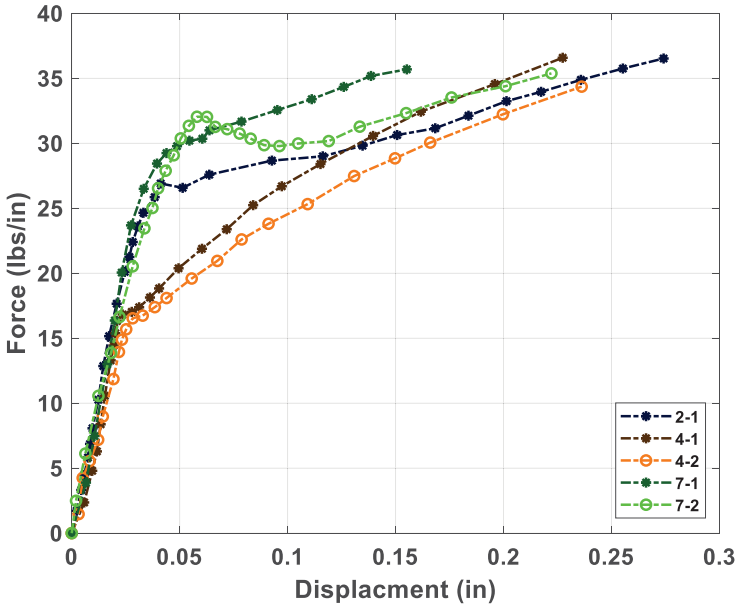

Figure 3: Summary of results of Easley test program (Adapted from Easley 1975)

2.2 Wright and Hossain (1997)

While developing analytical models to predict strength and stiffness of profiled sheets, Wright and Hossain (Wright and Hossain 1975) looked into the impact boundary attachment has on the buckling capacity of these sheets. Three distinct boundary conditions (Figure 4) were analyzed using finite element analysis (FEA) and compared to small scale tests: welded through both top flat and bottom flute (Type 1), welded through bottom flute (Type 2), discretely welded with spot

welds in bottom flute (Type 3). They found that Easley's buckling equations can accurately predict the shear buckling capacity but needed specific values of β to account for the effect of different boundary conditions i.e., end restraints. The reported β values varied from 1.72, 1.42, and 1.00 for Type 1, Type 2, and Type 3 boundary conditions respectively. These β values were back calculated from the FEA and experimental results. Further, Wright and Hossain also recommended a 50% reduction in buckling capacity if the sheets were only attached in alternate flutes. This 50% reduction also agrees with industry practice and is a significant deviation from what is recommended in the code.

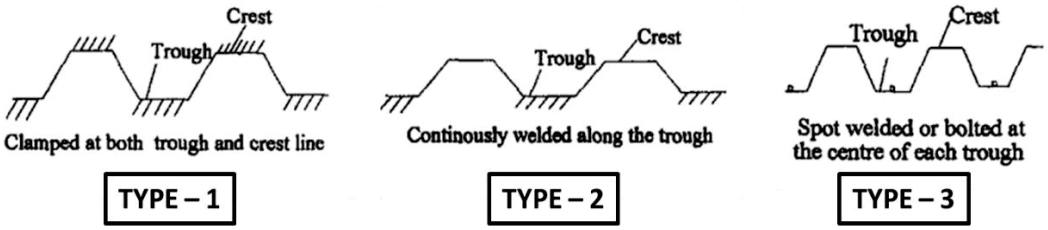

Figure 4: Evaluated boundary conditions (adapted from Wright and Hossain 1997)

2.3 Nunna (2011)

Nunna (Nunna 2011) evaluated the performance of panel buckling equations from TSM (Army, Navy, and Air Force 1982), SDI DDM03 (Luttrell 2004), Easley and McFarland (Easley 1975) and the proposed AISI S310 – 16 (AISI 2016a) equation (Equation 1). The equations were used to predict the buckling capacities for a historical dataset comprising of twenty-eight full-scale experiments where the failure mode was deck out-of-plane buckling without localized failure of fasteners. The specimens varied in corrugation depth (1.5 in specimen (26 nos.), 1-2 in specimen (1 no.), and 1- 5/8 in specimen (1 no.)), corrugation pitch – "d" (6 in (152.4 mm), 9 in (228.6 mm), and 12 in (304.8 mm)), gauge – "t" (29, 22, 20, 18 and 16 gauge), number of spans, and span length – "L". Twenty-seven of the twenty-eight specimens were fully attached to the test frame with connections through each flute. The strength to predicted ratios for TSM, Easley and McFarland, and proposed AISI S310 equations can be seen in Figure 5 below.

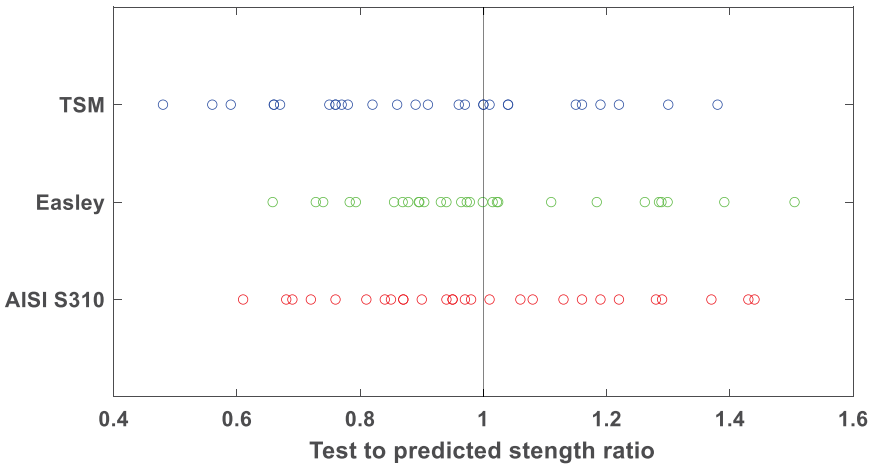

Figure 5: Comparison of existing equations

The comparison of the AISI S310 panel buckling equation with historical data can be seen in Figure 6. This equation had an average strength-to-predicted ratio and correlation coefficient of 1.002 and 0.910 respectively and could be utilized for single and multi-span applications (Nunna 2011). Nunna recommended that either the TSM, modified Easley, or proposed AISI S310 equation be used for estimating the out-of-plane buckling capacity of the deck. However, there was high variability in strength to predicted ratios (0.61 – 1.44) for the S310 out-of-plane buckling equation and all specimens had the same fully attached 36/7 pattern.

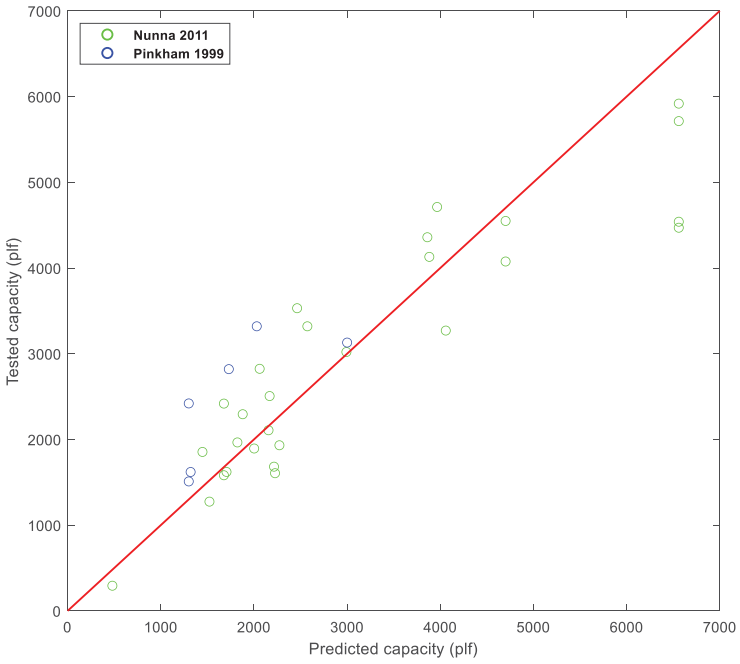

Figure 6: Comparison of current equation with historical test data

3 Design limit states and resultant design space

The nominal in plane shear strength (S_n) of a corrugated metal deck diaphragm is either governed by the limit state of connection failure (S_{nf}) or the limit state of shear buckling (S_{nb}). Current design standards and manuals such as AISI S310-20 (AISI 2020), SDI DDM04 (Luttrell 2015), and SDI-SDCFSFDM (Sputo 2017) utilize the same equations for estimating these limit states. Both limit states along with some example design configurations have been discussed in the following subsections.

3.1 Connection limit states

The available nominal shear strength governed by connection limit states (S_{nf}) is controlled by connection detailing and local failure (bearing/tilting, pull out, shear failure of fastener) of either the edge, interior, or corner connections (Fig 1). The following subsections discuss these limit states and their critical parameters.

3.1.1 Individual support and sidelap fastener strength

The available shear strength of the support/edge connections (P_{nf}) and side lap (P_{nfs}) connections is a critical input for the connection limit states calculations. Strength of typical screw fastened connections can be estimated from Chapter J.4.3.1 in AISI S100 (AISI 2016b), using Equations J4.3.1-1 through J4.3.1-5. The available shear strength of the Punchlok-II connection (VSC2) can be estimated using Equation 3 (IAPMO ER-0652 2018) provided by the deck manufacturer.

$$P_{nfs} = 137.42t - 2.01 \tag{3}$$

3.1.2 Edge connection (S_{ne})

The available shear strength per unit length from edge connections (S_{ne}) can be estimated by considering the contribution of all fasteners along the edge of an end panel and supports, and then averaging it across the length of the panel (Equation 4). This includes fasteners through both the interior and exterior supports and fasteners connected directly to the edge member. Interior and exterior support fasteners are accounted for by the measure of fastener group distribution across a panel width (w_e) by α_1 and α_2 respectively. The remaining fasteners are directly accounted for by n_e.

$$S_{ne} = \frac{(2\alpha_1 + n_p\alpha_2)P_{nf} + n_eP_{nf}}{L} \tag{4}$$

3.1.3 Interior connection (S_{ni})

The available shear strength per unit length governed by the failure of interior connections (S_{ni}) accounts for connection detailing at interior or edge panels and can be calculated using Equation 5 below. The number of fasteners through each flute at the supports (A), the distribution of fasteners across the panel (accounted for with β, different from Easley's β), and individual connection strength (P_{nf}) are all critical parameters for this calculation. Here, a relaxation term (λ-1), is used to account for the reduced capacity of corner fasteners due to buckling at support connections along sidelaps at panel ends. β (Equation 6) is the factor which defines connection contribution and interaction with the diaphragm shear strength. This further depends on the analogous section modulus of exterior (α_e^2) and interior supports (α_p^2), the number of sidelap connections (n_s) and connection strength ratio (α_s).

$$S_{ni} = [2A(\lambda - 1) + \beta]\frac{P_{nf}}{L} \tag{5}$$

$$\beta = n_s\alpha_s + 2n_p(\alpha_p)^2 + 4(\alpha_e)^2 \tag{6}$$

3.1.4 Corner connection (S_{nc})

The available shear strength per unit length controlled by the failure of the corner fastener (S_{nc}) can be estimated using Equation 7 below. The resultant of forces existing along the perpendicular and parallel edge of the deck is taken into consideration through N, β, and L and related to individual connection strength to estimate the limit state. Here N is the number of support fasteners per panel width (w_e), β is as described in 3.1.3, and L s the panel length.

$$S_{nc} = \left(\frac{N^2\beta^2}{N^2L^2+\beta}\right)^{0.5} P_{nf} \quad (7)$$

3.1.5 Connections along perpendicular edge (S_{np})

The available shear strength per unit length controlled by the failure of the connections along the perpendicular edge (S_{np}) can be estimated using Equation 8 below. Here n_d is the number of support fasteners per flute bottom and w_t is the greatest tributary width to any support connection perpendicular to the span and located at the exterior support.

$$S_{np} = n_d P_{nf} \frac{1}{w_t} \quad (8)$$

3.1.6 Sample connection limit states

The impact of changing attachment pattern on the connection limit states for a 22 gauge (0.76 mm) Type B deck (Figure 2) of variable length can be seen in Figure 7 below. Here, two different types of support connections, namely #14 (6 mm) fasteners [P_{nv} = 0.86 kips (3.83 kN)] and 0.85 in (21.6 mm) spot welds [P_{nv} = 2.56 kips (11.4 kN)], were considered for the calculations. These connections were assumed to either have the 36/7, 36/5, or 36/4 attachment patterns. Edge and sidelap spacing was held constant at 6 inches (152.4 mm) on center and were made with #12 (5.3 mm) fasteners [P_{nv} = .0.74 kips (3.30 kN)]. The governing predicted failure mode for all of these configurations (S_{nf}) was corner fastener failure (S_{nc}).

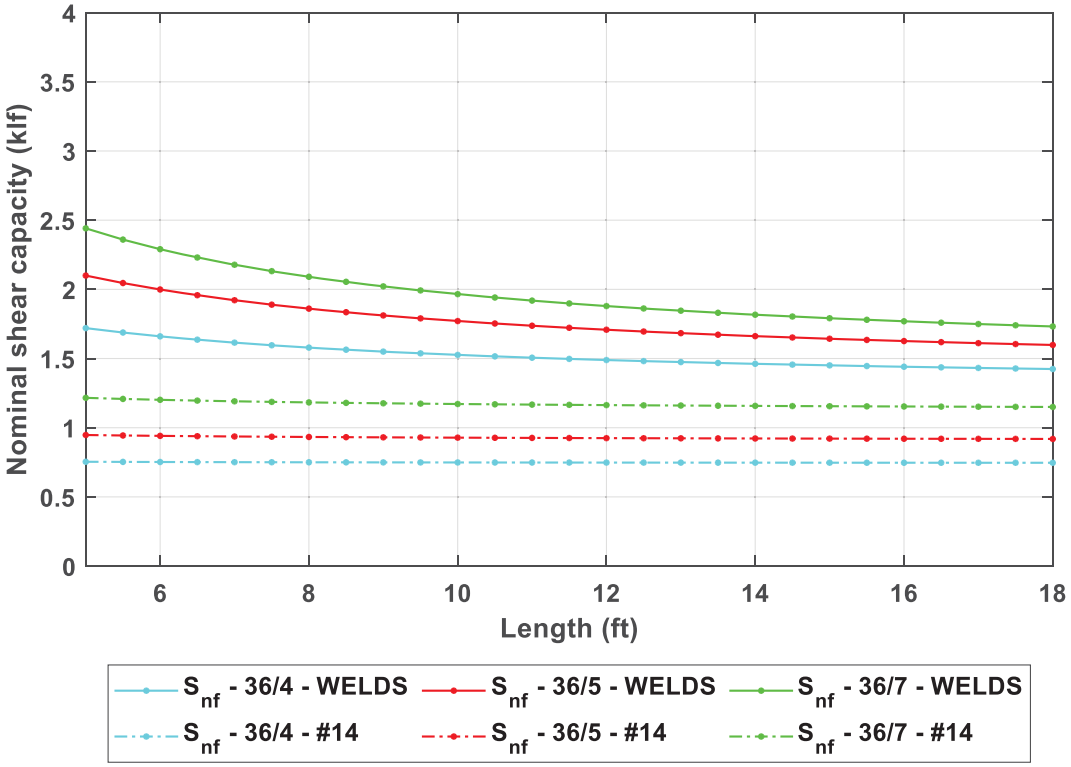

Figure 7: Connection limit states for 22 gauge Type B Deck

3.2 Panel buckling limit states (S_{nb})

The available nominal shear strength governed by panel buckling limit states (S_{nb}) is the minimum of the out-of-plane buckling capacity of the panel (S_{no}) and the local buckling capacity of the corrugation web over the supports (S_{nl}). The following subsections discuss these limit states and their critical parameters.

3.2.1 Global (Out-of-plane) buckling (S_{no})

The nominal shear strength per unit length of a diaphragm system controlled by out-of-plane buckling of the panel can be estimated using Equation 1. Here, the panel is assumed to be simply supported and capacity depends upon span length (L_v), moment of inertia per unit width (I_{xg}), thickness (t), corrugation pitch (d), and the developed flute width (s). The developed flute width is the flat width of sheet steel required to form an individual corrugation. The variation in S_{nb} due to increasing span length for a 22 gauge (0.76 mm) Type-B deck can be seen in Figure 8.

3.2.2 Local buckling (Web crippling) (S_{nl})

Local buckling in steel panels can be observed over the exterior supports and occurs after significant end warping of the panel ends. Both slenderness of the web and bearing length (N_{ext}) are important parameters that influence this diaphragm limit state. The failure mode is similar to web crippling (AISI 2020) and can be estimated using Equations 9 and 10 below.

$$S_{nl} = P_{nw}\left(\frac{d-e}{D_d}\right)\left(\frac{1}{d}\right) \tag{9}$$

$$P_{nw} = 4.36t^2F_y sin\theta\left(1 - 0.04\sqrt{\frac{R}{t}}\right)\left(1 + 0.25\sqrt{\frac{N_{ext}}{t}}\right)\left(1 + 0.025\sqrt{\frac{h}{q_s t}}\right) \tag{10}$$

Here, d, e, D_d, R, t, and h are corrugation pitch, half bottom flat width, panel depth, corner radii, thickness, and flat dimension of the web respectively. The same has been depicted for a typical trapezoidal corrugation in Figure 2.

3.3 Resultant design space

The unfactored capacity resultant design space for a 22 gauge (0.76 mm) Type B deck due to connection and stability limit states can be seen in Figure 8 below. For the local buckling calculations, N_{ext} was assumed to be the minimum recommended value of 0.75 in (19 mm) and corner radii were conservatively neglected. Sidelap and edge fastener spacings were set to 6 in (152.4 mm) on center. Here, for typical span lengths [<7.5 ft (2286 mm)] the governing limit state is either local buckling or connections (S_{nf}). S_{nb} does not govern design until 9.6 feet (2926 mm) and 14 feet (4267 mm) of span length for the selected welds and fasteners, respectively.

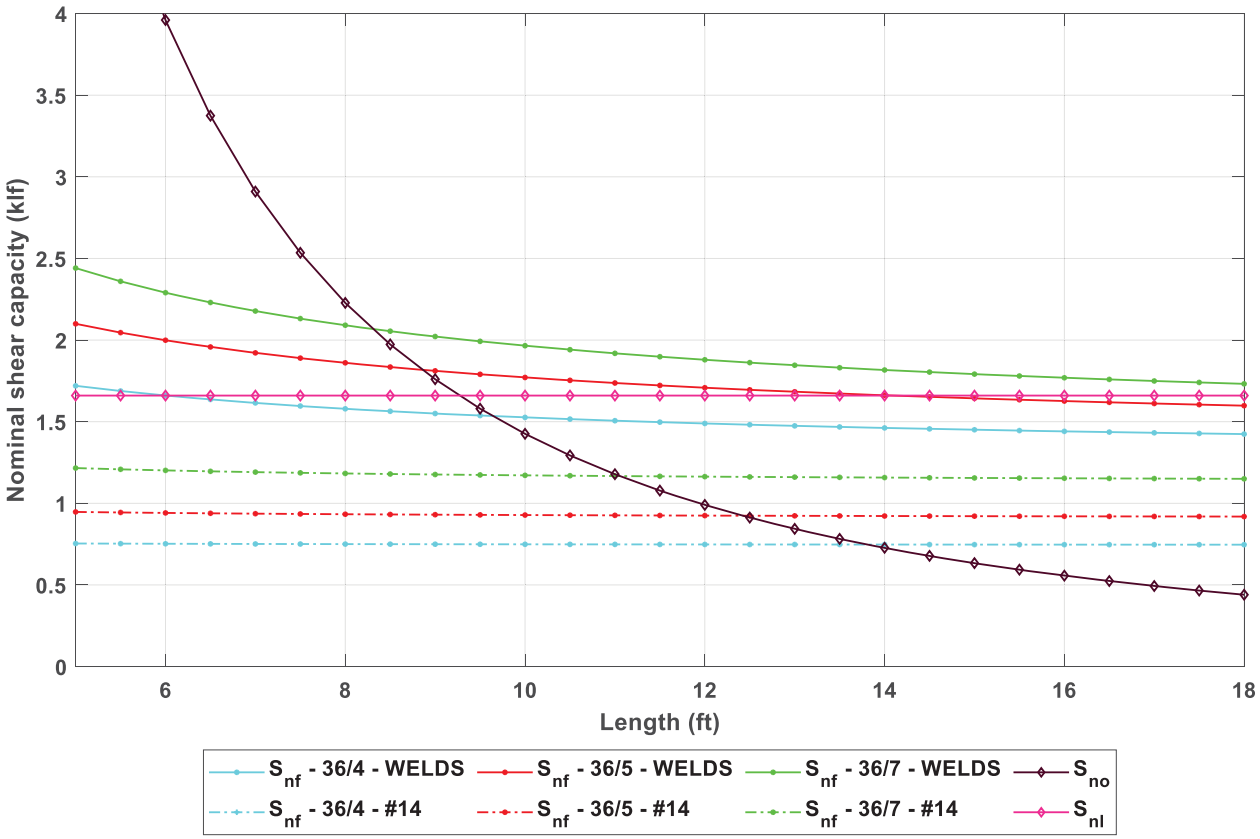

Figure 8: Resultant design space for panel buckling tests

4 Experimental test matrix and measured properties

4.1 Test matrix

The experimental test matrix (Table 2) was designed to ensure that panel buckling is the governing limit state across all the attachment patterns. This was ensured by providing adequate overstrength in the connection limit states [min (S_{nf}/S_{nb}) = 1.78)]. Support and edge fasteners connections were made with #14 (6 mm) screws which had a connection strength (P_{nf}) of 1.24 kips (5.52 kN) each when used with the 22-gauge deck (0.76 mm) and 54 mil (1.37 mm) CFS support angles. Sidelaps were made with the proprietary Punchlok – II tool which provided a P_{nf} of 2.10 kips (9.34 kN) for the 22-gauge (0.76 mm) deck. However, the sidelap capacity was conservatively restricted to support connection capacity [1.24 kips (5.52 kN)] for calculations as it was assumed that failure of the support connections would occur first along the sidelaps initiating failure in the test. Sidelaps and edge fasteners were installed 6 inches on center (152.4 mm). Nominal geometric dimensions and material properties [E = 29,500 ksi (203,400 MPa), Fy = 50 ksi (345 MPa), Fu = 65 ksi (448 MPa)] were used for all calculations.

Table 2: Summary of tested assemblies and calculated limit states

Specimen	Attachment Pattern [1,2,3]	L_v (ft)	S_{ni} (klf)	S_{nc} (klf)	S_{ne} (klf)	S_{np} (klf)	S_{nf} (klf)	S_{nb} (klf)	S_{nf}/S_{nb} (in)
36/7 - R1									
36/7 - R2	36/7	15.00	2.61	1.82	2.73	2.48	1.82	0.63	2.89
36/7 - R3									
36/5 - R1									
36/5 - R2	36/5	15.00	2.59	1.40	2.68	1.24	1.24	0.63	1.91
36/5 - R3									
36/4 - R1									
36/4 - R2	36/4	15.00	2.54	1.12	2.62	1.24	1.12	0.63	1.78
36/4 - R3									

Notes -

1. Edge and sidelap fastener spacing - 6 in (152.4 mm) on center
2. Exterior edge fastener type - #14 Hex head (P_{nf} = 1.24 kips)
3. Sidelap conections - VSC - II (P_{nf} = 2.10 kips, restricted to 1.24 kips)

4.2 Measured properties and dimensions

Thickness and bearing length (N_{ext}) measurements were taken from each of the specimen to compare with the nominal properties used in the test matrix design calculations. Thickness (t) of the panel has an impact on the nominal shear strength (P_{nv}) of the connection (AISI 2016b) and thereby impacts the connection limit states. Thirty-six thickness measurements were taken from various locations on the panel prior to construction and testing with a pair of digital Vernier Calipers. Figure 9(a) below shows the variation in t and the empirical cumulative distribution function for these measurements. The mean thickness including galvanization was 0.0305 in (77

mm) vs 0.0295 in (76 mm) as published in the deck manufacturer's specification and evaluation report (IAPMO ER-0652 2018). This was 2% higher than the nominal values used in the calculations and 97% of the measurements were above the nominal thickness value.

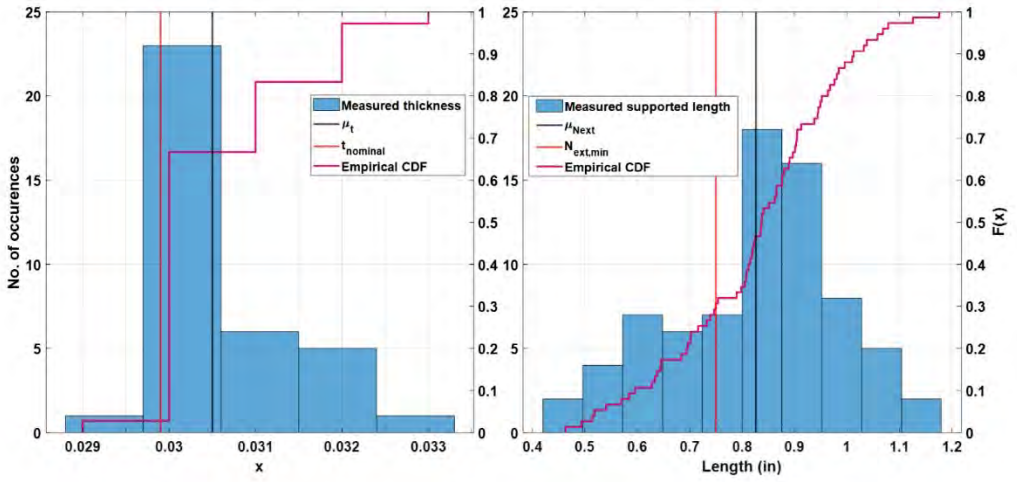

Figure 9: Measured thickness (left) and supported lengths (right)

Ten measurements of bearing length of deck on both the East and West supports were also recorded for each of the nine repetitions to compare against the minimum required value in AISI S310 of 0.75 in (19.0 mm). The recorded bearing lengths can be seen in figure 9(b). The mean supported length was 0.83 in (21.0 mm). Although the measurements varied from 0.46 in (11.7 mm) to 1.18 in (29.9 mm), at least 70% of the measurements were above the minimum required value.

5 Experimental Setup

The following subsections discuss the experimental test frame setup, sensor scheme, fabrication methodology, loading protocol, and data acquisition system utilized in the tests.

5.1 Test Frame

The cantilever test frame (Figure 10) was made up of hot-rolled steel plate girders and can be used to test specimens in 10 ft X 15 ft (3048 mm X 4572 mm) and 15 ft X 15 ft (4572 mm X 4572mm) configurations. The south side free beam is connected to the actuator and the north beam is fixed to the strong floor. Additionally, the free beam has a roller support near either end to prevent out-of-plane motion of the rig. These supports are connected to the free beam using high-capacity rollers [25 kips (111 kN)]. The bottom of the free beam also rests on rollers to allow translation of the beam due to action of the actuator. The free and fixed beams are connected by transverse beams on the east and west side with pins in all four corners to allow the test frame to pivot about the points of fixity. Detailed design, fabrication, and construction specifications of the rig have been discussed by Castaneda (Castaneda 2022) and select drawings can be found in Appendix C.

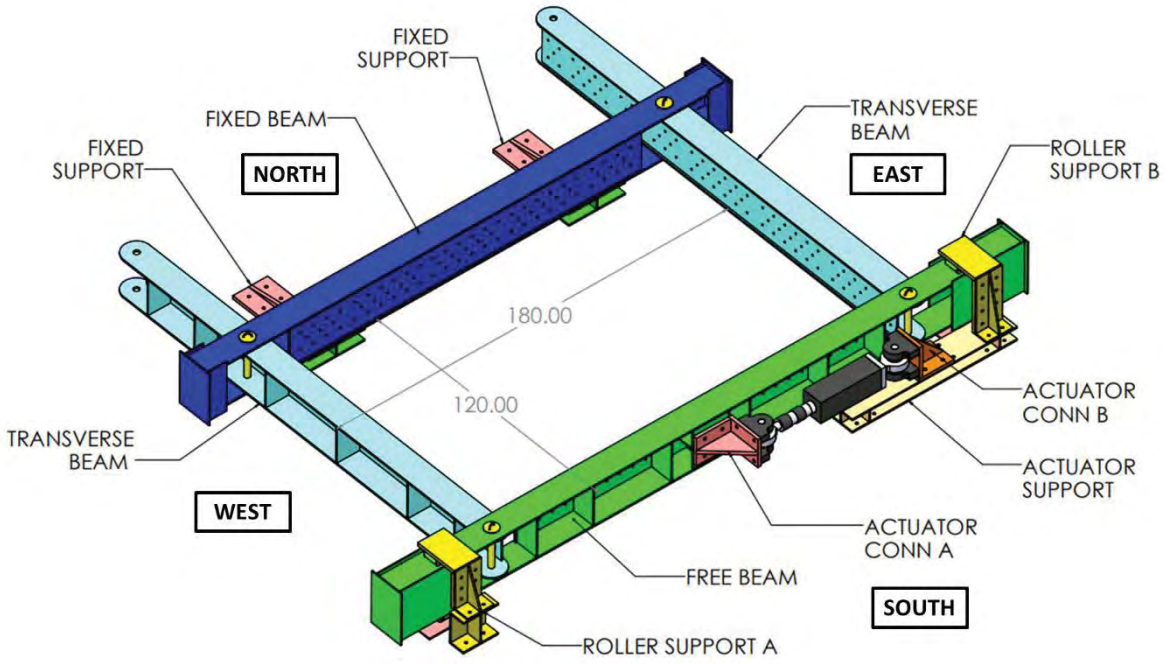

Figure 10: Cantilever test rig

5.2 Sensor locations

Linear variable differential transducers (LVDTs) were used to measure translations of the test rig and out of plane motion of the specimen. Three LVDTs each were located in the north-east and south-west corners of the test frame which measured the X, Y, and Z motion of the rig. Three sensor frames comprising of three LVDTs each were placed along the width of the specimen to

measure out-of-plane displacements at various locations during testing. Complete sensor layout and sensor coordinate system can be seen in Figure 11.

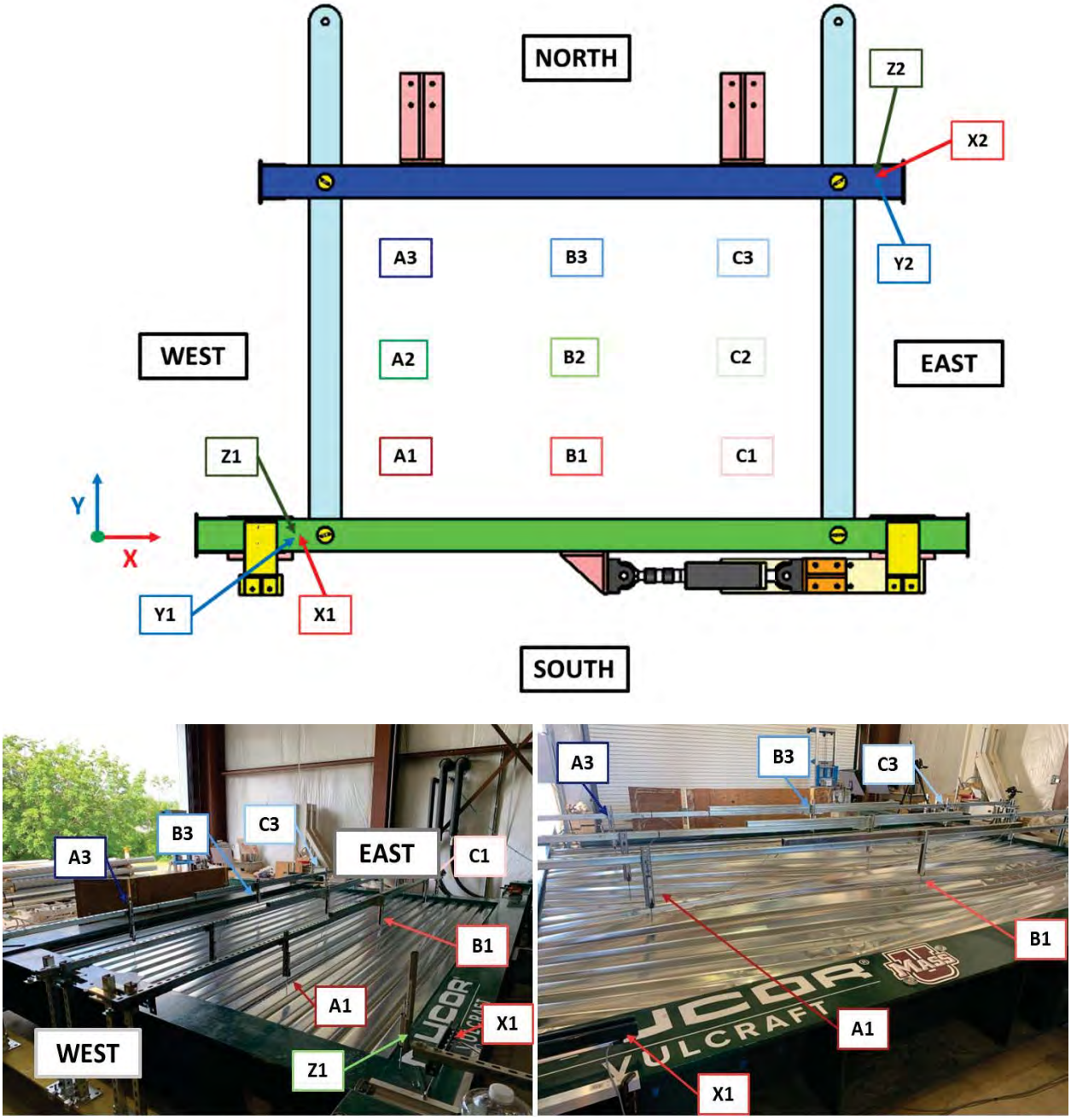

Figure 11: Sensor locations on specimen

5.3 Specimen fabrication

The 22 gauge (0.76 mm) steel deck was connected to the test rig using a supporting frame made from 600S200 – 54 cold-formed steel angles (Figure 12) which was created by splitting 1200S200

– 54 studs in half through the web. The frame members had holes drilled into them and were connected to the test rig with 0.75 in (19 mm) bolts placed approximately 2 ft (610 mm) on center along the fixed, free, and transverse beams. Hilti #14 (6 mm) self-drilling, self-tapping, hex head screws were used to make the support and edge connections (Figure 13). The individual pieces of deck were then connected at sidelaps using the proprietary Punchlok II tool (Figure 13).

Figure 12: Perimeter framing members

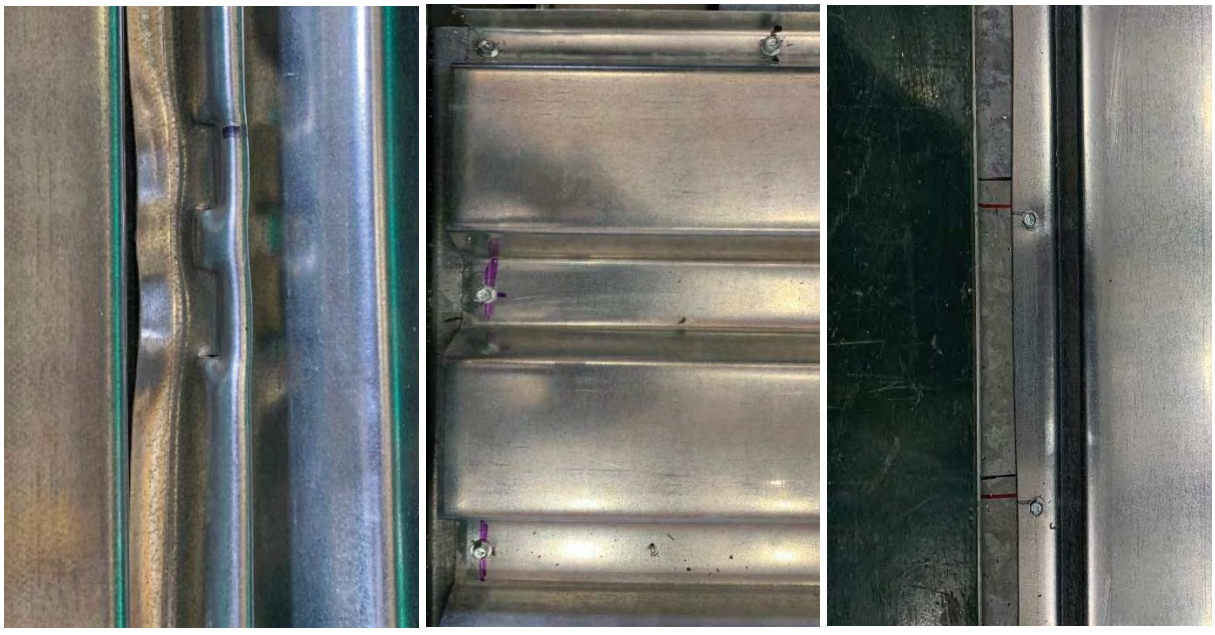

Figure 13: Typical sidelap (VSC-II), support (Hex-14), and edge connections (Hex-14)

To prevent any accidental damage to the specimen or unintentional loading during the sidelap construction, a 20 ft (6096 mm) long construction platform (Figure 14) was constructed using a

ladder and OSB sheathing. This platform was used as the working platform during crimping of the seams and supported all construction loads.

Figure 14: Construction platform for sidelap connections. The Punchlok – II tool was supported by the crane during specimen fabrication

5.4 Loading protocol and data acquisition

A monotonic load protocol (Figure 15) was utilized to load the specimen using the MTS 244.41 hydraulic actuator and FLEXTEST 60 controller. Peak displacement was set to 3 in (76.2 mm) and the specimen was loaded at a rate of 0.0033 in/sec (0.084 mm/sec) to achieve approximately 1 in (25.4 mm) of displacement every 300 seconds of testing. Data acquisition was done with National Instruments data acquisition system and LabView program at an acquisition rate of 10 Hz.

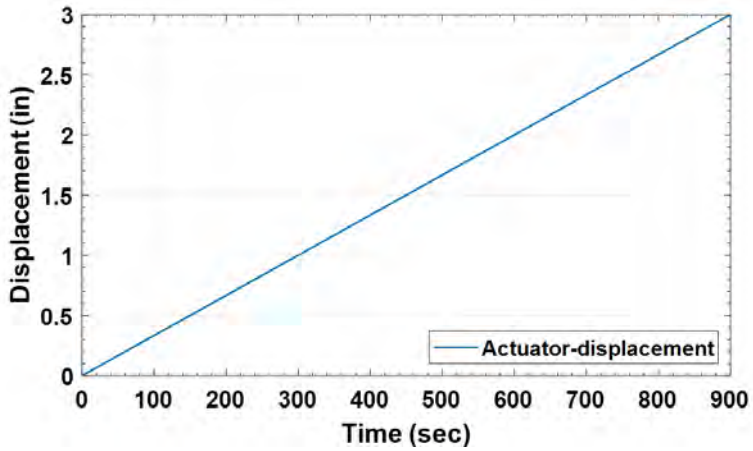

Figure 15: Typical monotonic loading protocol (Δ_{max} = 3in)

6 Results

The following sections and subsections present and discuss the results and post processing methods utilized in the experimental testing and interpretation of data.

6.1 Summary of experimental results

The data acquisition system provided unfiltered sensor data from the actuator and out-of-plane displacement sensors. Unprocessed actuator force-displacement results for the specimen have been depicted in Figure 16 below. Table 3 summarizes the ultimate capacity, displacement, and stiffness results for the tests. Conversion of unprocessed actuator force-displacement to shear force-displacement data was required to estimate the ultimate capacity (P_{max}), displacement at maximum load (Δ_s), and stiffness (G') of the specimen. The processing methods for the same are discussed in section 6.1.1 and 6.1.3. Table 4 summarizes the load and displacement levels at the initiation of out-of-plane buckling (P_{nb}). Out-of-plane sensor data was utilized to establish load level for initiation of buckling. The methodology for the same has been discussed in Section 6.1.2. Figure 17 shows the corrected force-shear displacement results, P_{max}, P_{nb}, and P_{40} for all the specimens. Individual sensor force-displacement results for all the repetitions have been summarized in Figure 18.

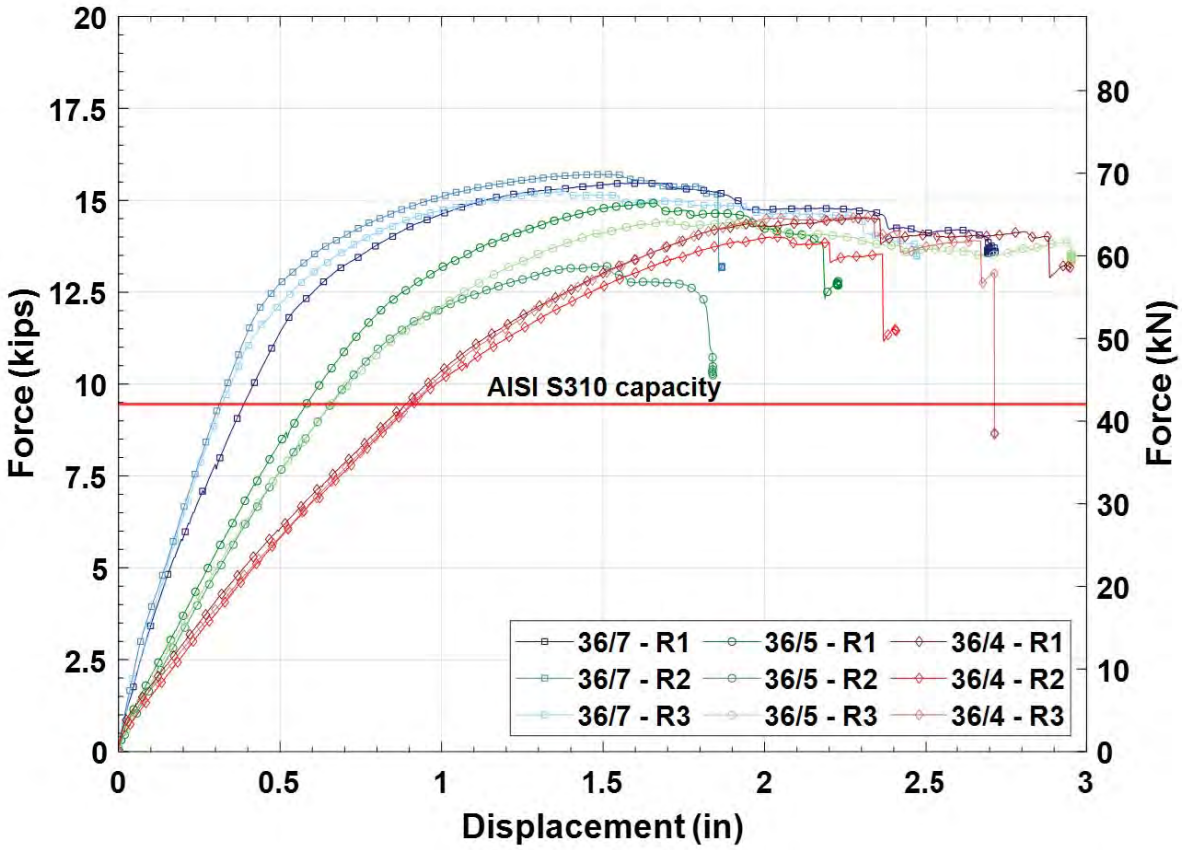

Figure 16: Unprocessed actuator force displacement results summary

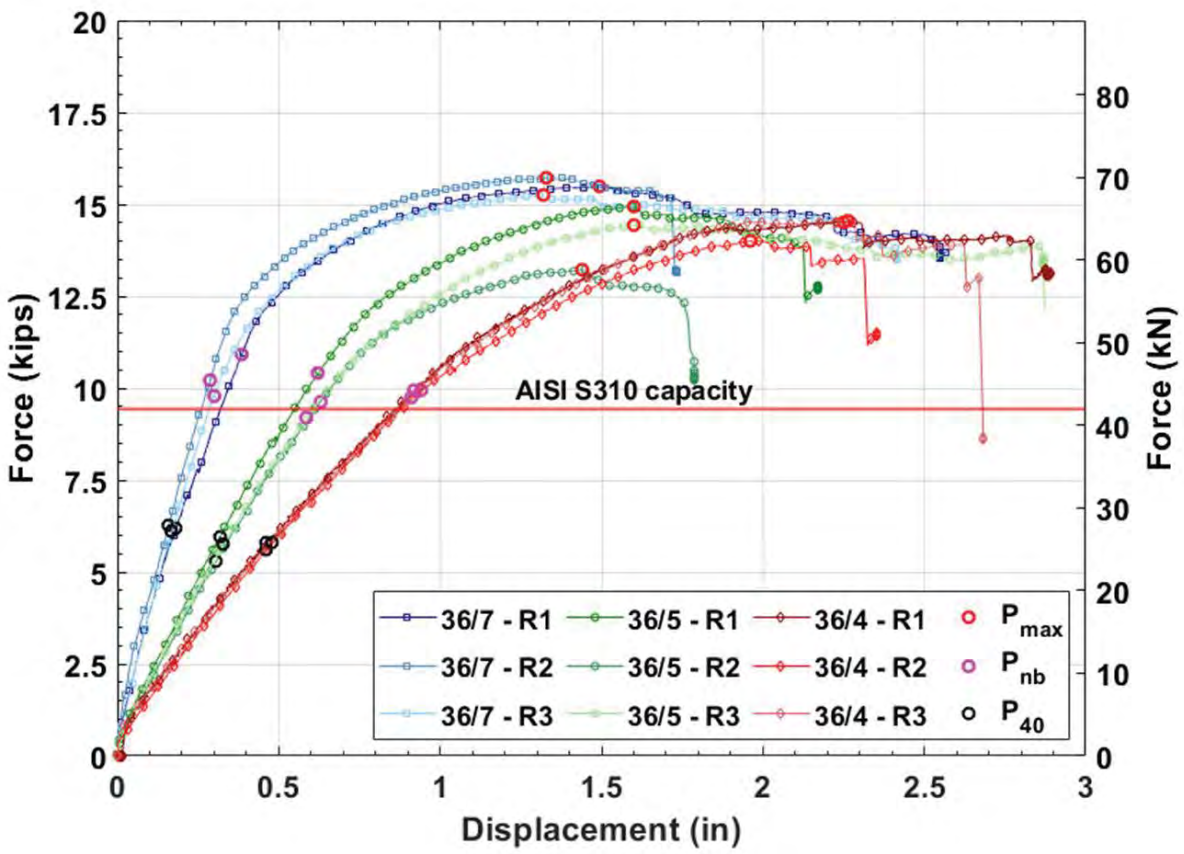

Figure 17: Processed force-shear displacement results summary

Table 3: Summary of Results (Ultimate load and stiffness)

Specimen	P_{max} (kips)	$P_{max,ave}$ (kips)	Δ_{Pmax} (in)	$\Delta_{Pmax,ave}$ (in)	G' (kips/in)	G'$_{ave}$ (kips/in)
36_7_R1	15.5		1.65		22.8	
36_7_R2	15.7	15.5	1.47	1.50	26.4	24.5
36_7_R3	15.3		1.38		24.2	
36_5_R1	14.9		1.66		12.5	
36_5_R2	13.2	14.2	1.50	1.62	11.5	11.9
36_7_R3	14.4		1.69		11.7	
36_4_R1	14.5		2.32		8.40	
36_4_R2	14.0	14.4	2.01	2.21	8.08	8.20
36_4_R3	14.6		2.31		8.12	

Table 4: Summary of results [initiation of buckling and comparison with AISI S310 Section D2 (AISI 2020)]

Specimen	P_{nb} (kips)	$P_{nb,ave}$ (kips)	Δ_{Pnb} (in)	$\Delta_{Pnb,ave}$ (in)	$P_{nb}/P_{nb,AISI}$	$(P_{nb}/P_{nb,AISI})_{ave}$
36_7_R1	10.9		0.38		1.15	
36_7_R2	10.2	10.3	0.29	0.32	1.08	1.09
36_7_R3	9.78		0.30		1.03	
36_5_R1	10.4		0.62		1.10	
36_5_R2	9.62	9.7	0.62	0.61	1.02	1.03
36_7_R3	9.19		0.58		0.97	
36_4_R1	9.94		0.92		1.05	
36_4_R2	9.93	9.9	0.94	0.92	1.05	1.05
36_4_R3	9.76		0.91		1.03	

Table 5: summary of results [Stiffness comparison with AISI S310 Section D5 (AISI 2020)]

Specimen	G' (kips/in)	G'_{ave} (kips/in)	G'_{AISI}[1] (kips/in)	G'_{ave}/G'_{AISI}
36_7_R1	22.8			
36_7_R2	26.4	24.5	72.9	0.34
36_7_R3	24.2			
36_5_R1	12.5			
36_5_R2	11.5	11.9	18.7	0.64
36_7_R3	11.7			
36_4_R1	8.40			
36_4_R2	8.08	8.20	13.61	0.60
36_4_R3	8.12			

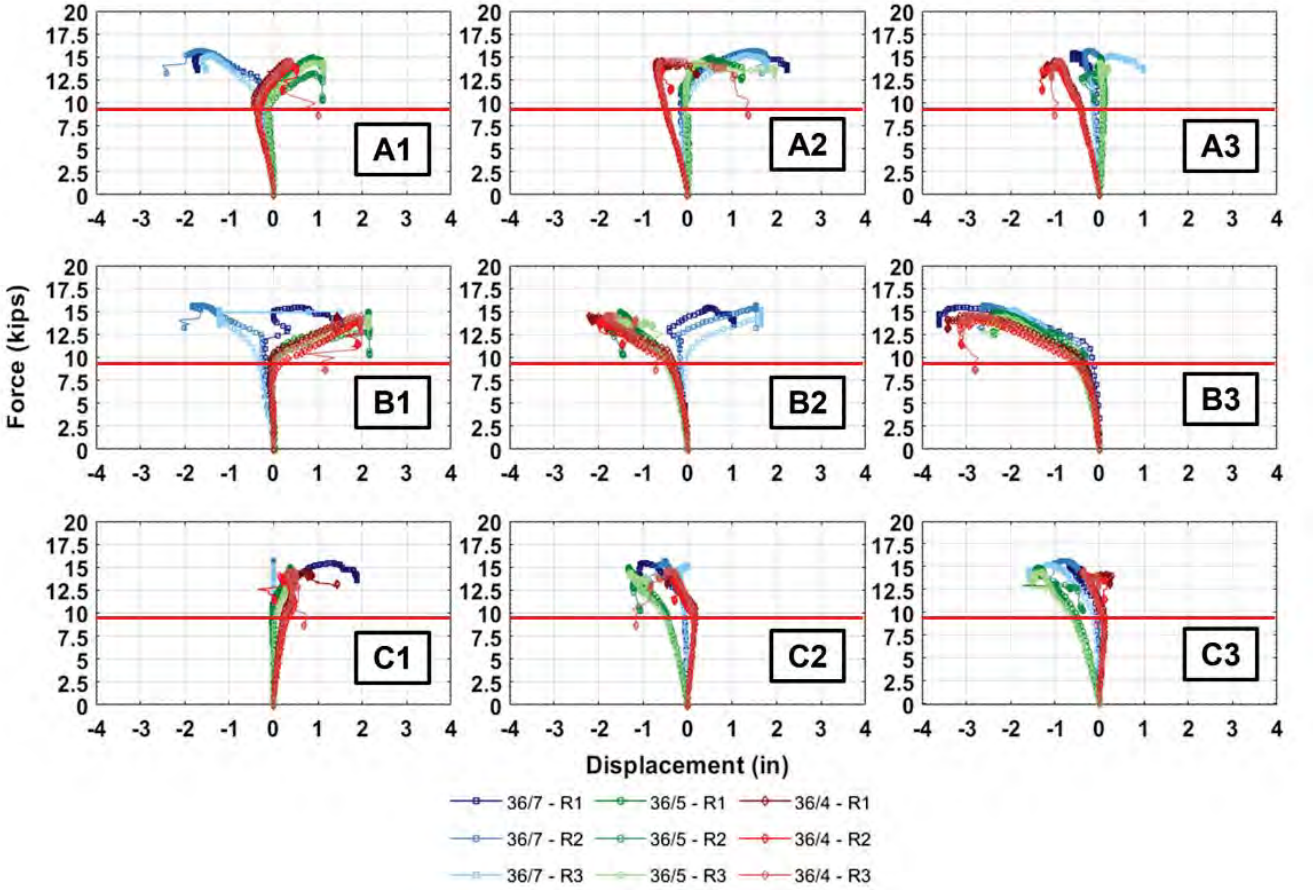

Figure 18: Summary of sensor force-out-of-plane displacement (Δ_z)

6.1.1 Estimation of peak load (P_{max}) and corrected displacement

To account for initial actuator load and lateral translation of the rig, the measured force and displacement results were corrected using initial force readings and adapted forms of the equations (Equation 10) presented in AISI S907 (AISI 2017) respectively. Figure 19 below shows the sensor locations that were used to measure in-plane translations of the rig. These displacements were subtracted from the measured displacements using Equation 11 to obtain the pure shear displacement (Δ_s) of the specimen.

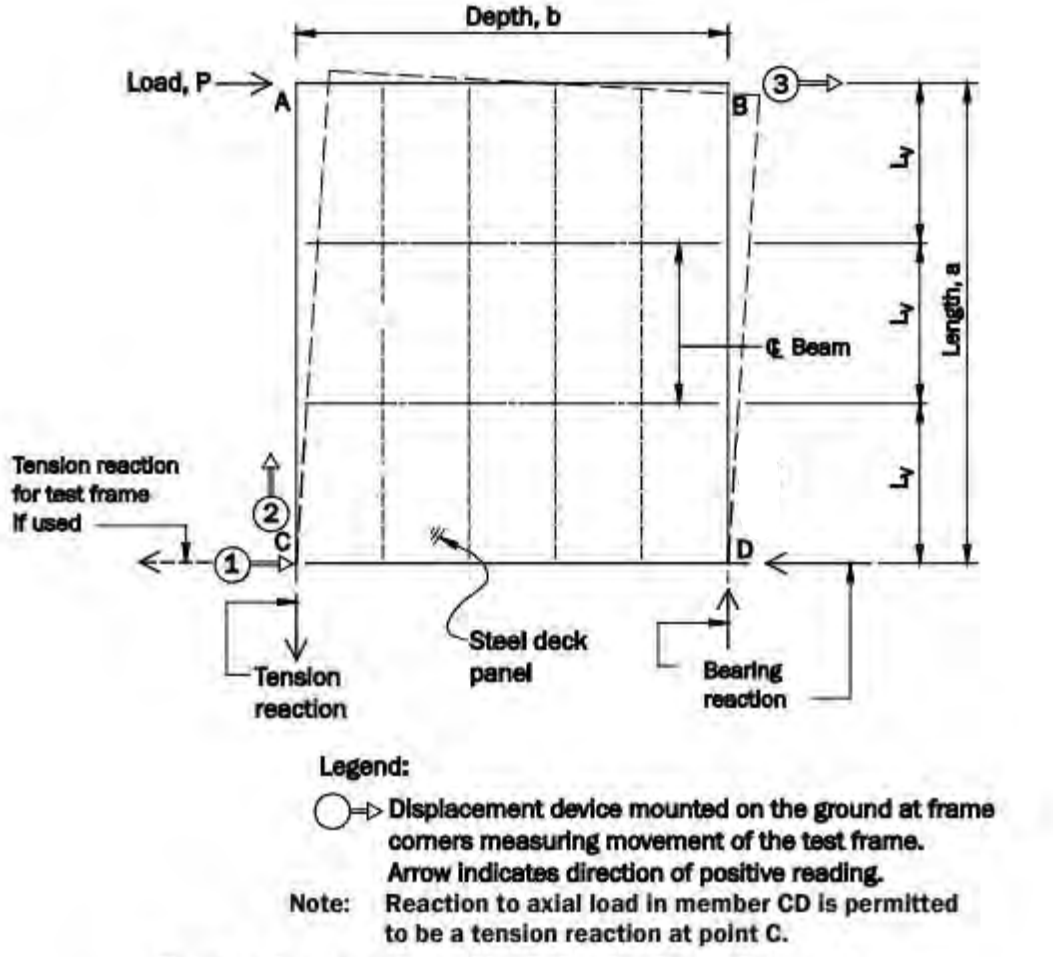

Figure 19: Estimation of corrected displacement [Adapted from AISI S907 (AISI 2017)]

$$\Delta_s = \Delta_3 - \Delta_1 \tag{11}$$

6.1.2 Estimation of load (P_{nb}) and displacement (Δ_{nb}) level corresponding with onset of out-of-plane buckling

Results from the out-of-plane sensors (Sensors A1 through C3, Figure 11) were used to establish onset of out-of-plane buckling in the specimen. Sensor displacement-time results were evaluated

to identify the time step at which rapid Z axis movement was recorded by the sensors. This time step was correlated with the actuator force-time results to determine force required (P_{nb}) to initiate out of plane buckling in the specimen. This force level was then correlated with the corrected force-shear displacement plots to determine displacement level (Δ_{nb}) at which first signs of out-of-plane motion were recorded. The force level (P_{nb}) was also verified by comparing results with sensor force-displacement results. This process has been visualized for the 36/5-R3 specimen in Figure 20 through 22.

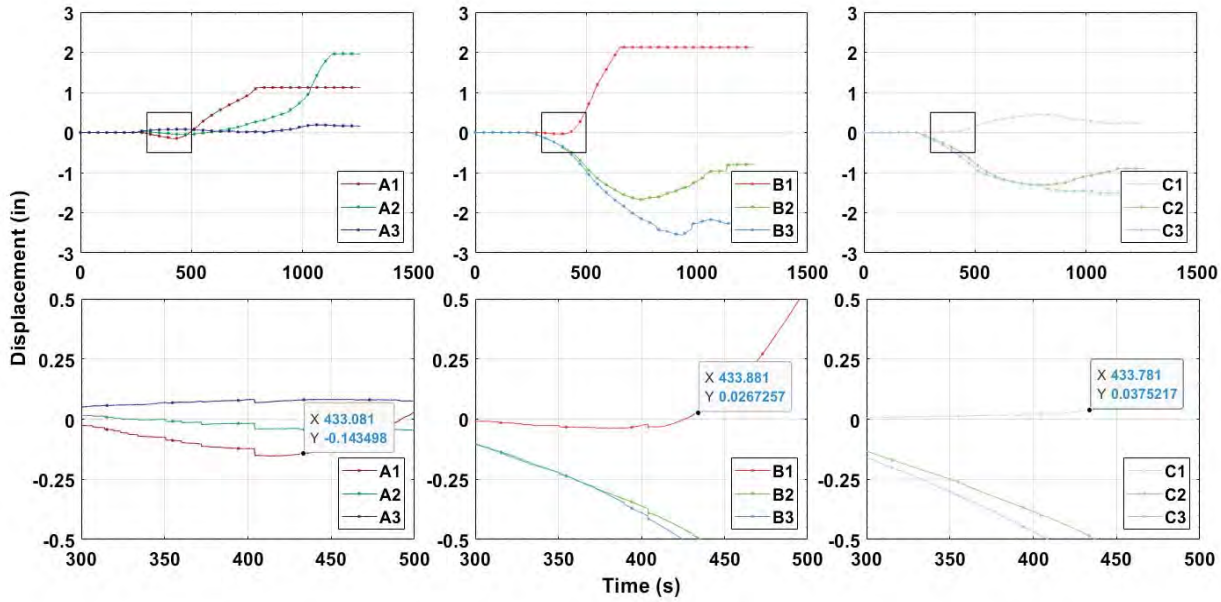

Figure 20: Determining time step corresponding with onset of out-of-plane buckling. Bottom three plots represent insets of corresponding top three plots.

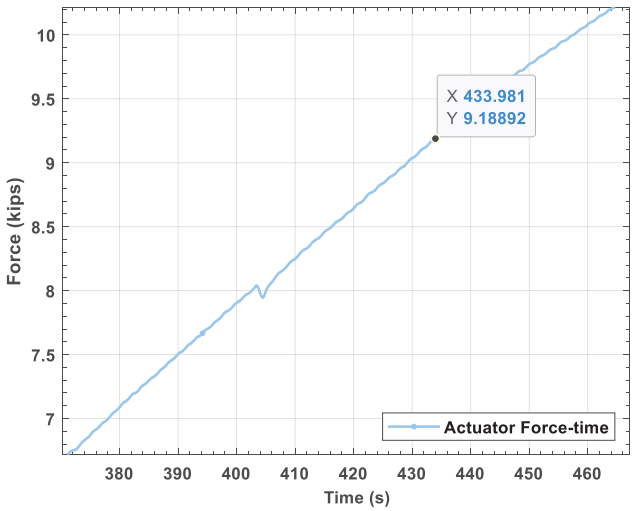

Figure 21: Determining force level (P_{nb}) corresponding with time step

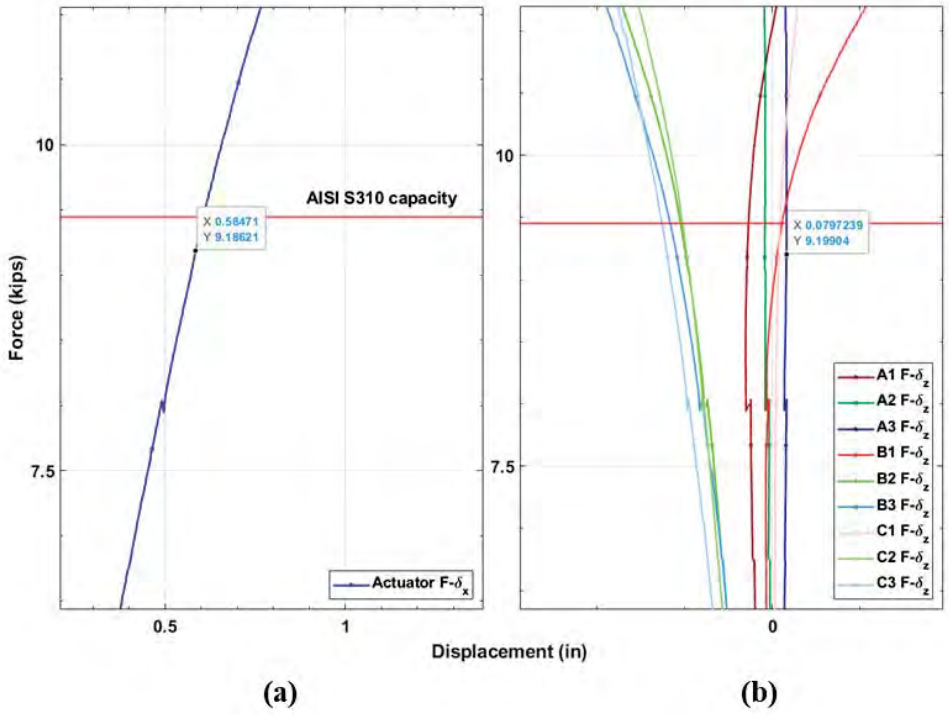

Figure 22: (a) Determining displacement level Δ_{nb} (b)verification of P_{nb}

6.1.3 Estimation of Stiffness (G')

Stiffness of the specimen were calculated from the corrected force-shear displacement results at the 40% peak load level (P_d and Δ_d) as depicted in Figure 23 below. This was based on recommendations from AISI S907 – Test Standard for determining the strength and stiffness of cold-formed steel diaphragms by the cantilever test method (AISI 2017).

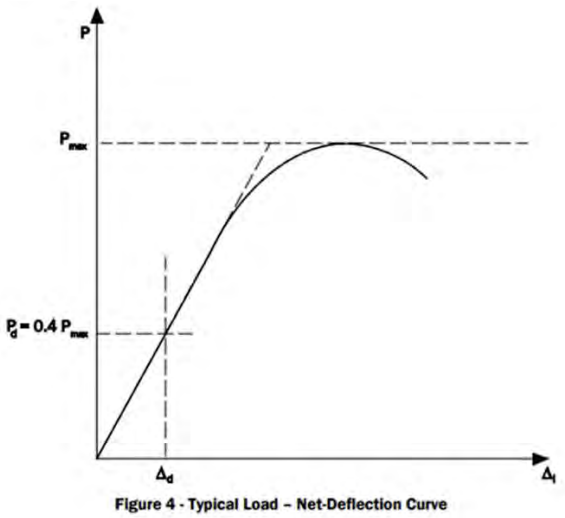

Figure 23: Estimation of diaphragm stiffness, G' (AISI 2017)

$$G' = \frac{P_d \times a}{\Delta_d \times b} \tag{12}$$

6.2 36-7 Fully attached specimen

The 36/7 fully attached specimen had an average peak capacity ($P_{max,ave}$) of 15.5 kips (66.7 kN) at an average displacement (Δ_{Pmax}) of 1.50 in (38.1 mm). Initiation of out-of-plane buckling, as indicated by the rapid movement of the out-of-plane sensors, occurred at an average load ($P_{nb,ave}$) of 10.3 kips (45.8 kN) (Table 4 and Figure 17) at 0.32 in (8.12 mm) of average displacement ($\Delta_{pnb,ave}$). Strength to predicted ratios for individual repetitions have been summarized in Table 4. The average strength to predicted capacity ratios for the maximum capacity ($P_{max}/P_{nb,AISI}$) and initiation of buckling ($P_{nb}/P_{nb,AISI}$) were 1.64 and 1.09 respectively. The average stiffness (G'_{ave}) for the 36/7 repetitions was calculated to be 24.5 kips/in (4.29 kN/mm) (Table 5).

These tests were terminated either due to large post-peak deflections, flattening of flutes, or post-peak connection failures. The 36/7 – R1 test was terminated due to excessive flattening of the corner flute (Figure 24.a) in Panel 01 at the West support. The 36/7 – R2 test was terminated due to a post-peak pull out failure of the support fastener in Panel 01 on the West support (Figure 24.b). The 36/7 – R3 test was terminated due to excessive post-peak deformations and flattening of the corner flute on the West support (Figure 24.c).

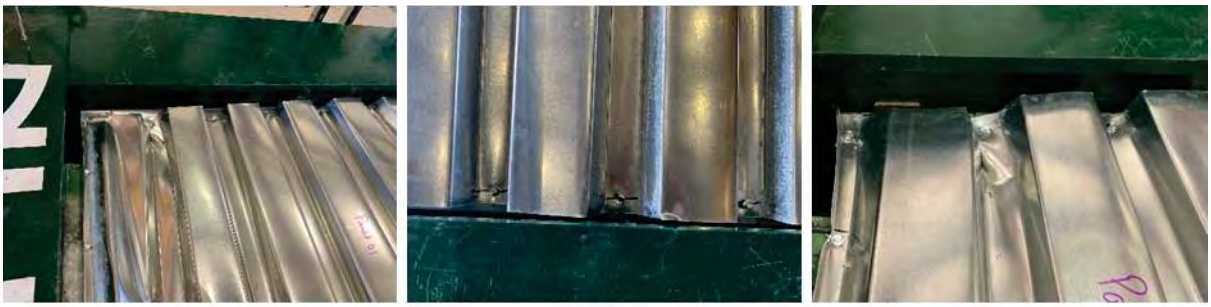

Figure 24: Observed post-peak failure modes in the 36/7 repititions:

(a) 36/7-R1 (b) 36/7-R2 (c) 36/7-R3

6.3 36-5 Intermediately attached specimen

The 36/5 intermediately attached specimen had an average peak capacity ($P_{max,ave}$) of 14.2 kips (63.2 kN) at an average displacement (Δ_{Pmax}) of 1.62 in (41.1 mm). Initiation of out-of-plane buckling, as indicated by the out-of-plane sensors, occurred at an average load ($P_{nb,ave}$) of 9.70 kips (43.1 kN) (Table 4 and Figure 17) at 0.61 in (15.5 mm) of average displacement ($\Delta_{pnb,ave}$). The average strength to code predicted capacity ratios for the maximum capacity ($P_{max}/P_{nb,AISI}$) and initiation of buckling (P_{nb}/P_{AISI}) were 1.50 and 1.03 respectively. The average stiffness (G'_{ave}) for the 36/5 repetitions was calculated to be 11.9 kips/in (2.08 kN/mm) (Table 5).

Test repetitions 36/5-R1 and 36/5 R3 were terminated due to post-peak flattening of flutes and bearing/pull-over failures of the support fasteners (Figure 25). The 36/5 – R1 specimen had excessive flattening of the flutes at the supports as can be seen in Figure 25.a. The 36/5 – R3 repetition failed due to post peak bearing/tilting of fasteners which was followed by pull over (Figure 25.b). Repetition 36/5-R2 was terminated due to unzipping of the sidelaps caused by failure of the sidelap connections between panel 03 and panel 04 at sidelap seam 3-4 (Figure 25.b).

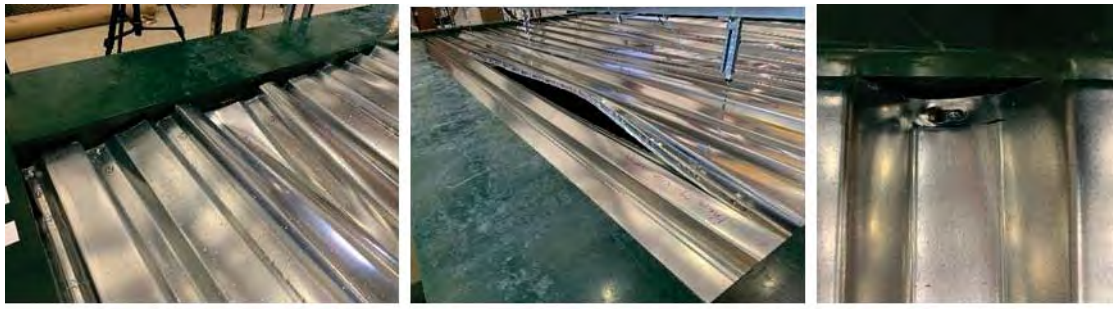

Figure 25: Observed ultimate failure modes in the 36/5 repititions:

(a) 36/5-R1 (b) 36/5-R2 (c) 36/5-R3

This occurred due to a fabrication/construction error during crimping of the panels as the overlapping ends were not sufficiently lapped to ensure a proper connection. The difference in failure mode of the connection due to the improper crimping can be seen in Figure 26. Here, when the two overlapping ends were lapped adequately, the connection failed after tearing off the overlapping edges. With the inadequate connection, the seams show minimal signs of tearing, and the connection fails due to opening of the crimp. Since the failure of the sidelap occurred in the post-peak range, the test was deemed acceptable. However, this repetition has a noticeably lower ultimate (P_{max}) capacity, 10% lower on average, when compared to other repetitions in the set.

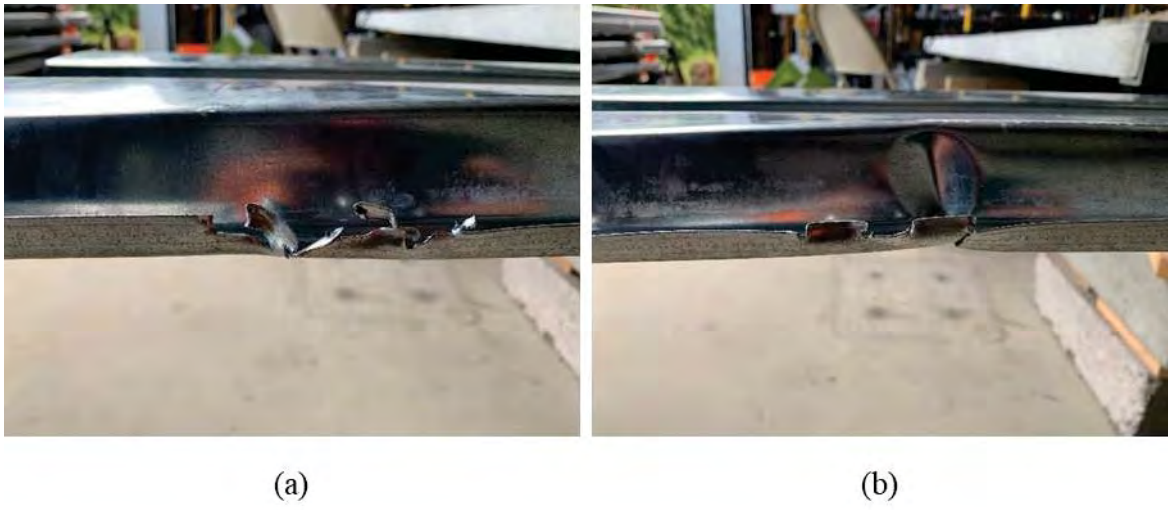

Figure 26: (a) Proper vs (b) improper sidelap connection at failure

6.4 36-4 Skip pattern specimen

The 36/4 skip pattern specimen had an average peak capacity ($P_{max,ave}$) of 14.4 kips (64.1 kN) at an average displacement (Δ_{Pmax}) of 2.21 in (56.1 mm). Initiation of out-of-plane buckling occurred at an average load ($P_{nb,ave}$) of 9.87 kips (43.9 kN) (Table 4 and Figure 17) at 0.92 in (23.4 mm) of average displacement ($\Delta_{pnb,ave}$). The average strength to code predicted capacity ratios for the maximum capacity ($P_{max}/P_{nb,AISI}$) and initiation of buckling (P_{nb}/P_{AISI}) were 1.52 and 1.05 respectively. The average stiffness (G'_{ave}) for the 36/4 repetitions was calculated to be 8.20 kips/in (1.44 kN/mm) (Table 5).

The 36/4 test repetitions were terminated due to significant warping and flattening of flutes over the supports and post peak connection failures. Pull over, pullout, bearing, edge tear out, and tilting were observed in the repetitions. The 36/4 – R1 specimen ultimately failed due to pull over of a support fastener over the west support [Figure 27(a)] Panel 01. The 36/4 – R2 specimen test run was terminated due to bearing and subsequent pull out of the fastener over the East support in Panel 01 [Figure 27(b)]. The 36/4 – R3 specimen failed due to fastener failures caused by pullout, edge tear out, and bearing/tilting over the west support [Figure 27(c) and (d)]. Significant warping present throughout the panel ends.

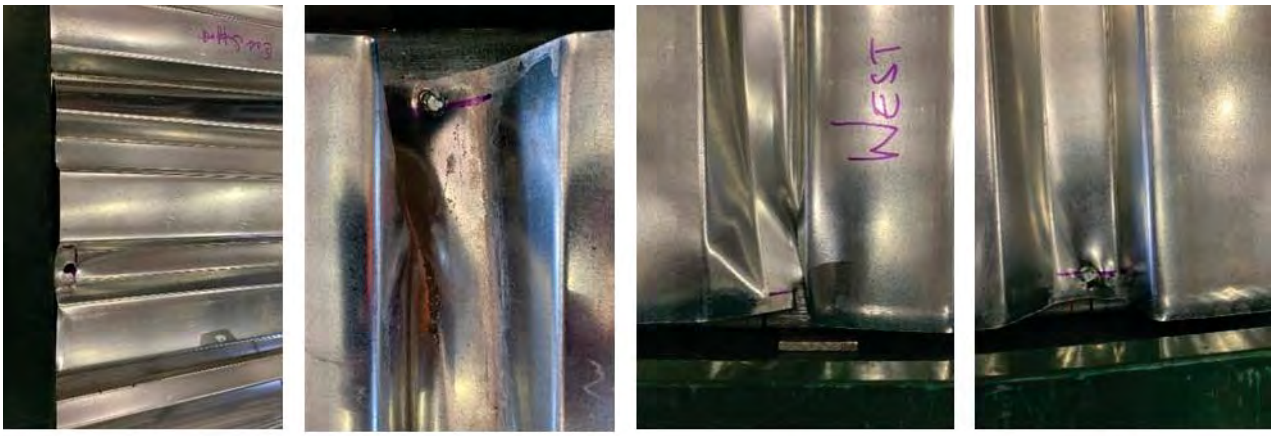

Figure 27: Select ultimate failure modes in the 36/4 repititions:

(a) 36/4-R1 – Pull over (b) 36/4-R2 – Bearing (c) 36/4-R3 – Edge tearout (d) 36/4-R3 – Tilting

6.5 Influence on buckling capacity and displacement

Changing support attachment pattern had a negligible impact on peak force (P_{max}) observed in the tests, about 7.7% average. When support fasteners were reduced from the 36/7 pattern to the reduced 35/5 and 36/4 patterns, capacity reduced by 8.3% and 7.3% respectively. However, P_{max} was achieved at varying displacement levels as can be seen in Figure 17 and Table 4. The average displacement increased from 1.50 in (38.1 mm) to 1.62 in (41.1 mm) for the 36/5 and to 2.21 in (56.1 mm) for the 36/4 pattern tests respectively. This was an increase of 7.8% for the 36/5 and 47.6% for the 36/4 repetitions. The average ultimate strength to predicted ratios ($P_{max}/P_{nb,AISI}$) for the 36/7, 36/5, and 36/4 repetitions were 1.64, 1.50, and 1.52 respectively.

Changing support attachment pattern from the 36/7 pattern to the 36/5 and 36/4 pattern reduced the load at which out-of-plane buckling initiated (P_{nb}) by 5% and 4 % respectively. The average strength to predicted ratios when comparing initiation of buckling strength with expected capacity ($P_{nb}/P_{nb,AISI}$) for the 36/7, 36/5, and 36/4 repetitions were 1.09, 1.03, and 1.05, respectively.

6.6 Influence on stiffness

Changing support attachment pattern had a significant impact on the specimen's stiffness (Figure 17 and Table 4). As support fasteners were reduced from the fully attached pattern (36/7) to the intermediate (36/5) and skip patterns (36/4), the average stiffness for the set of repetitions reduced from 24.5 kips/in (4.29 kN/mm) to 11.9 kips/in (2.08 kN/mm) and 8.20 kips/in (1.44 kN/mm) respectively. This is a 51% and 67% percent reduction for the 36/5 and 36/4 patterns, respectively, when compared to the fully attached case. The stiffness observed from the experimental tests (G'_{exp}) did not agree well with predictive methods in AISI S310 – 20 Section D5 (AISI 2020) [$mean(G'_{FEA}/G'_{AISI})$ = 0.52]. The 36/5 specimens were best predicted [$mean(G'_{FEA}/G'_{AISI})_{36/5}$ = 0.90] and the fully attached 36/7 specimens had the lowest prediction ratio [$mean(G'_{FEA}/G'_{AISI})_{36/7}$ = 0.34].

6.7 Influence on end-warping behavior

Although the ends of the specimen were not instrumented, video recordings of the tests show that the three attachment patterns exhibited different end-warping behavior. The 36/7 pattern (Figure 28) showed uniform warping across all the flutes with all the flutes warping approximately uniformly in the same direction. The 36/5 attachment pattern showed non-uniform warping behavior with differences observed in the attached and unattached flutes (Figure 29). The two fully attached flutes on either ends of the panels warped similarly and the warping behavior was different from the partially attached interior four flutes. The 36/4 specimen warped uniformly with subsequent flutes alternatingly warping upwards or downwards as can be seen in Figure 30.

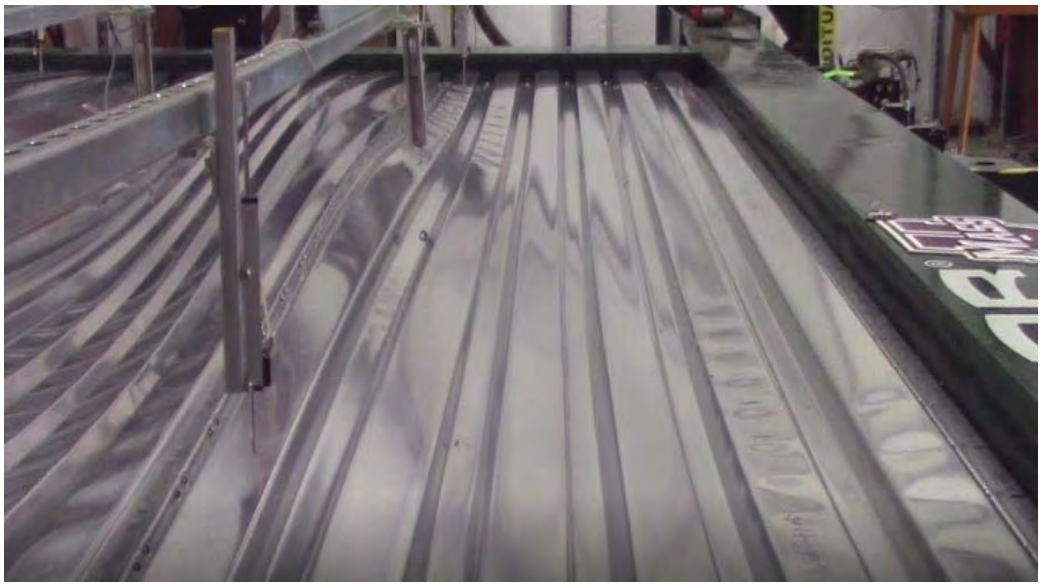

Figure 28: Typical end-warping behavior observed in the 36/7 specimens

Figure 29: Typical end-warping behavior observed in the 36/5 specimens

Figure 30: Typical end-warping beavior observed in the 36/4 specimens

7 Experimental program conclusions

To investigate the influence of industry standard support fastener attachment patterns on the AISI S310 and DDM04 panel buckling limit state, nine monotonic tests were conducted. These tests were identical in configuration except for the support attachment pattern. Three unique support attachment patterns were evaluated, and three repetitions were performed for each set. The specimens were instrumented with displacement sensors to capture the onset of buckling. Based on the observations from these tests, the following key conclusions were drawn:

- Support attachment pattern had negligible impact on the ultimate capacity (7.7%) and load at which buckling initiates (4.5%)
- Reducing support fasteners from the 36/7 pattern to the 36/5 and 36/4 patterns increased displacement at ultimate load level by 7.80% and 47.6% respectively
- Current design equations provided a conservative estimate for the ultimate capacity of the specimen (Mean test to predicted ratio = 1.55) but provided accurate estimates of the load at which out-of-plane buckling initiated (Mean test to predicted ratio = 1.05)
- Reducing support attachments from the 36/7 pattern to the 36/5 and 36/4 reduced the initial stiffness of the test specimen by 51% and 67% respectively
- Current design equations provided stiffness estimates that were significantly stiffer than experimental results (Mean test to predicted ratio = 0.52)

8 Finite element analysis (FEA) expansion

The experimental results presented in Section 6 of this report were utilized to develop and calibrate finite element analysis (FEA) models capable of capturing experimental strength and buckling behavior observed during testing. The FEA models utilized non-linear idealized material properties, idealized connection behavior, and contact definitions. The calibrated models were used to predict onset of buckling, ultimate capacities, and stiffness for 18 gauge and 20 gauge Type B deck for comparison with the predictive equation in AISI S310 (AISI 2020) and SDI DDM04 (Luttrell 2015). This section of the report presents and discusses the FEA modelling methodology, validation process, findings of the numerical simulations, and performance of predictive equations.

8.1 Numerical modelling matrix

The numerical modeling matrix for the FEA expansion can be seen in Table 6 below. The 20 gauge and 18 gauge simulation models are identical to the tested 22 gauge specimen in deck profile (Type B), span length (L_v), support member thickness, and attachment patterns (36/7, 36/5, and 36/4) and only differ in the simulated base metal thickness. This ensures that deck thickness is the only variable across the models and the effect of thickness on panel buckling capacity can be isolated.

Table 6: Numerical modelling matrix for FEA Expansion

Specimen	Attachment Pattern	L_v (ft)	Deck Thickness (in)	Support Thickness (in)
36/7 - 22 – 16	36/7	15	0.0295	0.054
36/7 - 20 – 16			0.0358	
36/7 - 18 – 16			0.0474	
36/5 - 22 – 16	36/5	15	0.0295	0.054
36/5 - 20 – 16			0.0358	
36/5 - 18 – 16			0.0474	
36/4 - 22 – 16	36/4	15	0.0295	0.054
36/4 - 20 – 16			0.0358	
36/4 - 18 – 16			0.0474	

8.2 FEA modelling methodology

Specimens based on the modelling matrix proposed in Section 8.1 were modelled and analyzed using the commercially available finite element analysis software ABAQUS Version 6.14. The following sub-sections present the modelled simplified deck and support geometry, material properties, interactions/constraints, and boundary conditions utilized for the non-linear analysis.

8.2.1 Model geometry and material properties

The FEA model geometry was defined to be identical to the tested specimens and the idealization can be seen in Figure 31 below. Three interconnected full width (36-inches) light gauge steel deck panels and one partial panel (12-inches) were modelled which were connected to the underlying frame. The overall size of the FEA model was 10 feet by 15 feet (Figure 31).

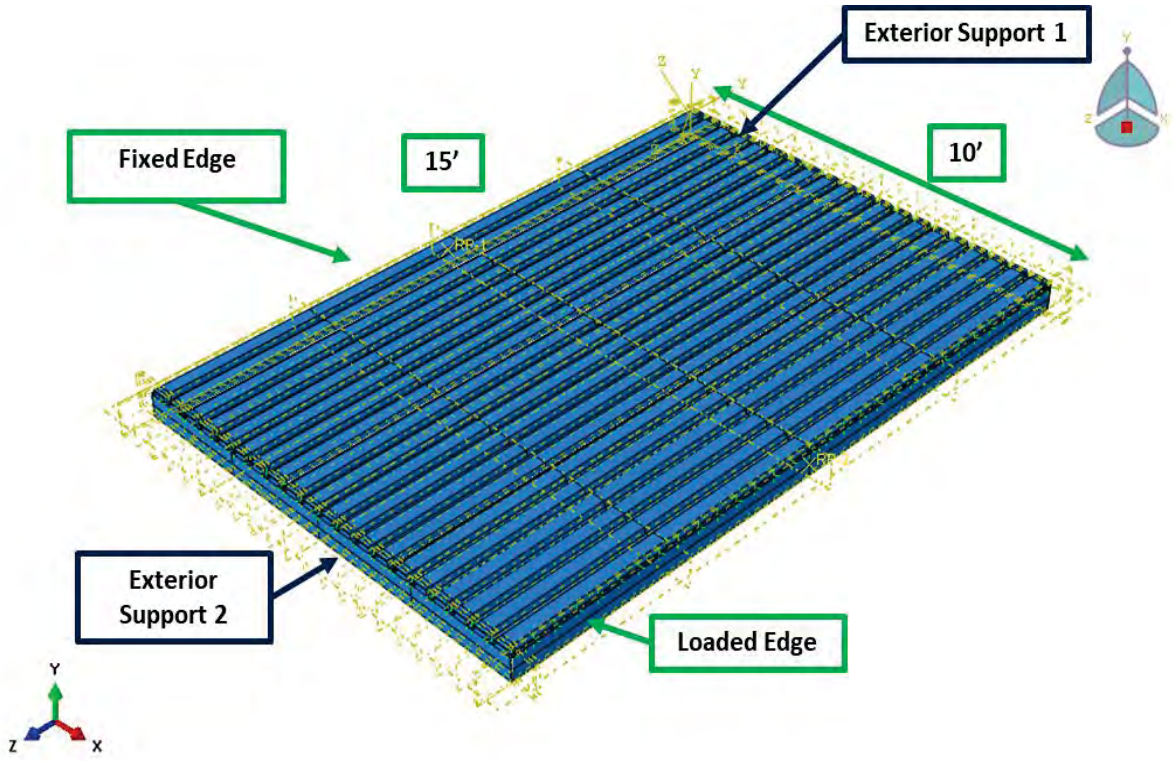

Figure 31: FEA idealization of test specimen

The light gauge steel deck was modelled with repeating configurations as can be seen in Figure 32. The dimensions for the corrugations were based on nominal dimensions provided by the deck manufacturer. The geometry of the interlocking sidelaps was simplified into 0.75-inch-high flat plates as can be seen in Figure 32 below.

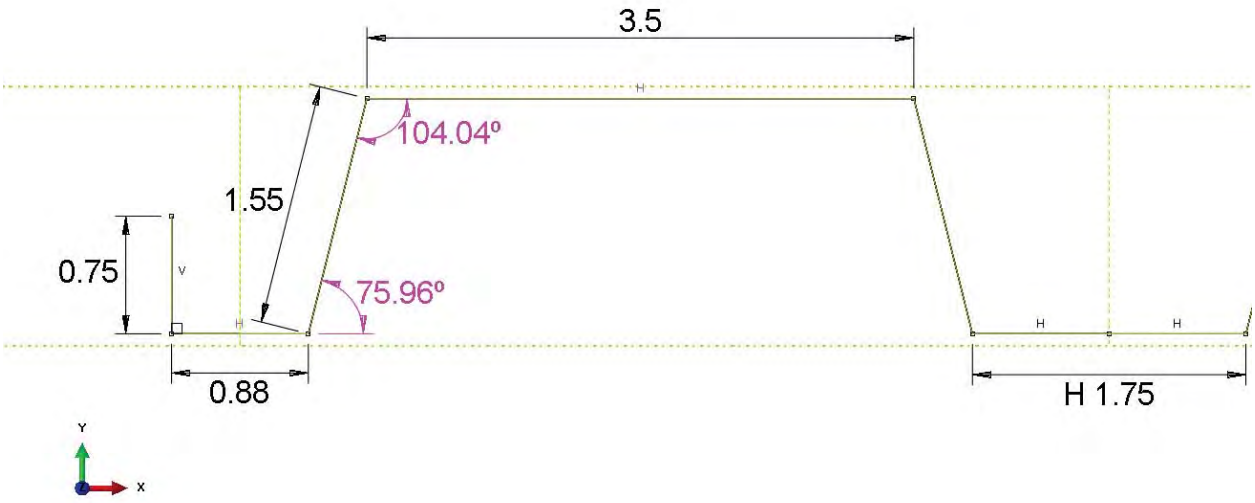

Figure 32: Repeating corrugation dimensions (in inches)

The support angles and cold-formed steel (CFS) framing members were modelled based on nominal dimensions of the framing members used in the experimental testing. The modelled cross-section geometry can be seen in Figure 33 below.

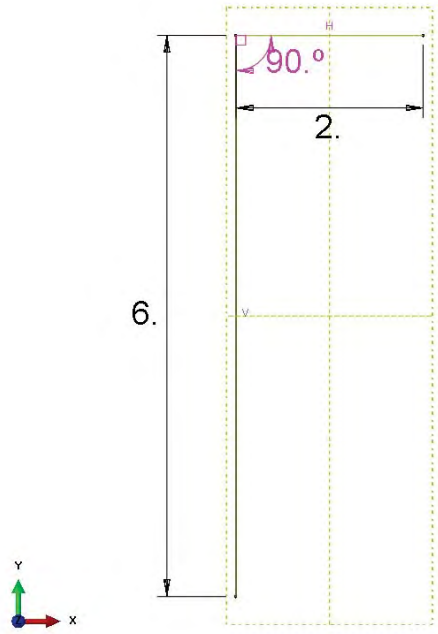

Figure 33: Cross-section dimensions of the support framing members (in inches)

An idealized bi-linear material model was utilized to model the nominal stress-strain behavior of steel (Figure 34). The yield strength, F_y, and ultimate strength, F_u, were set to 50 ksi and 65 ksi respectively. Yield point, ε_y, and elongation at failure, ε_u,were assumed to be 0.02% and 18% respectively. The modulus of elasticity, E, and Poisson's ratio was assumed to be 29,500 ksi and 0.3 respectively. Engineering stress and strain were converted to plastic stress and strain to include material plasticity in the models.

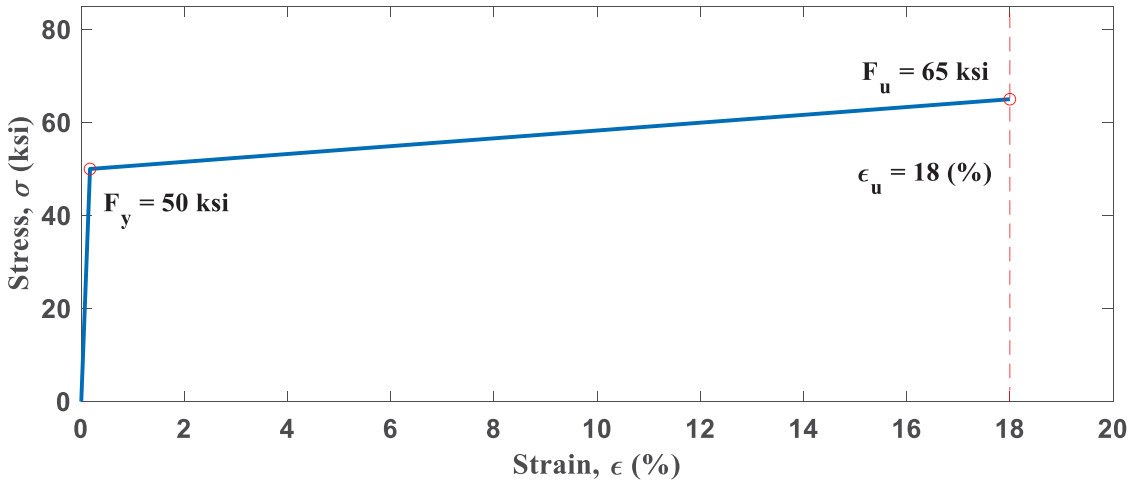

Figure 34: Idealized bi-linear stress strain curve for FEA simulations

8.2.2 Interactions and constraints

Inbuilt ABAQUS (ABAQUS 2014) multi-point constraints (MPC) and point based fasteners were utilized in the model to apply boundary conditions and simulate connections respectively. Both the fixed and load joist were constrained to reference nodes located in the middle of the joist webs using MPCs (Figure 35). These reference points were then used to restrict degrees of freedom and apply displacements in the static general load step.

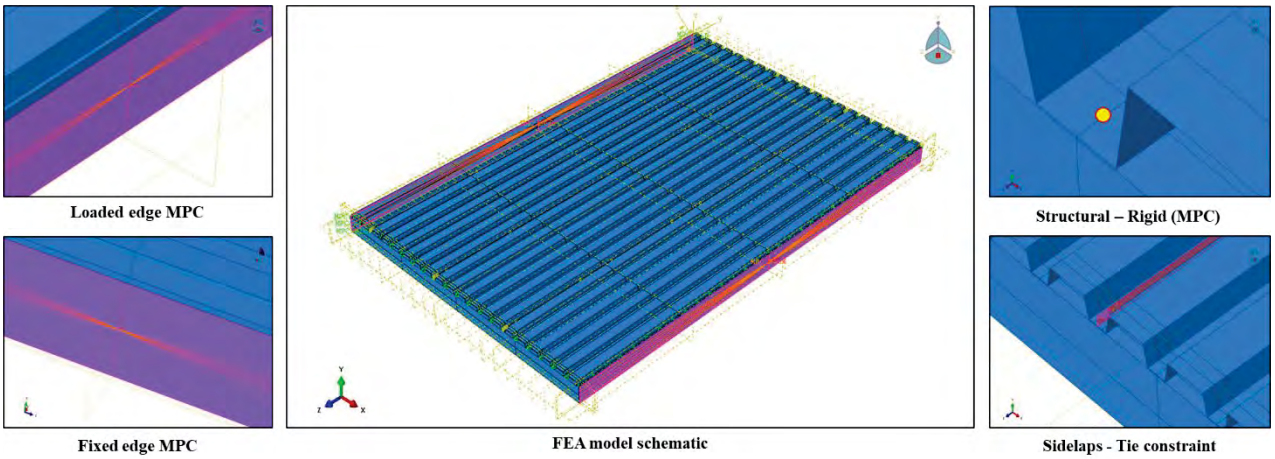

Figure 35: MPC constraints for loaded/ fixed supports and fasteners

Connections between the deck and the underlying frame were modelled using the inbuilt Abaqus point-based fasteners. The fastener behavior in U1, U2, and U3 direction was defined as a rigid MPC to prevent any slip or deformation at fastener locations. A second bi-linear fastener model was also used as an alternative to the rigid fasteners to study the influence of fastener deformation on panel buckling and stiffness. The bi-linear fastener stiffness and peak capacity were based on tests by Ta et al. (Tao et al. 2017) and the idealized behavior can be seen in Figure 36 below in orange. While the connection test was not identical to the experimentally tested configuration, it served as a reasonable approximation to determine the impact of connection models on strength and stiffness. Sidelap connections were not modelled explicitly in the FEA simulations and a tie constraint was used to join the vertical flats of the panels to simulate the interlocking deck and VSC- II connection (Figure 35). Implications of the fastener and VSC-II modelling methodology have been discussed in the results section of this report.

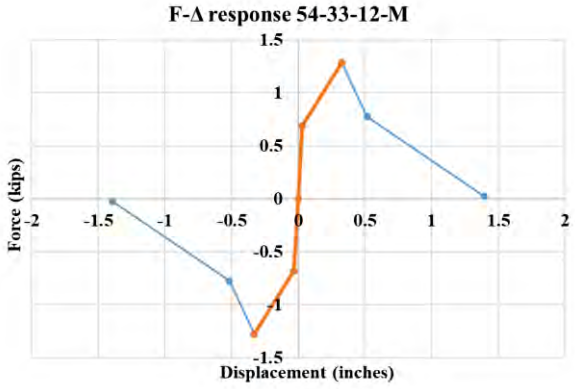

Figure 36: Fastener behavior (orange) utilized in FEA models to improve stiffness

Contacts were defined between the ends of the panels and exterior support beams and the bottom flanges of the exterior panels and free and fixed support joist flanges (Figure 37). ABAQUS default "hard" contacts were utilized in the U2 direction and "frictionless" behavior was defined in the U1 and U3 direction (ABAQUS 2014). This was done to prevent the steel panels from penetrating the underlying frame in the FEA models and to simulate realistic warping restraint at the deck ends.

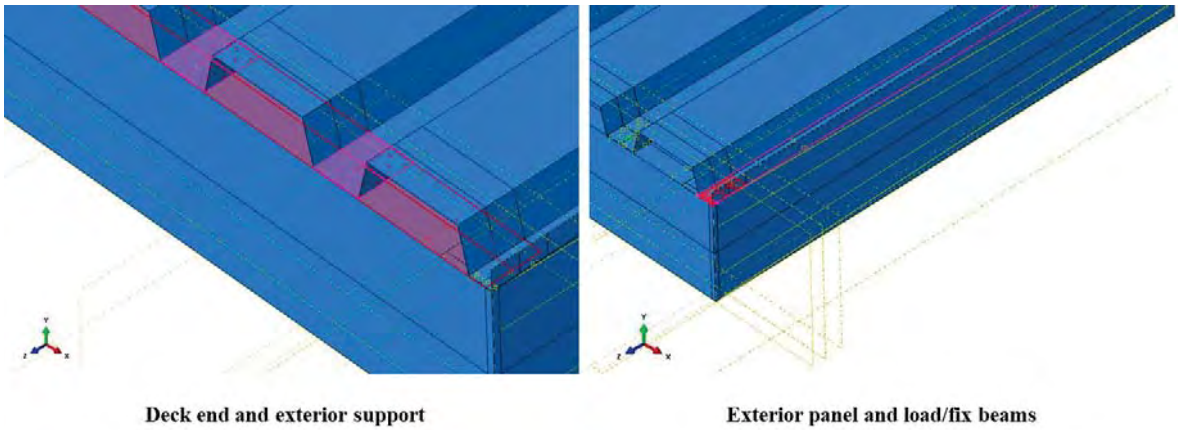

Figure 37: Contact definition locations in the model for panel ends and support members and panels edges and loaded/fixed beams

8.2.3 Meshing details

The deck panels were meshed with S4R quadrilateral shell elements with 7 integration points through the thickness. The support angles and CFS members were also modelled with S4R elements. A 0.5 in global mesh size was used to discretize the deck panel and 1.0 in global mesh size was used to discretize the support framing members.

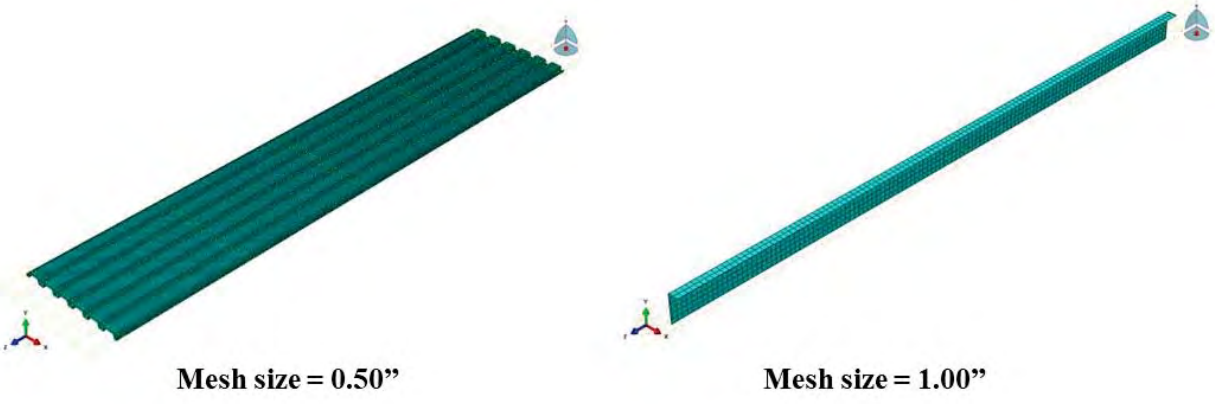

Figure 38: Discretization of steel deck panel and support framing members

8.2.4 Solvers, boundary conditions, and applied loading/displacement

A static general load step was defined to incrementally apply the displacement in the FEA simulation. Maximum iterations were set to 500 and the initial and maximum increment size was set to 0.0015 inches and 0.03 inches respectively. The minimum size was set to 3E-25 inch to aid

with convergence during the local buckling portion of the analysis. Non-linear geometry was also activated for the load step. Boundary conditions were imposed on the FEA model by restraining degrees of freedom of the underlying frame to replicate experimental conditions as can be seen in Figure 39 below. The fixed beam was restricted in all degrees of freedom (U1 = U2 = U3 = UR1 = UR2 = UR3 = 0). The free/load beam was restricted in all degrees of freedom except for U3 and U1 (U2 = UR1 = UR2 = UR3 = 0). Both exterior support beams were restricted by setting U2, UR1, and UR3 to allow these beams to pivot about their connection to the fixed beam and loaded beam. This also allowed the underlying frame to behave like a pin-jointed frame. A displacement of 3-inches was applied to the free beam in the U3 direction as was done in the experimental tests. The beam was free to move in the U1 direction.

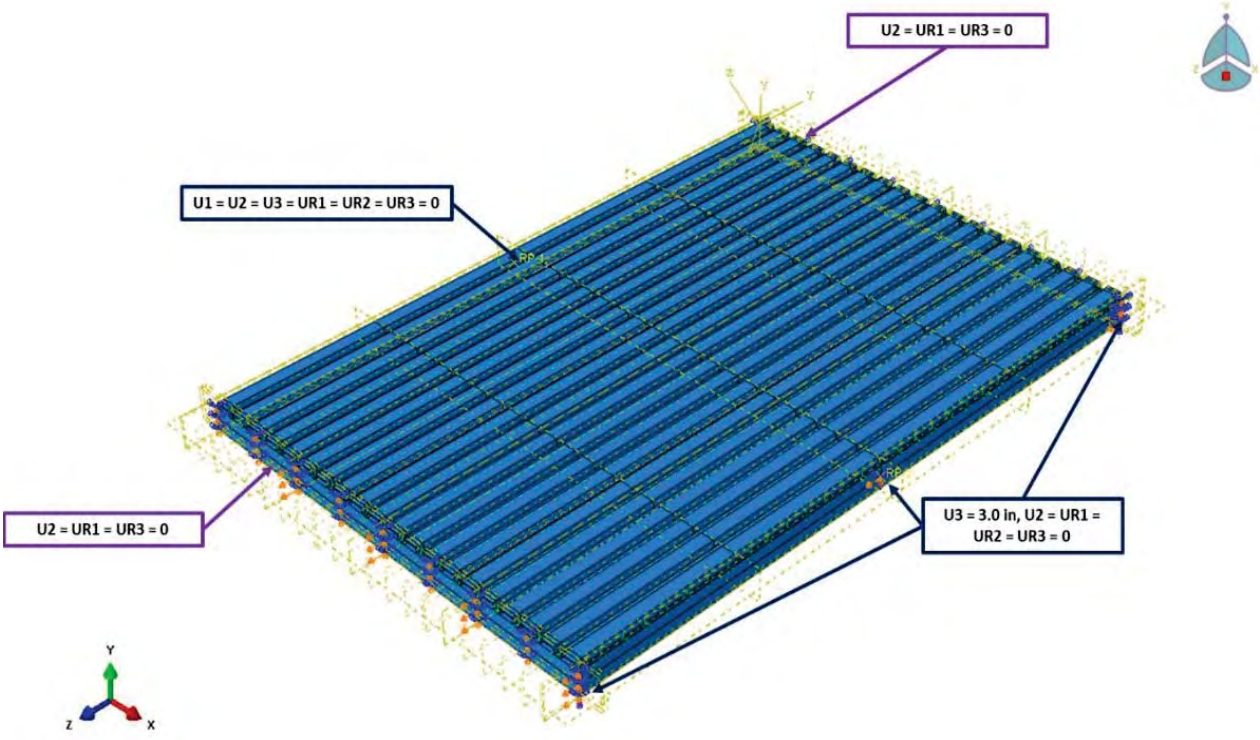

Figure 39: Applied Boundary conditions for the non-linear analysis

8.3 Comparison with experimental data

Figure 40 compares the force versus shear displacement response of the FEA models with experimental tests. The FEA models accurately precited peak capacity and mean experimental to simulated capacity ($P_{max,exp}/P_{max,FEA}$) ratio was 0.95. However, displacement at peak load (Δ_{exp}) was not accurately precited (Table 7) and the mean predicted displacement at ultimate load (Δ_{exp}) versus predicted (Δ_{FEA}) was 1.43. The FEA models were also stiffer (Table 8) than the experimental tests (Mean experimental to FEA precited stiffness ratio, G'_{exp}/G'_{FEA} = 0.78). Global (out-of-plane) buckling, local buckling, and end-warping behavior observed in the experimental tests were accurately captured by the FEA models and Figures 42 through Figure 44 compare the FEA simulations with experimental tests. The FEA models accurately predicted overall buckled shapes, local buckling near deck ends, and the end-warping behavior of flutes.

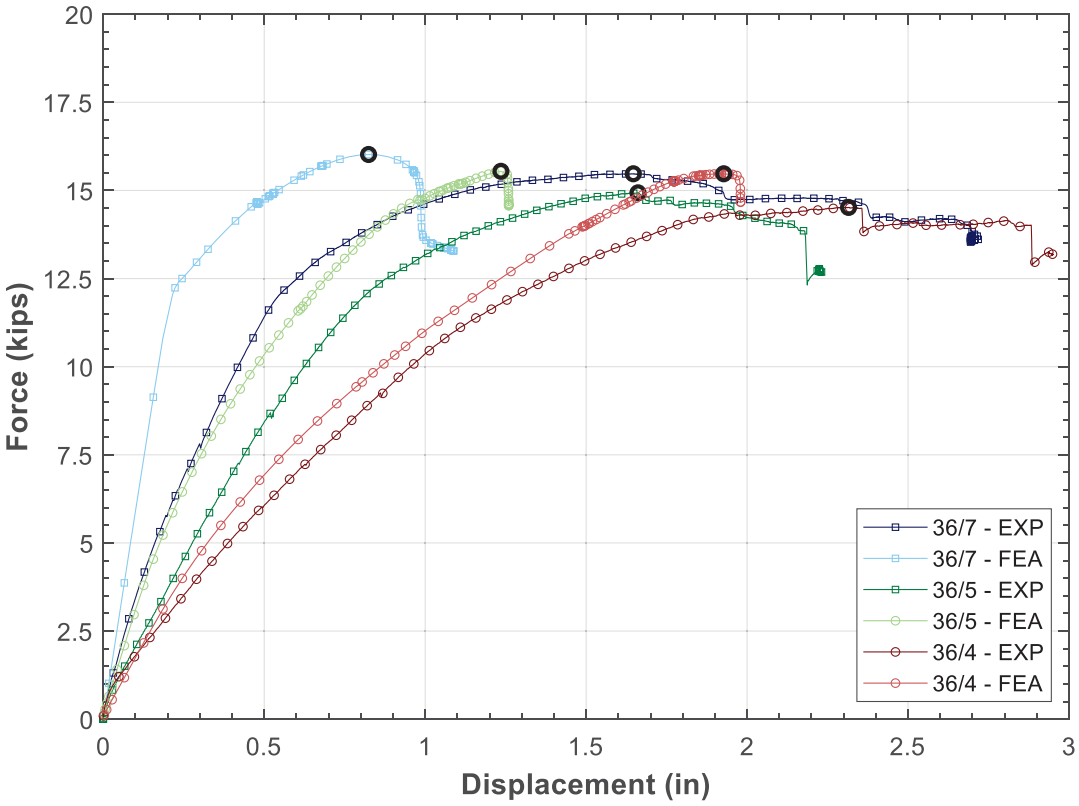

Figure 40:Comparison of experimental and FEA force displacement response

Table 7: Comparison of FEA and experimental peak strength and displacement

Configuration	$P_{max,exp}$	$P_{max,FEA}$	$P_{max,exp}/P_{max,FEA}$	Δ_{exp}	Δ_{FEA}	$\Delta_{exp}/\Delta_{FEA}$
36/7 - 22 gauge	15.48	16.02	0.97	1.50	0.82	1.82
36/5 - 22 gauge	14.93	15.54	0.96	1.62	1.24	1.31
36/4 - 22 gauge	14.36	15.47	0.93	2.21	1.93	1.15
		Mean	0.95			1.43

Table 8: Comparison of FEA and experimental stiffness and reduction in stiffness due to changing fastener pattern

				Reduction in G'			
Configuration	G'_{exp}	G'_{FEA}	G'_{exp}/G'_{FEA}	**Test**	**FEA**	**Description**	**Test/FEA**
36/7 - 22 gauge	24.46	34.08	0.72	0.66	0.73	36/7 vs 36/4	0.90
36/5 - 22 gauge	11.79	16.89	0.70	0.52	0.50	36/7 vs 36/5	1.03
36/4 - 22 gauge	8.24	9.06	0.91	0.30	0.46	36/5 vs 36/4	0.65
						Mean	0.86

Possible causes for the deviation in stiffness (G') and displacement at ultimate load (Δ) were investigated and determined to be a combination of connection stiffness and the material model utilized in the simulations. FEA models with multi-linear fastener behavior were analyzed and results were compared with experimental response (Figure 41). Coupon tests available in literature (Torabian and Schafer 2021) of identical deck from the manufacturer also showed that the steel had slightly higher elongation at failure (ε_u) of average 20% vs 18%. Material models based on the increased elongation were utilized to rerun the FEA models. The revised models showed great improvements in stiffness predictions for the 36/5 and 36/4 tests [(G'_{exp}/G'_{FEA}) = 1.11 and 0.96 respectively] but lead to convergence issues and a large increase in computational run time (more than 1500 increments). Further, negligible improvement was observed for the 36/7 simulations.

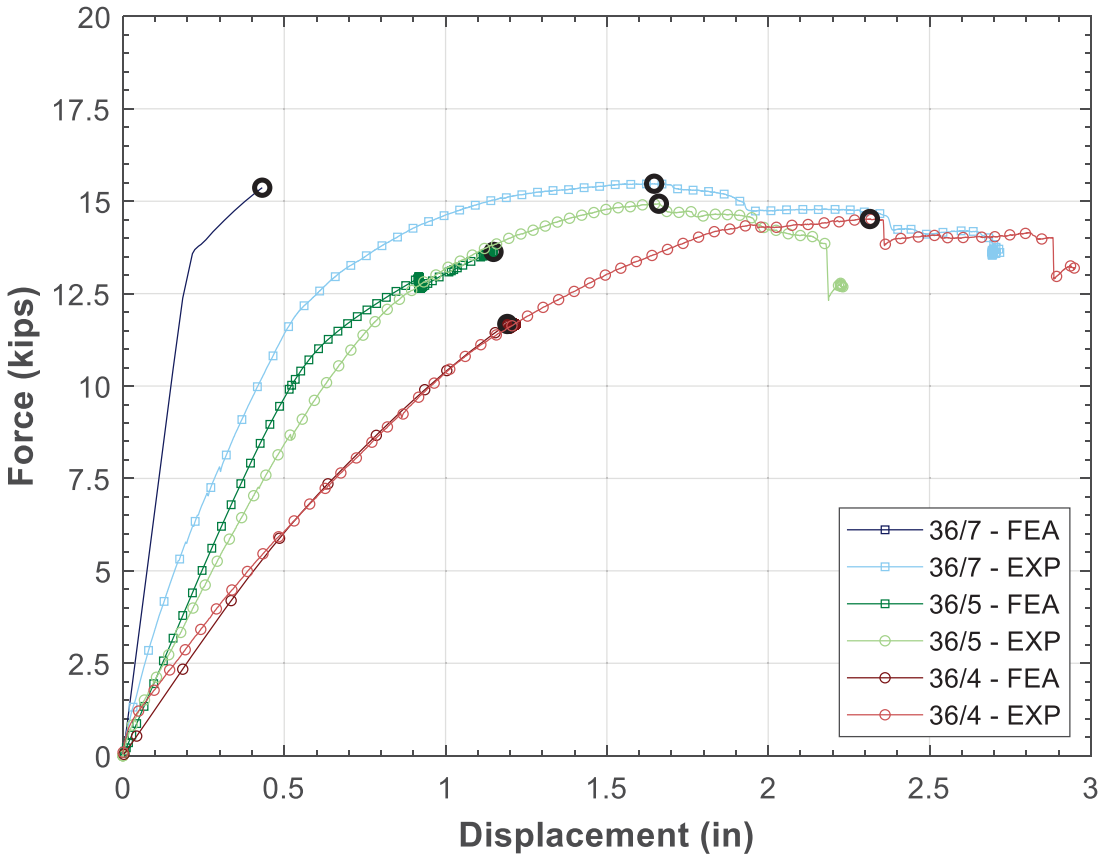

Figure 41: Comparison of experimental and FEA force displacement response with bi-linear fastener data and increased ductility material models

Although the models did not capture experimental stiffness behavior, the strength, buckling, and end-warping behavior predictions were in good agreement with experimental results. Further, the modelling methodology did not require experimental fastener data or coupon-tested material properties for strength prediction. Hence, the models were deemed suitable for predicting buckling capacities of similar untested configurations.

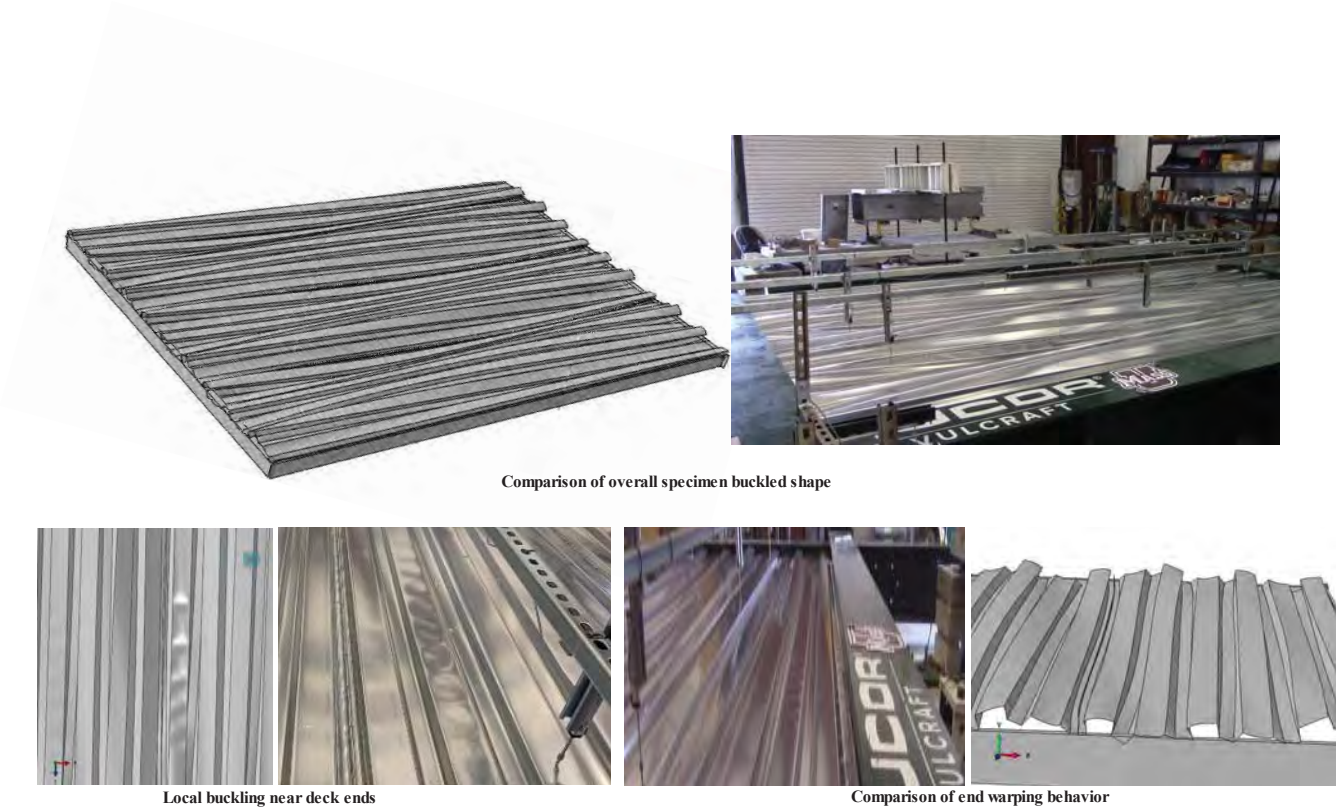

Figure 42: Comparison of FEA and experimental deformed states for the 36/4 skip pattern specimen

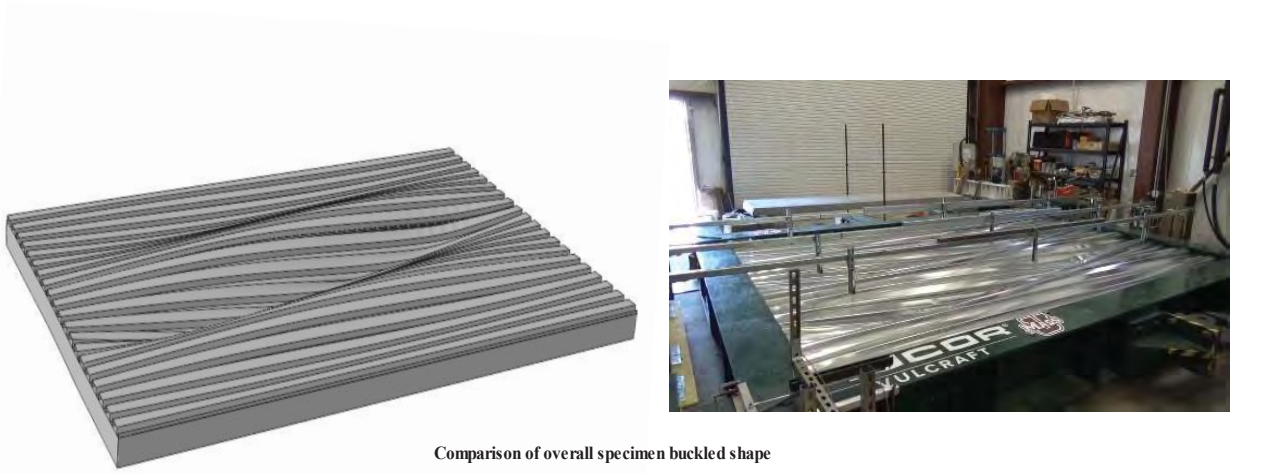

Figure 43: Comparison of FEA and experimental deformed states for the 36/5 specimen

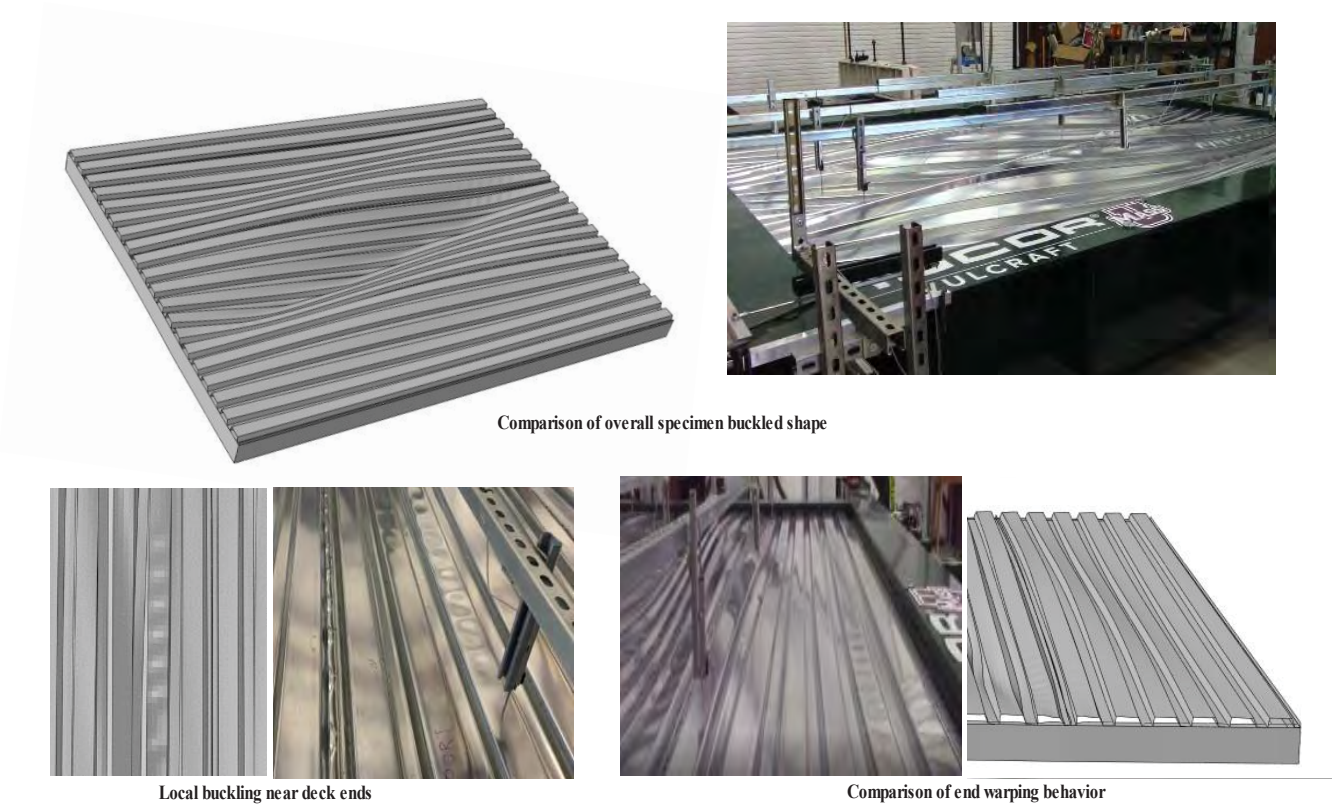

Figure 44: Comparison of FEA and experimental deformed states for the 36/7 fully attached specimen

8.4 Parametric study summary results

The FEA models developed and presented in section 8.2-8.3 were utilized to predict capacities for 20-gauge and 18-gauge Type B deck to evaluate the influence of support attachment patterns across two more commonly used deck thicknesses. The force vs. shear displacement results for the entire parametric evaluation can be seen in Figure 45 below. Table 9 summarized the observed peak strength ($P_{max,FEA}$), displacement at $P_{max,FEA}$, (Δ_{FEA}), and stiffness (G'_{FEA}).

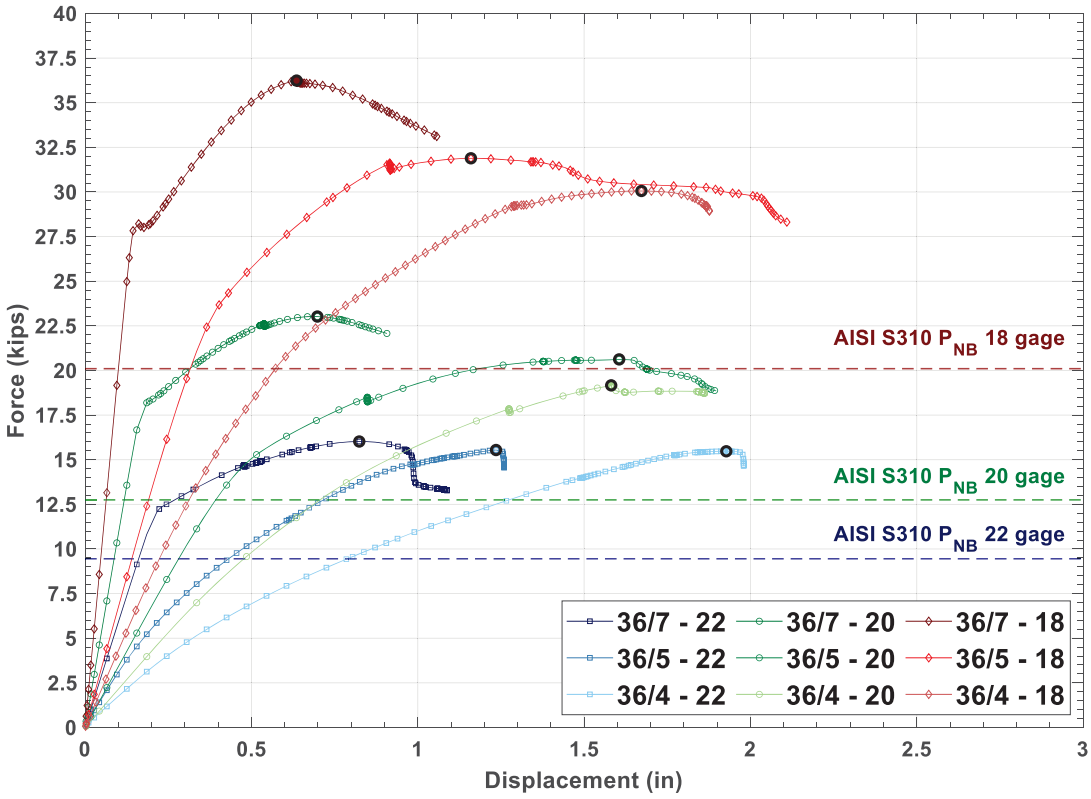

Figure 45: FEA force-shear displacement results summary

Table 9: Summary of FEA predicted ultimate cpaacities and stiffness (non-linear analysis)

Configuration	$P_{max,FEA}$ (kips)	Δ_{FEA} (in)	G'_{FEA} (kips/in)
36/7 - 22 gauge	16.02	0.82	34.08
36/5 - 22 gauge	15.54	1.24	16.89
36/4 - 22 gauge	15.47	1.93	9.06
36/7 - 20 gauge	23.02	0.70	64.39
36/5 - 20 gauge	20.62	1.61	22.41
36/4 - 20 gauge	19.17	1.58	12.93
36/7 - 18 gauge	36.24	0.64	101.36
36/5 - 18 gauge	31.89	1.16	39.49
36/4 - 18 gauge	30.06	1.67	26.48

As observed in the experimental tests, onset of buckling did not coincide with a change in overall force-displacement behavior. Hence out-of-plane displacement at midspan nodes of the FEA specimen were extracted and plotted against overall force to qualitatively determine onset of buckling. The location of measurement of out-of-plane displacement and force versus out-of-plane displacement results for the 9 configurations can be seen in Figure 46 and Figure 48 respectively. For all the specimens, the AISI S310 out-plane buckling equation provided conservative estimates for initiation of buckling as can be seen in Figure 48.

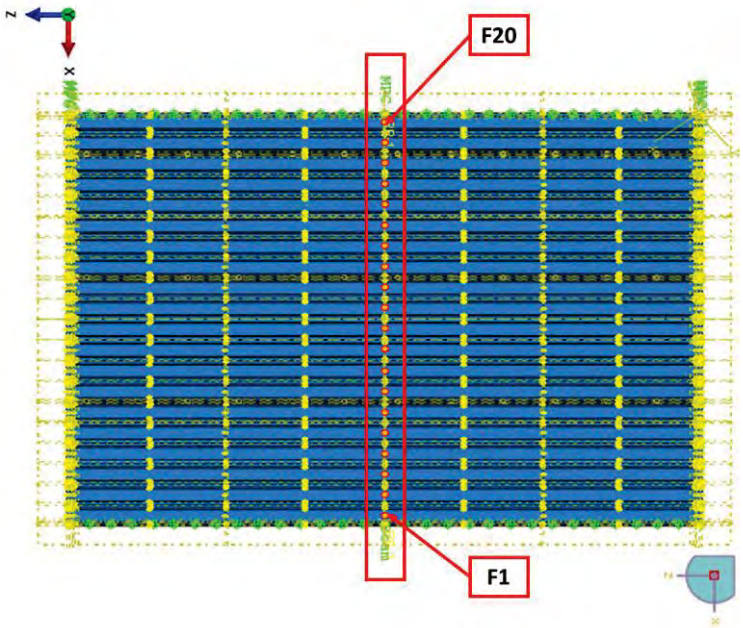

Figure 46: Location of out-of-plane displacement measurements for determining onset of buckling

Determining onset-of-buckling visually from the out-of-plane versus force results was possible for the 20-gauge and 18-gauge deck but proved to be challenging for the 22-gauge 36/5 and 36/4 attachment pattern simulations. Unlike the other 7 simulated configurations, both the 22-gauge 36/5 and 36/4 simulations did not have a clear point where sudden change in stiffness could be clearly detected (Figure 47).

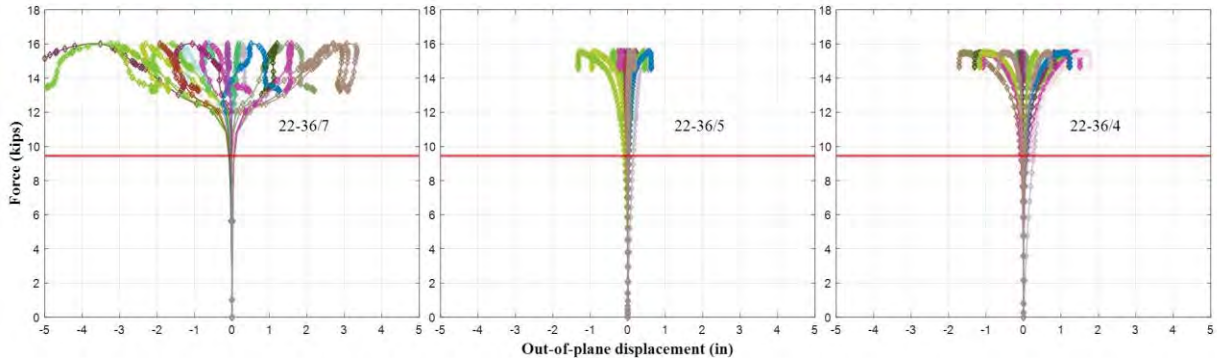

Figure 47: Comparison of out-of-plane displacement versus applied force for 22-gauge 36/7, 36/5, and 36/4 simulations

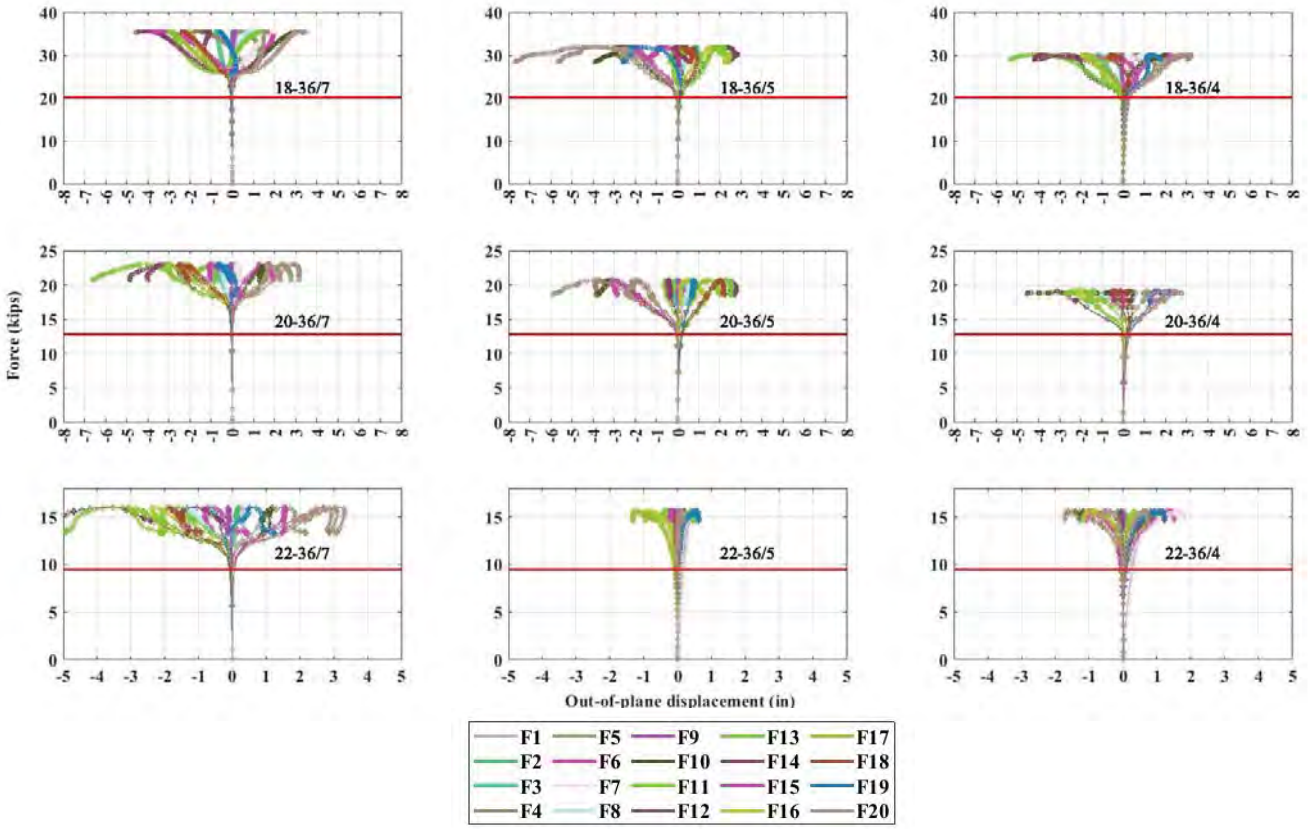

Figure 48: Summary of FEA out-of-plane displacement (Δ_z) of flutes at midspan versus applied force

8.5 Comparison with predictive methods

The ultimate capacity ($P_{max,FEA}$) and stiffness (G') predicted by the FEA models were compared with predictive equations from AISI S310 – 20 (AISI 2020) and DDM04 (Luttrell 2015). The following subsections discuss the performance of the predictive equations.

8.5.1 Comparison of predicted capacity from AISI S310 - 20 (AISI 2020) with ultimate capacity from FEA

The ultimate capacities ($P_{max,FEA}$) predicted by the FEA models were compared with capacities ($P_{nb,AISI}$) predicted by Equation D2-1 (Equation 1 in this report) from AISI S310 - 20 (AISI 2020). Table 10 summarizes the measured (FEA) to predicted (AISI) ratios for the parametric evaluation. The FEA models predicted significant overstrength in the out-of-plane buckling limit state [$mean(P_{max,FEA}/P_{nb,AISI})$ = 1.50], but these capacities were achieved well into the non-linear range of the force-displacement response and after initiation of out-of-plane buckling (Figure 45 and Figure 48). Also, from experimental testing, it was observed that the peak capacity achieved is highly dependent on connection integrity and behavior (Experimental specimen 36/5 R1/R3 vs 36/5 R2) and hence can vary based on connection detailing. Further, there was a drop in capacity in the FEA simulations when comparing the fully attached simulations (36/7) with partial attachments (36/5 and 36/4) for the 18-gauge and 22-gauge deck. This reduction was about 6% and 17% when comparing the fully attached (36/7) pattern with the intermediate (36/5) and skip (36/4) patterns respectively. However, the predictive equation predicted buckling capacities that coincided well with onset of buckling and hence no modifications have been suggested.

Table 10: Comparison of non-linear analysis predicted capacities and AISI S310 -20 Section D2 capacities (AISI 2020)

Configuration	thickness	$P_{max,FEA}$	$P_{nb,AISI}$	$P_{max,EEA}/P_{nb,AISI}$
	(in)	(kips)	(kips)	(--)
36/7 - 22 gauge	0.0300	16.02	10.59	1.51
36/5 - 22 gauge	0.0300	15.54	10.59	1.47
36/4 - 22 gauge	0.0300	15.47	10.59	1.46
36/7 - 20 gauge	0.0358	23.02	13.84	1.66
36/5 - 20 gauge	0.0358	20.62	13.84	1.49
36/4 - 20 gauge	0.0358	19.17	13.84	1.39
36/7 - 18 gauge	0.0474	36.24	21.57	1.68
36/5 - 18 gauge	0.0474	31.89	21.57	1.48
36/4 - 18 gauge	0.0474	30.06	21.57	1.39
			Mean	1.50
			St. Dev	0.10

8.5.2 Comparison of predicted stiffness from AISI S310 -20 (AISI 2020) with stiffness from FEA

The stiffness (G'_{FEA}) predicted by the FEA models were compared with stiffness (G'_{AISI}) predicted by following the procedure outlined in Section D5 from AISI S310 - 20 (AISI 2020). Table 11 summarizes the measured (FEA) to predicted (AISI) ratios for the parametric evaluation. The FEA models were more flexible than the AISI predictions [$mean(G'_{FEA}/G'_{AISI})$ = 0.67] and there was high variability associated with the predictions. The intermediate attached pattern (36/5) was best predicted [$mean(G'_{FEA}/G'_{AISI})_{36/5}$ = 0.80] and the fully attached pattern (36/7) [$mean(G'_{FEA}/G'_{AISI})_{36/7}$ = 0.56] had the highest difference in prediction. The reduction in stiffness predicted by the FEA models when attachment pattern was changed from 36/7 to 36/5 and 36/4 was on average 59% and 76% respectively. In comparison, the experimental predicted reductions when attachment pattern was changed from 36/7 to 36/5 and 36/4 was on average 52% and 66% respectively.

Table 11: Comparison of non-linear analysis predicted stiffness and AISI S310 – 20 stiffness (AISI 2020)

	P_{max}	Δ_{pmax}	G'_{FEA}	G'_{AISI}[1]	G'_{FEA}/G'_{AISI}
Configuration	**(kips)**	**(in)**	**(kips/in)**	**(kips/in)**	**(--)**
36/7 - 22 gauge	16.02	0.82	34.08	72.90	0.47
36/5 - 22 gauge	15.54	1.24	16.89	18.70	0.90
36/4 - 22 gauge	15.47	1.93	9.06	13.61	0.67
36/7 - 20 gauge	23.02	0.70	64.39	103.41	0.62
36/5 - 20 gauge	20.62	1.61	22.41	28.67	0.78
36/4 - 20 gauge	19.17	1.58	12.93	21.06	0.61
36/7 - 18 gauge	36.24	0.64	101.36	173.44	0.58
36/5 - 18 gauge	31.89	1.16	39.49	55.29	0.71
36/4 - 18 gauge	30.06	1.67	26.48	41.24	0.64
				Mean	0.67
				St. Dev	0.12

8.6 FEA parametric study conclusions

To investigate the influence of industry standard support fastener attachment patterns on the AISI S310 -20 (AISI 2020) and DDM04 panel buckling limit state, a FEA modelling methodology was developed to predict capacity for nine unique configurations. The FEA modelling methodology was validated against experimental results and utilized non-linear idealized material properties, idealized connection behavior, and contact definitions. The calibrated models were used to predict onset of buckling, ultimate capacities, and stiffness for 18-gauge, 20-gauge, 22-gauge Type B deck. These simulations were identical in configuration except for the support attachment pattern and base metal thickness. Based on the observations from these numerical simulations, the following key conclusions were drawn:

- Developed FEA models can capture experimental strength with high accuracy (Experimental/FEA = 95%) and predict buckling (local and global) and end warping behavior
- Stiffness predicted by the FEA models is higher than that observed during experimental testing [mean(Experimental/FEA = 78%)]. This difference is largest for the 36/5 intermediate attached specimen (observed/predicted = 70%)
- Improved stiffness prediction is possible with more involved fastener models [mean(Experimental/FEA = 89%)] and measured material properties, but such models can cause convergence issues and add significant runtime
- Reduction in stiffness when comparing the fully attached specimen with intermediate and skip patterns show good agreement with reductions observed during experimental testing (Experimental/FEA = 90% and 103% for 36/7 versus 36/5 and 36/4 respectively)
- FEA models show similar trends in peak capacity as observed in experimental testing and a significant reserve was observed after initiation of out-of-plane buckling
- A reduction (6% and 17% average) in peak capacity was observed in the FEA models when comparing the fully attached 36/7 specimens with the 36/5 and 36/4 specimens
- In the FEA simulations and experimental tests, onset of buckling was observed to not coincide with a notable change in the overall force-displacement response. While predicting onset of buckling visually through sensor/out-of-plane displacement buckling data is possible, a homogenous method is required to uniformly predict initiation and required for assessing the accuracy of the panel buckling equation

9 Recommended future works

To further understand the influence of end connectivity on the stability behavior of light gauge steel panels, the following future works are recommended –

- Development of robust FEA models capable of accurately predicting stiffness in addition to buckling capacity and behavior. Stiffness prediction greatly depends on material properties (E, F_y, F_u, ε_y, ε_u) as well as fastener behavior. ASTM 8 compliant coupon tests are recommended for accurately capturing material behavior. Further, support and sidelap fastener tests are recommended for determining multi-linear connection behavior inputs for the FEA models.
- Developed models should be used to predict behavior for a variety of commercially available deck cross section types (For example Type N deck, Type F, Dovetail deck, shallow deck, etc.) and at a range of spans (L_v). Additionally, the newly added limit state of local buckling should also be investigated by varying panel end support lengths. End warping behavior should also be included as an objective of the study as stiffness greatly depends on it and FEA models can provide detailed warping behavior.
- Predictions of the FEA models should be spot checked with full-scale experiments to verify the accuracy of the models and recalibrate if necessary.

References

ABAQUS (2014). ABAQUS standard version 6.14-4, Dassault Systems Simulia Corp.

AISI. (2016a). "North American standard for the design of profiled steel diaphragm panels, (AISI S310-16)." American Iron and Steel Institute

AISI. (2016b). "North American specification for the design of cold-formed steel structural members, (AISI S100-16)." American Iron and Steel Institute

AISI. (2017). "Test standard for cantilever test method for cold-formed steel diaphragms, (AISI S907)." American Iron and Steel Institute

AISI. (2020). "North American standard for the design of profiled steel diaphragm panels, (AISI S310-20)." American Iron and Steel Institute

Army, Navy and Air Force. (1982). "Seismic design for buildings, (Tri-services Manual). Report No. Army TM 5-809-10." Washington, D.C.: U.S. Government Printing Office

Castaneda. H. (2022). "Lateral response of cold-formed steel diaphragms with variable sheathing." *Doctoral Dissertations,* University of Massachusetts, Amherst Libraries.

Easley, J.T. (1975). "Buckling formulas for corrugated metal shear diaphragms." *Journal of the structural division*, 101, 1403-1417.

Hlavacek, V. (1968). "Shear instability of orthotropic panels." *Acta Technica CSAV*, 1, 134–158.

Luttrell, L.D. (2004). "Diaphragm Design Manual, 3rd Edition (DDM03)." Steel Deck Institute

Luttrell, L.D. (2015). "Diaphragm Design Manual, 4th Edition (DDM04)." Steel Deck Institute

Nunna, R, V. (2011). "Buckling of profiled steel diaphragms" Center for Cold-Formed Steel Structures Library. 163

IAPMO (2018). "Uniform evaluation report." International Association of Plumbing and Mechanical Officials

O'Brien et al. (2017). "Characterizing the load-deformation behavior of steel deck diaphragms using past test data." Cold-formed steel research consortium report series.

Sputo, T. (2017). Steel Deck on Cold-Formed Steel Framing Design Manual (SDCFSFDM), 1st Edition." Steel Deck Institute

Tao et al (2017). Monotonic and cyclic response of single shear cold-formed steel-to-steel and sheathing-to-steel connections (AISI RP17-2)." American Iron and Steel Institute

Torabian, S., Schafer, B.W. (2021). "Cyclic Experiments on Sidelap and Structural Connectors in Steel Deck Diaphragms." *Journal of structural engineering*, 147, 1403-1417.

Wright, H. D., Hossain, K.M. (1997). "In-plane shear behavior of profiled steel sheeting" *Thin-Walled Structures*, Elsevier, 29 (1-4) 79-100.

A. Appendix A – Test rig

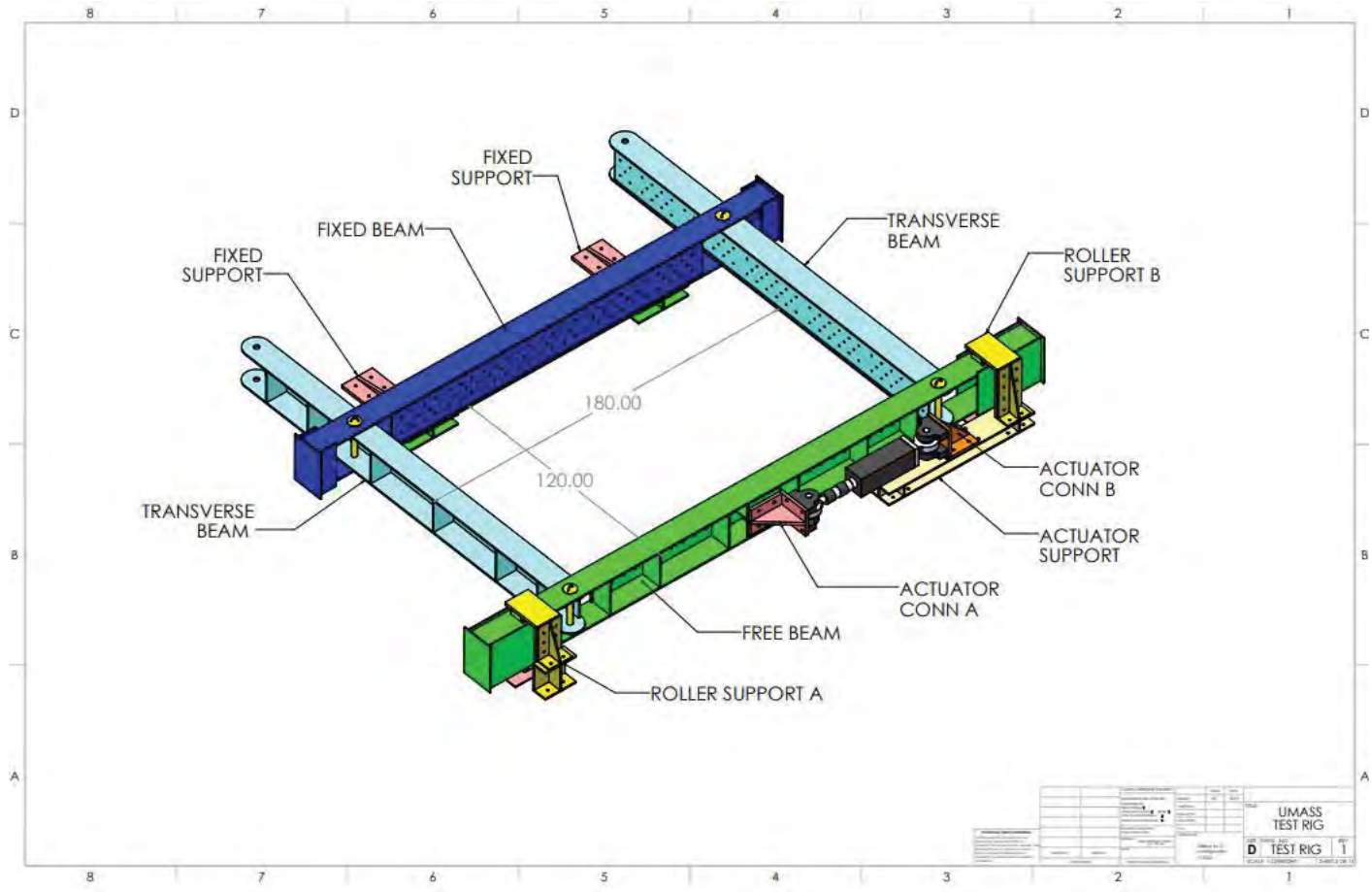

Figure 49: Overall test-rig schematic (Castaneda 2022)

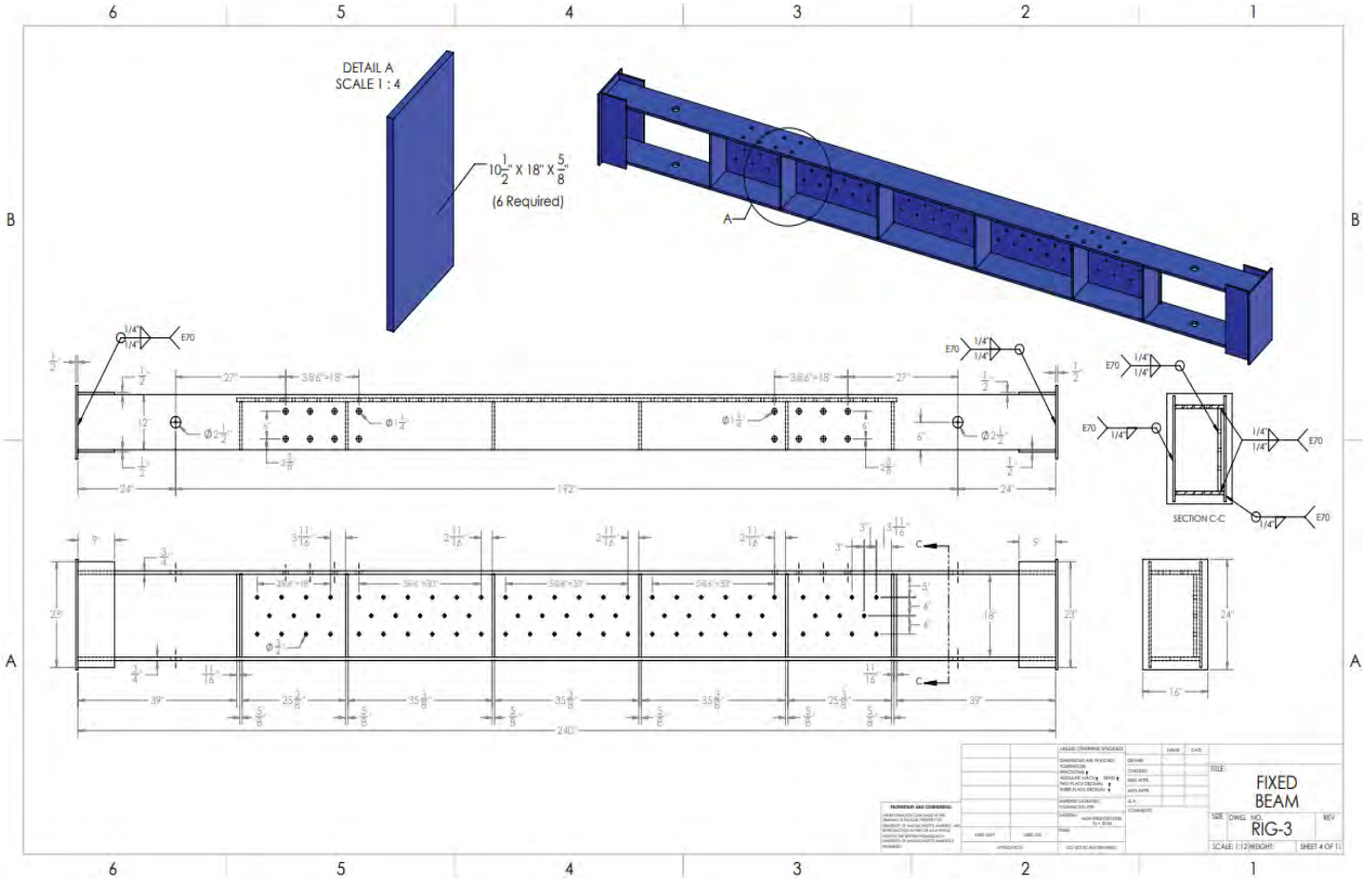

Figure 50: Fixed beam details (Castaneda 2022)

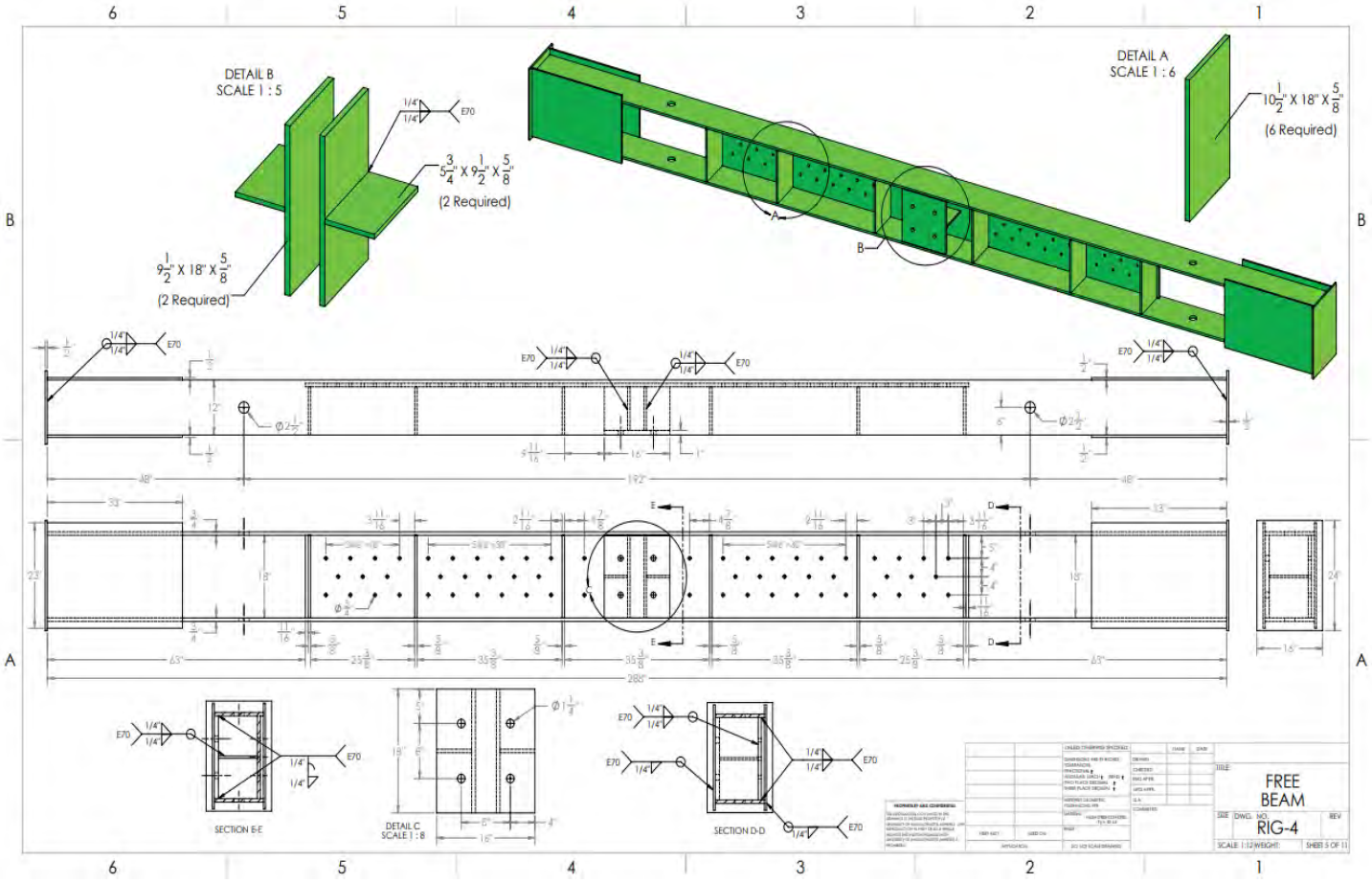

Figure 51: Free/Load beam details (Castaneda 2022)

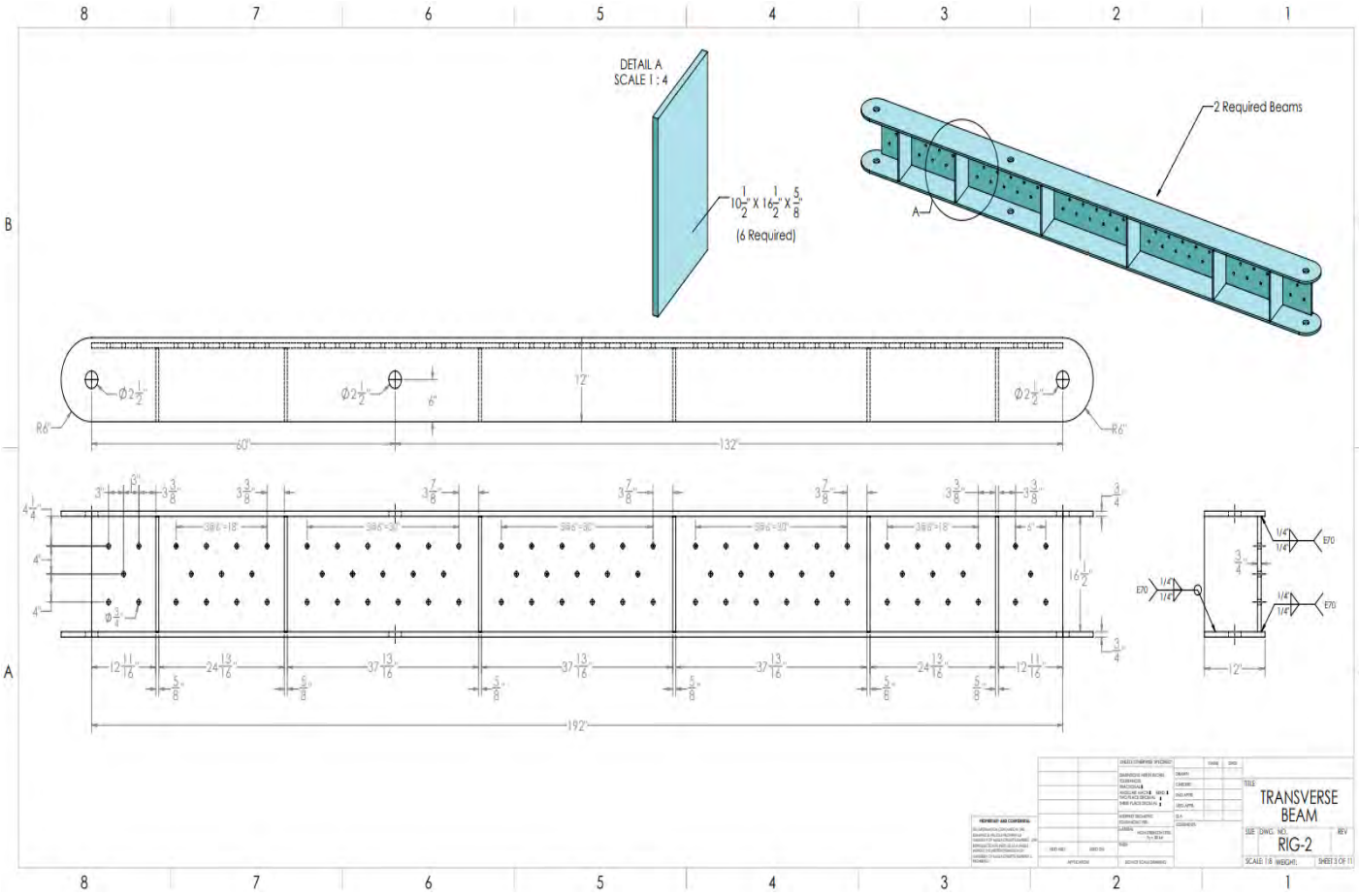

Figure 52: Transverse beam details (Castaneda 2022)

B. Appendix B – Sensor layout and loading protocol

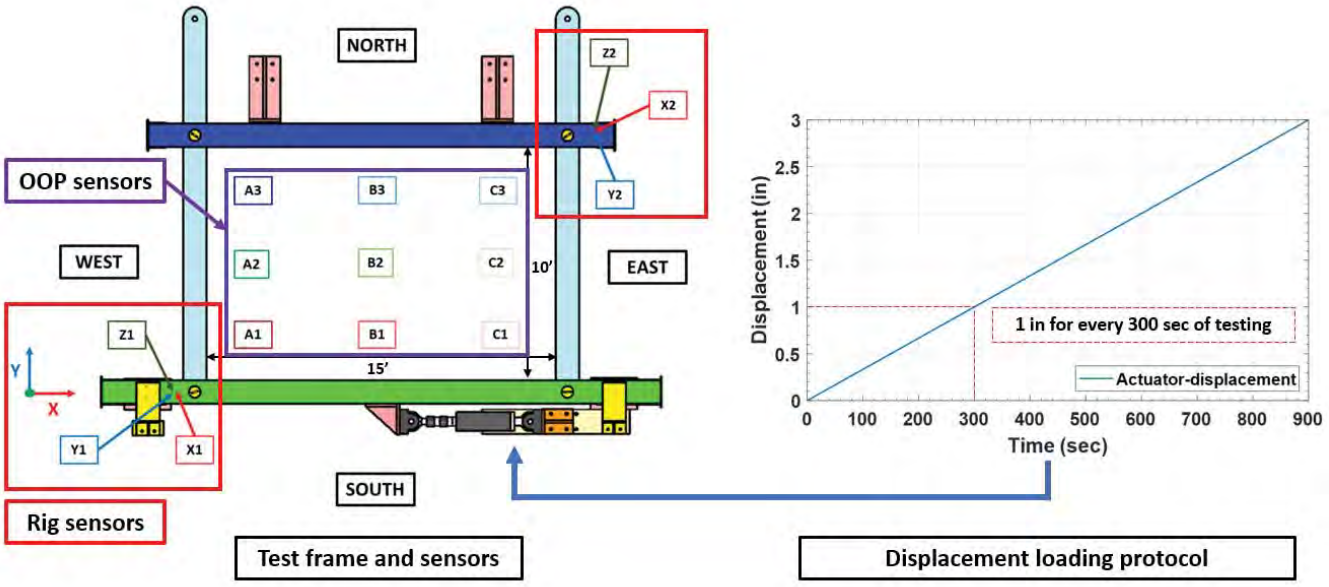

Figure 53: Sensor layout and loading protocol

C. Appendix C – Detailed per-specimen experimental results

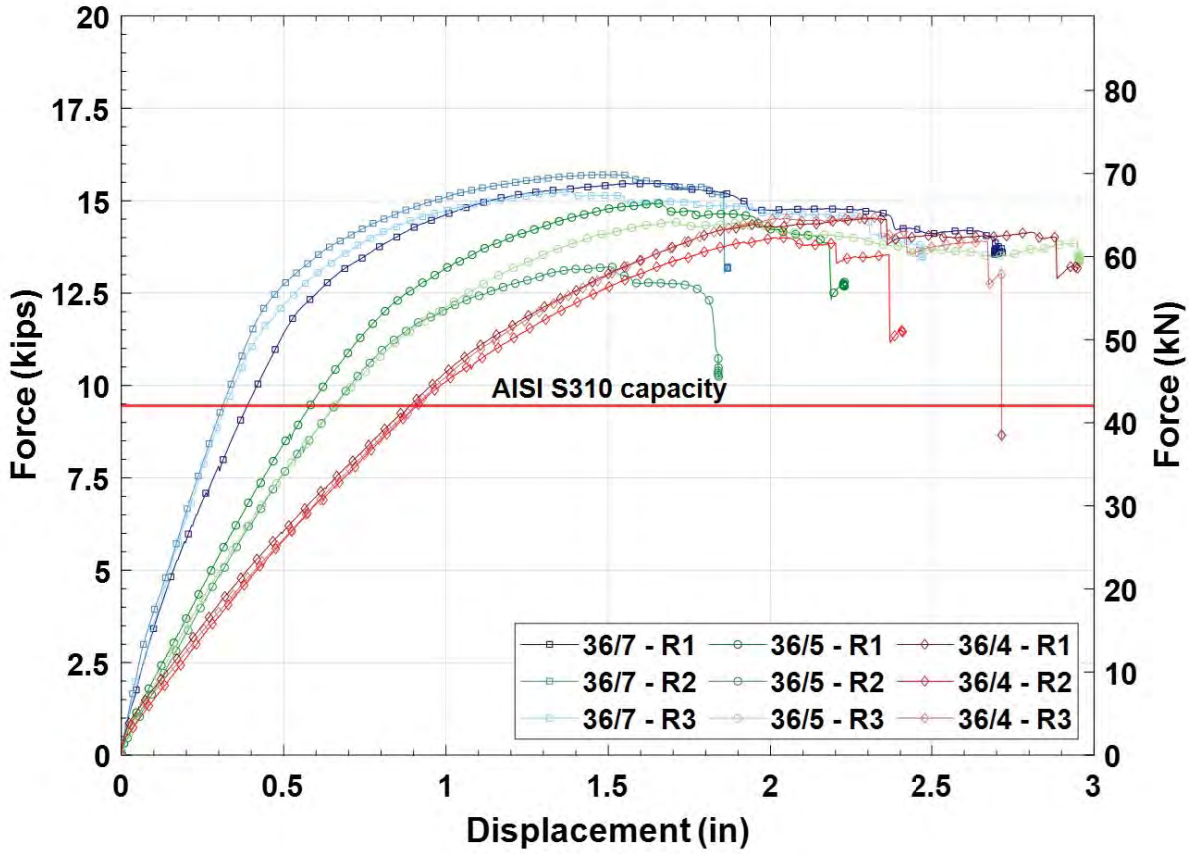

Figure 54: Actuator force displacement summary (Full page)

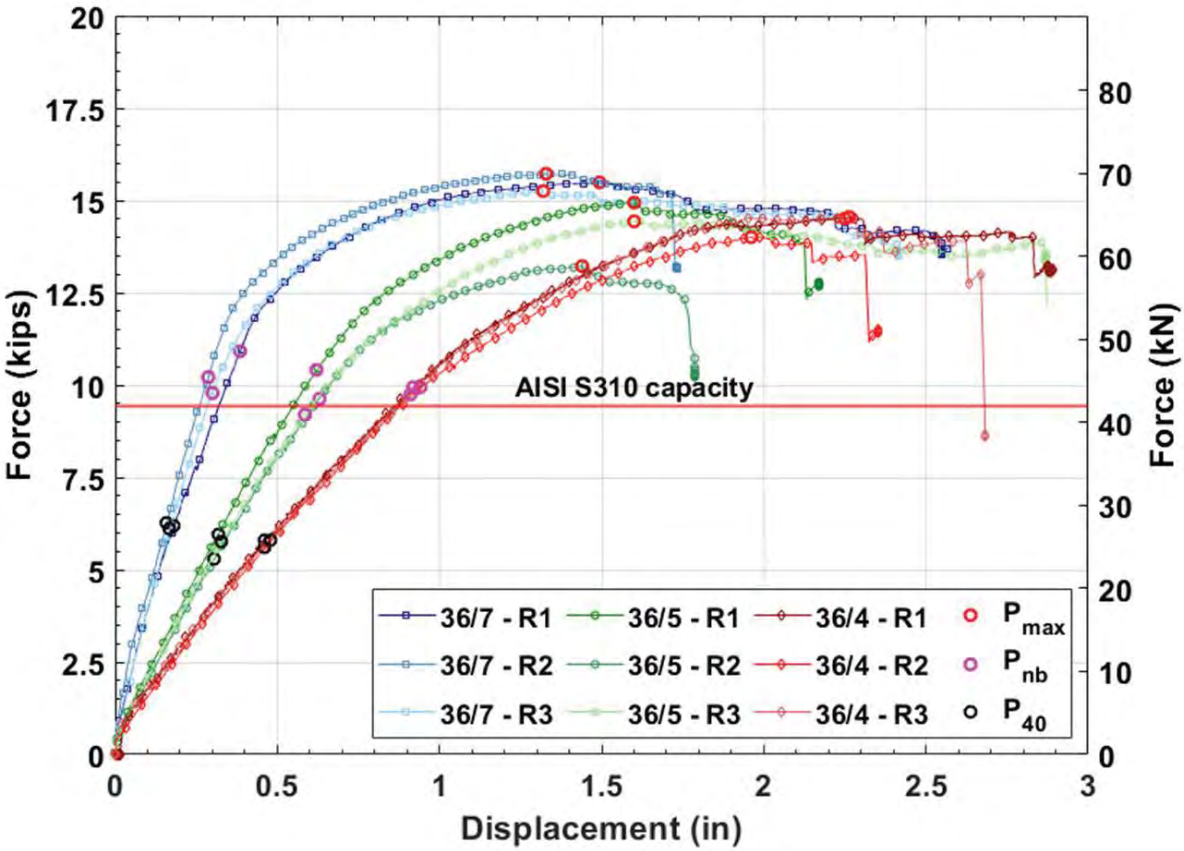

Figure 55: Shear force-displacement summary (Full page)

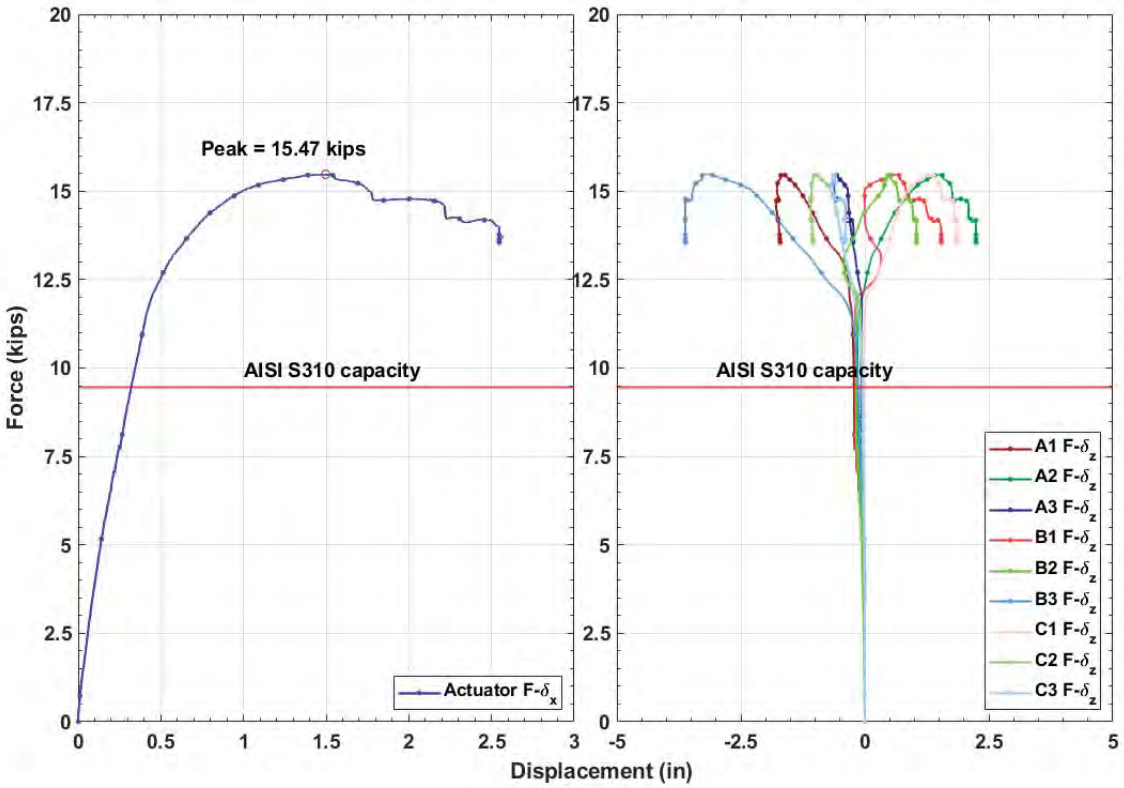

Figure 56: 36-7-R1: Actuator and Sensor force-displacement results

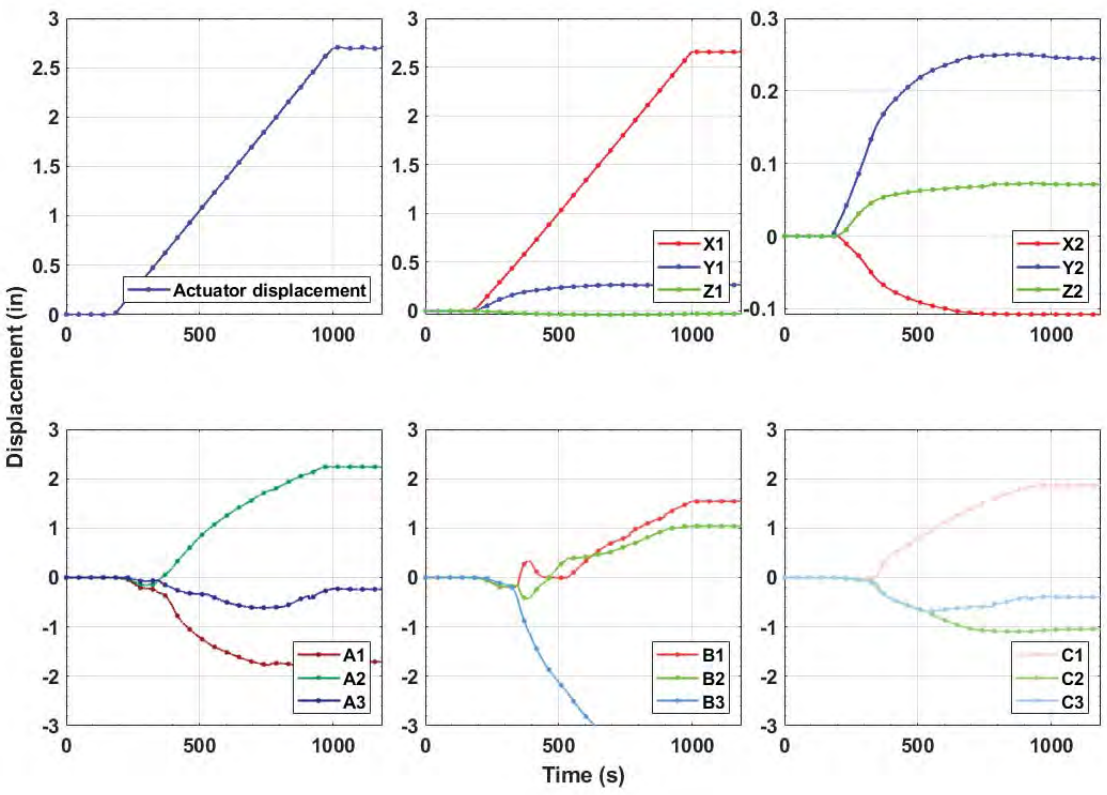

Figure 57: 36-7-R1: Actuator and Sensor displacement time data

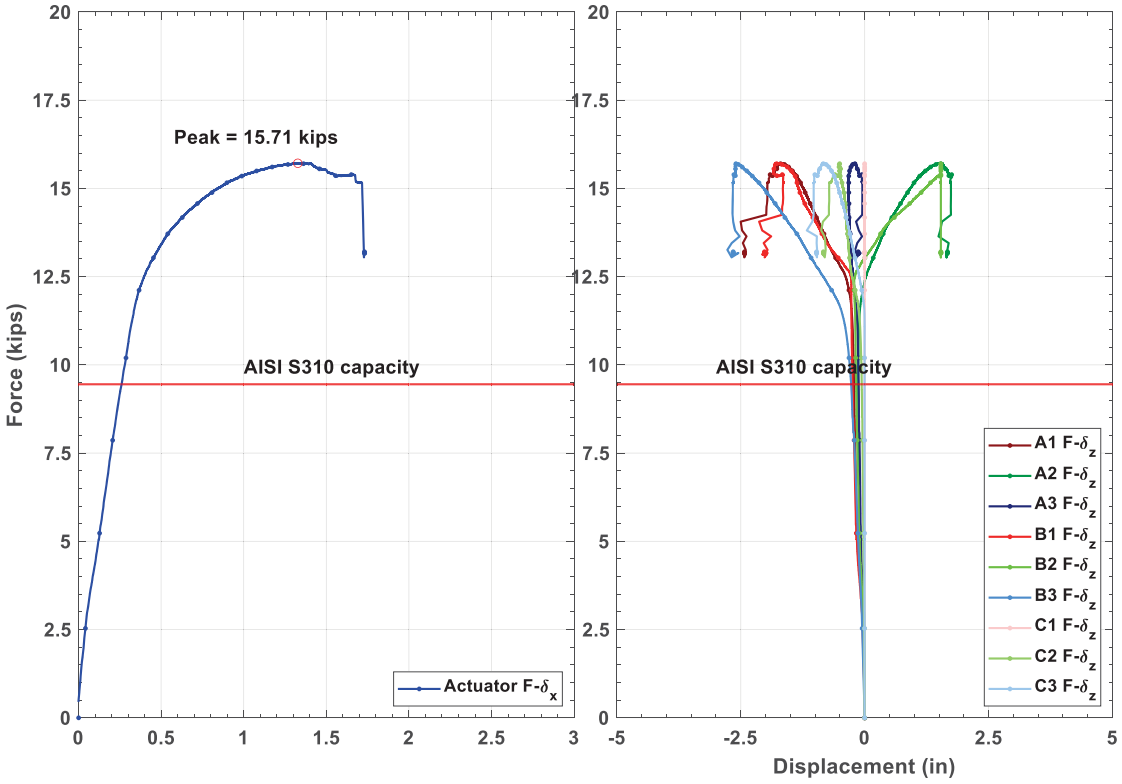

Figure 58: 36-7-R2: Actuator and Sensor force-displacement results

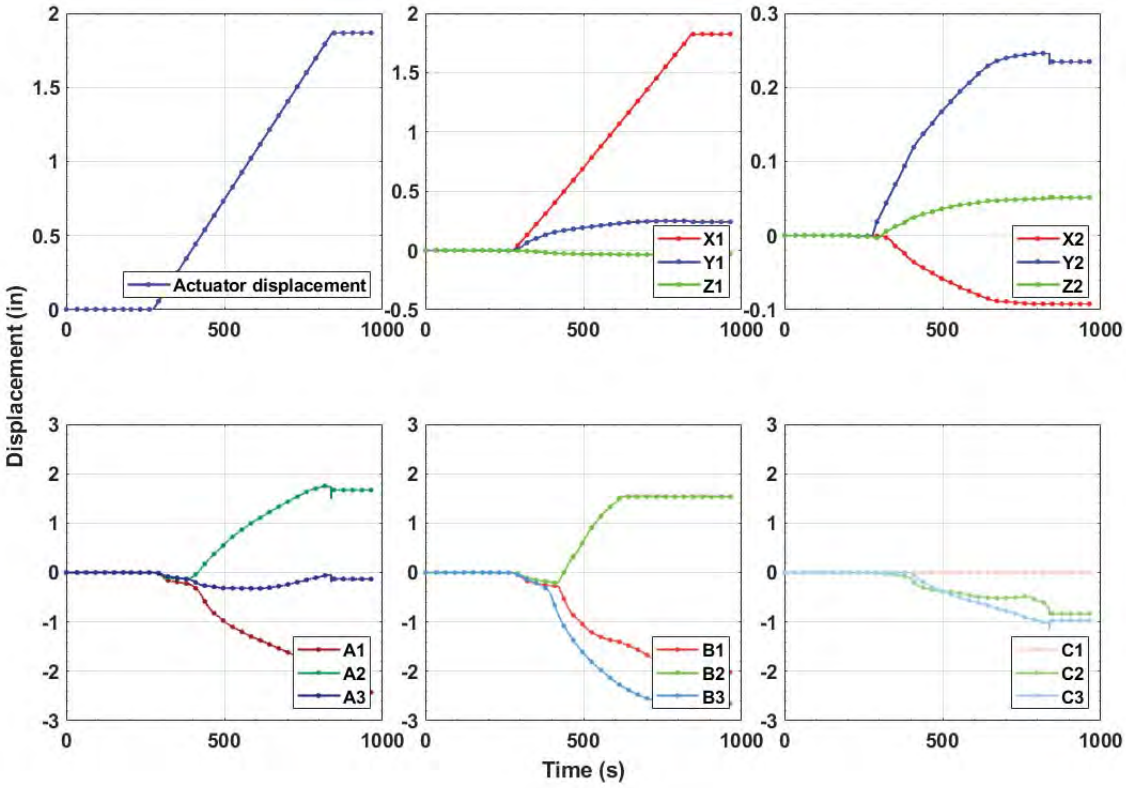

Figure 59: 36-7-R2: Actuator and Sensor displacement time data

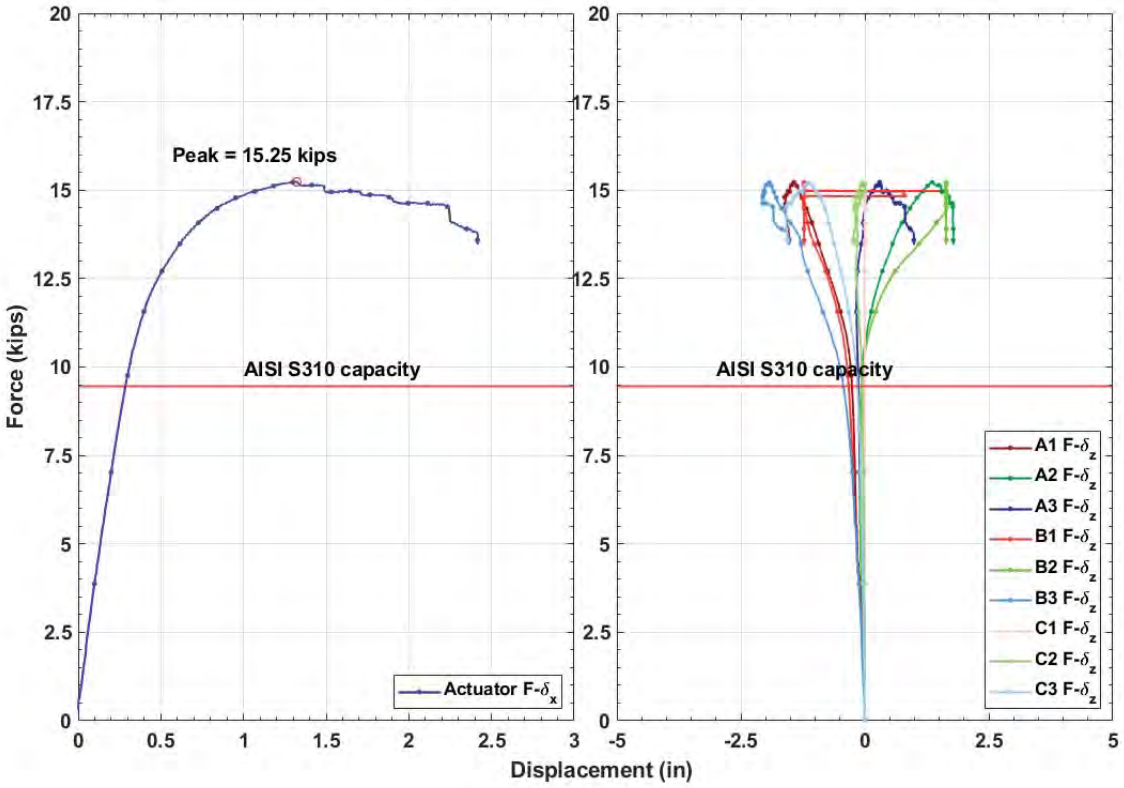

Figure 60: 36-7-R3: Actuator and Sensor force-displacement results

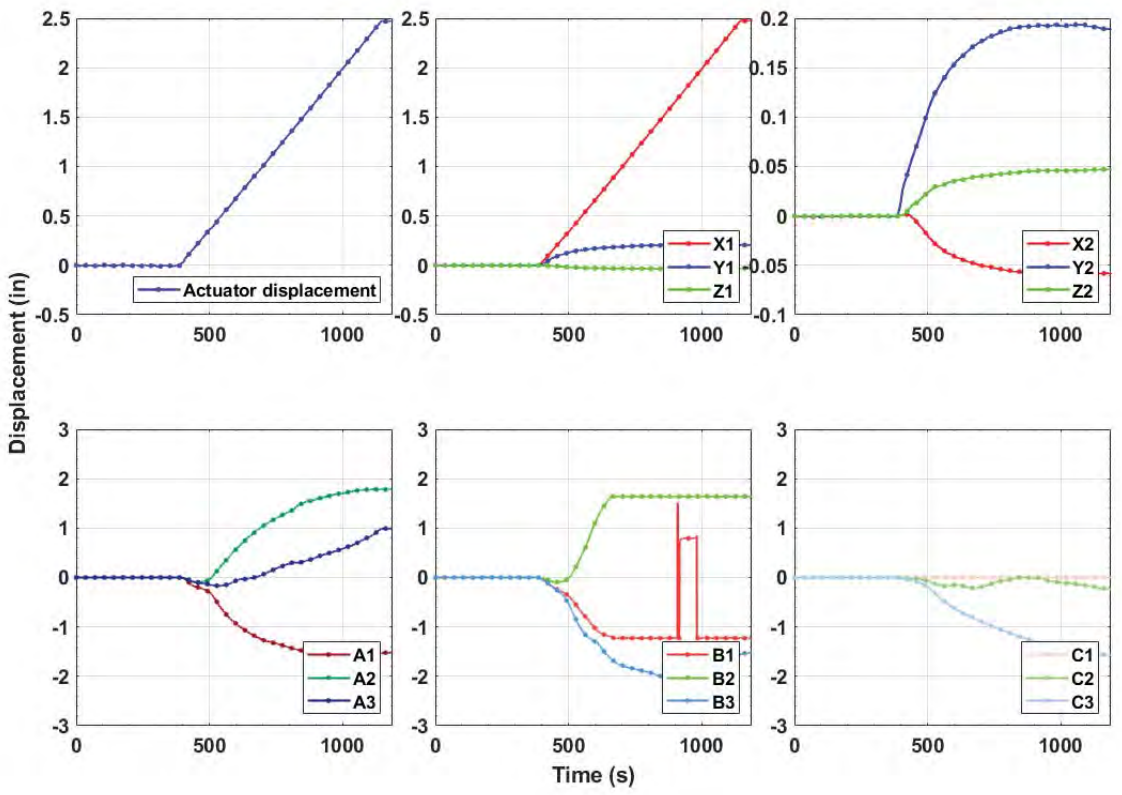

Figure 61: 36-7-R3: Actuator and Sensor displacement time data

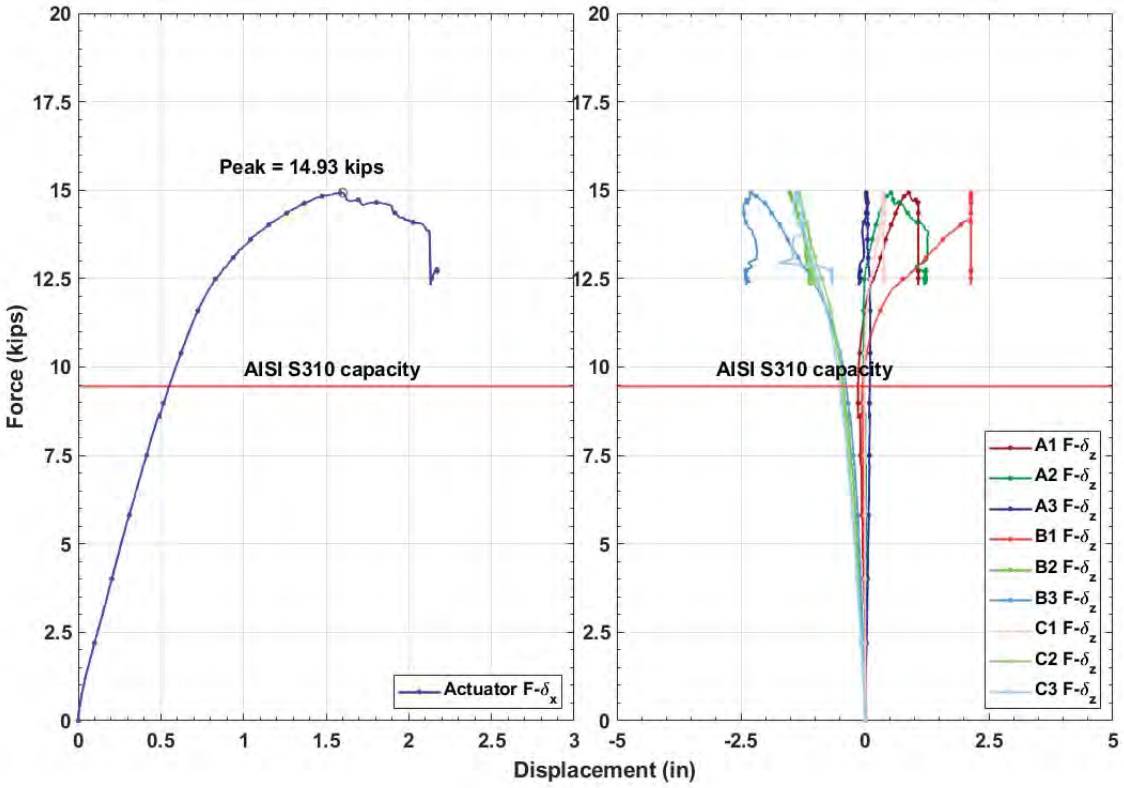

Figure 62: 36-5-R1: Actuator and Sensor force-displacement results

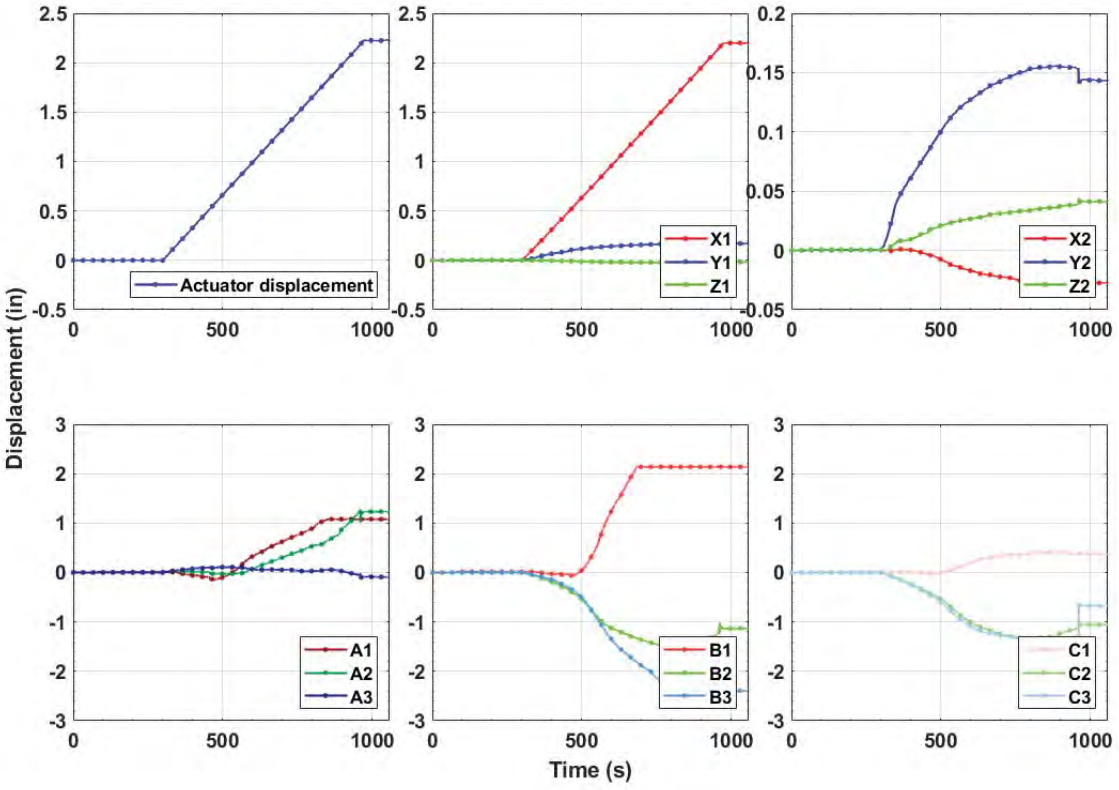

Figure 63: 36-5-R1: Actuator and Sensor displacement time data

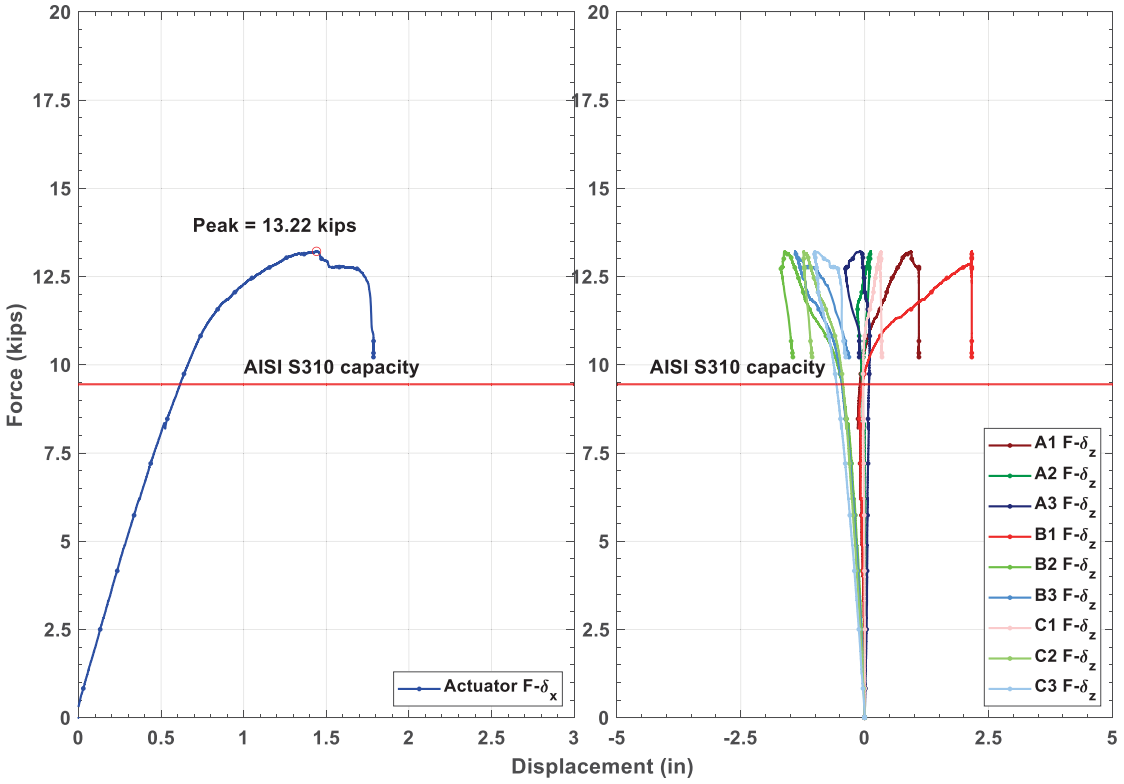

Figure 64: 36-5-R2: Actuator and Sensor force-displacement results

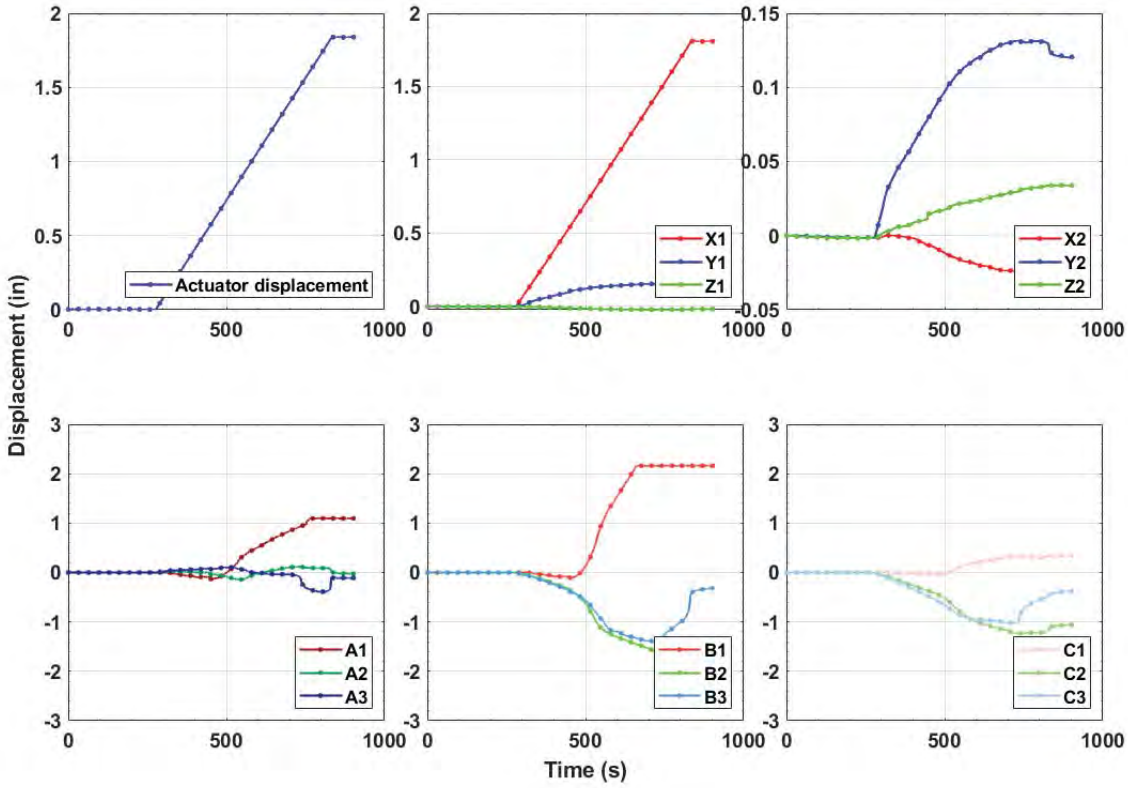

Figure 65: 36-5-R2: Actuator and Sensor displacement time data

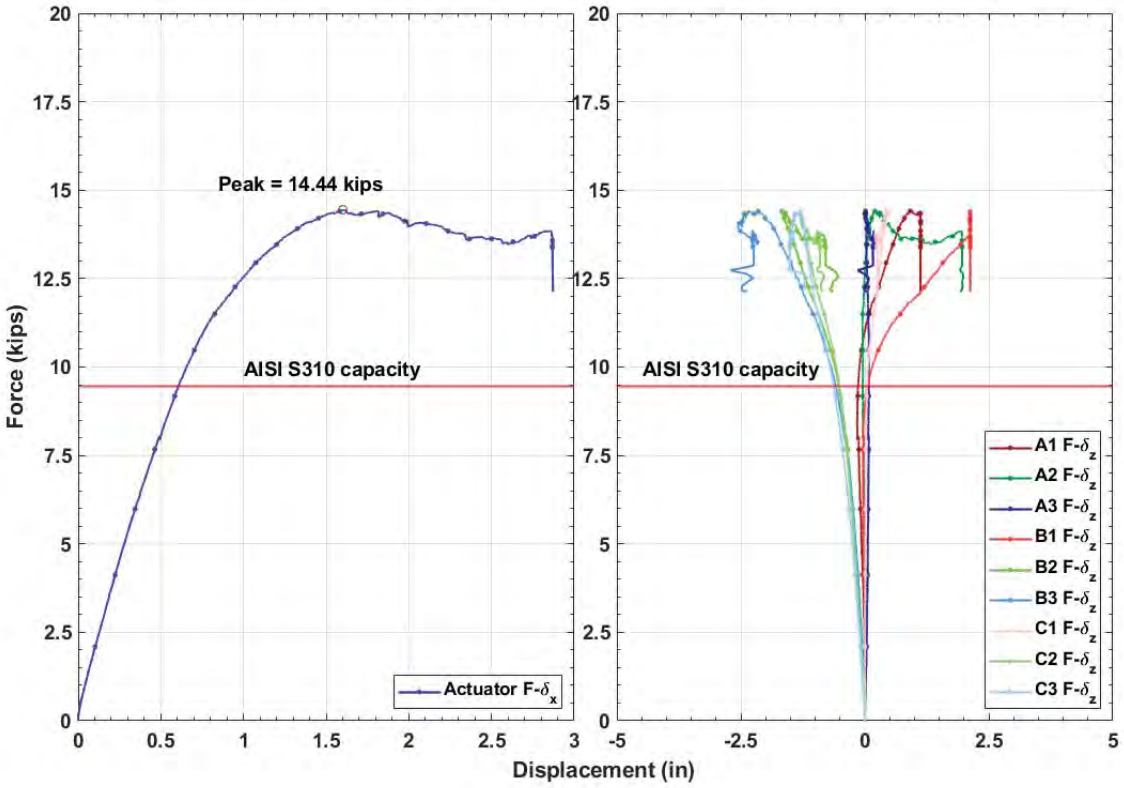

Figure 66: 36-5-R3: Actuator and Sensor force-displacement results

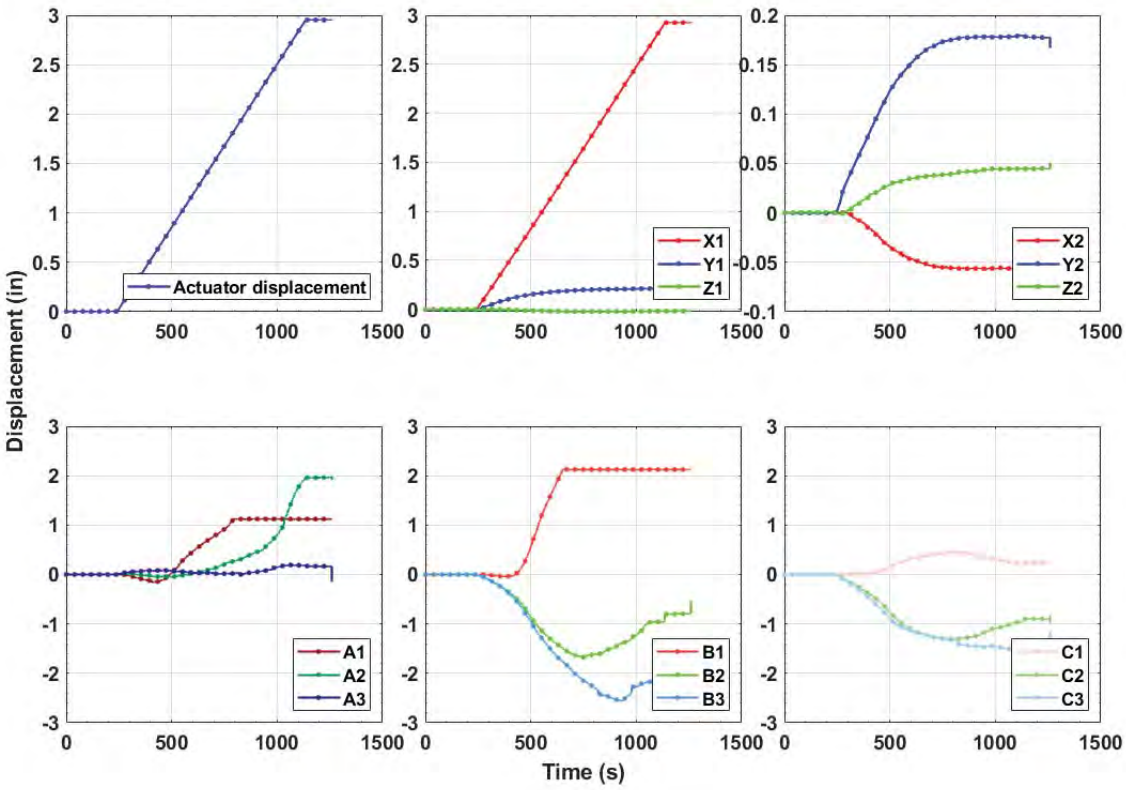

Figure 67: 36-5-R3: Actuator and Sensor displacement time data

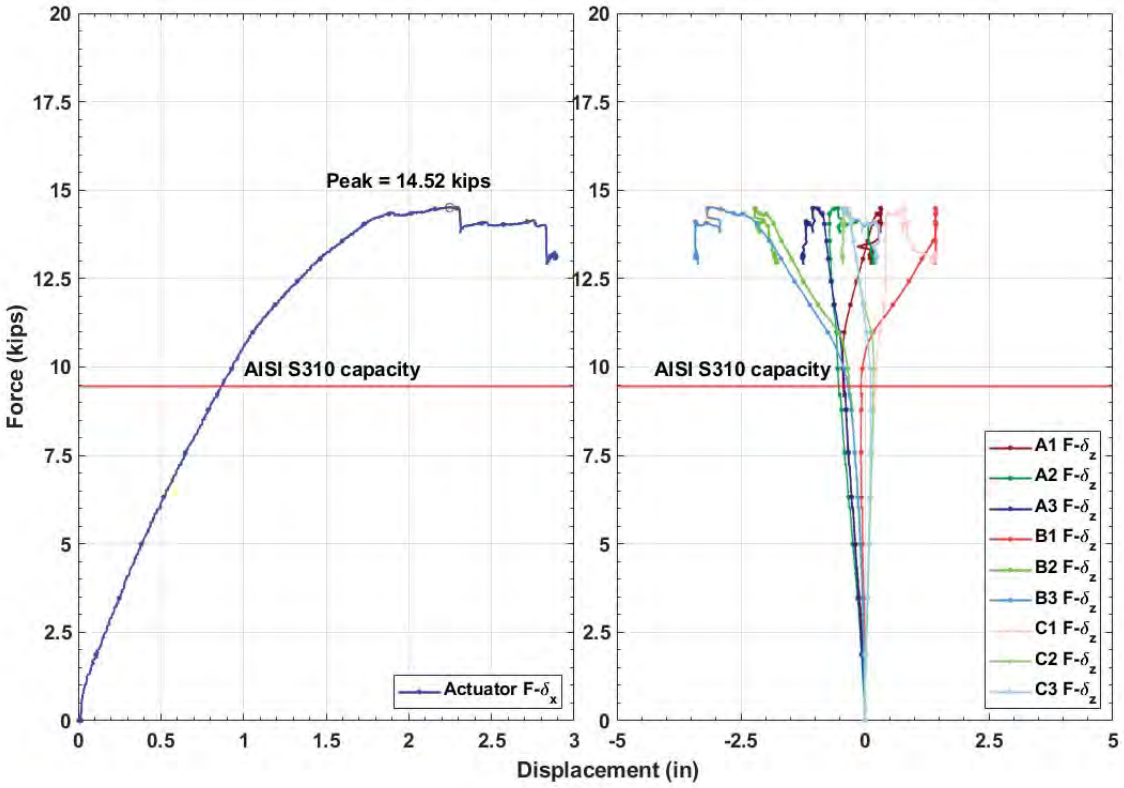

Figure 68: 36-4-R1: Actuator and Sensor force-displacement results

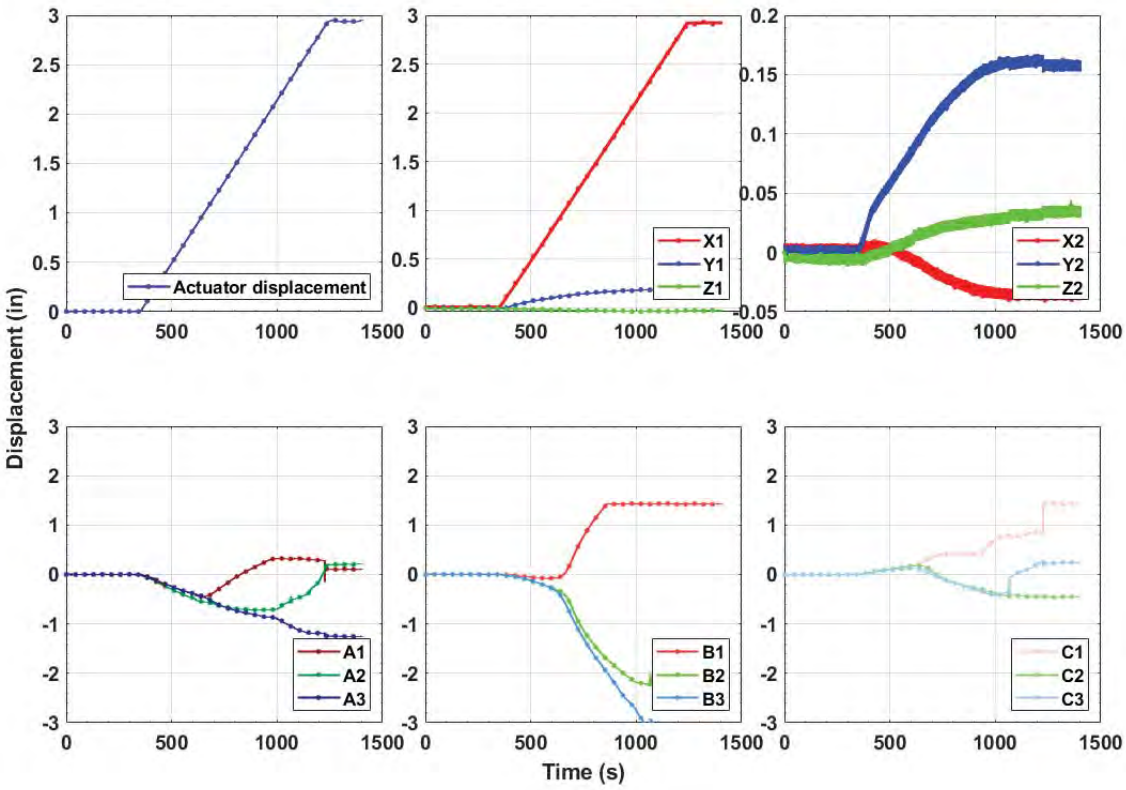

Figure 69: 36-4-R1: Actuator and Sensor displacement time data

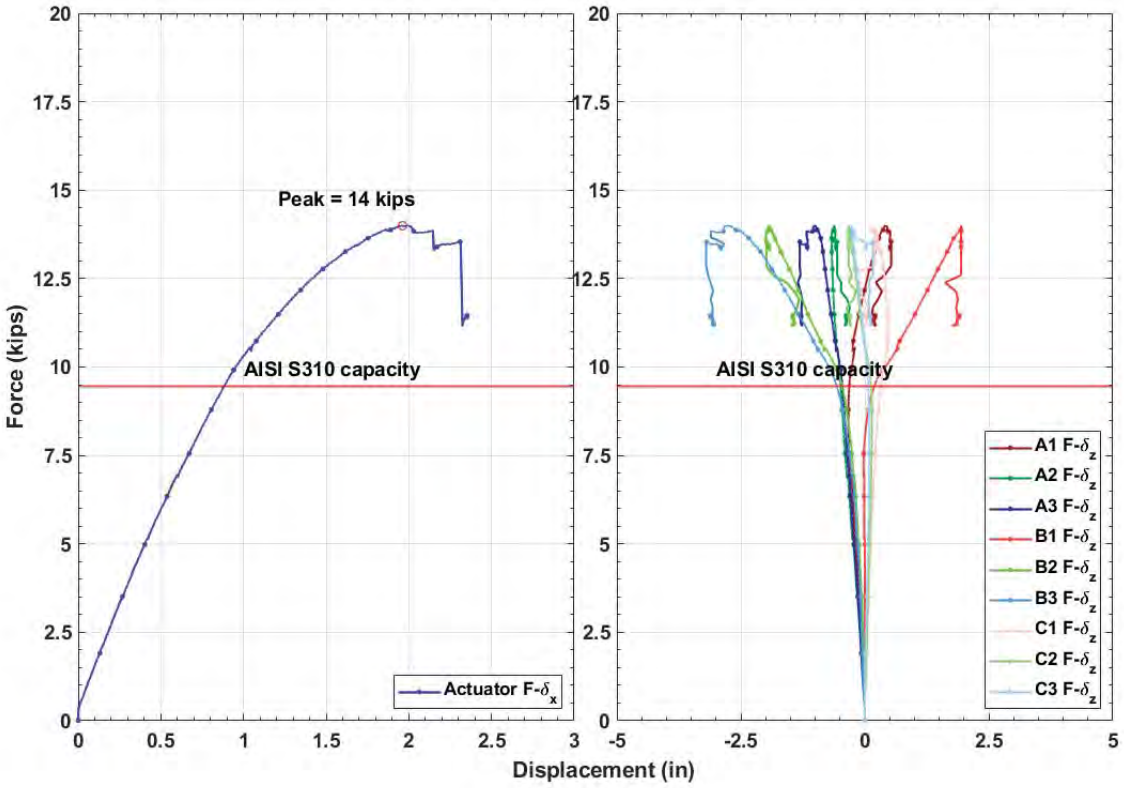

Figure 70: 36-4-R2: Actuator and Sensor force-displacement results

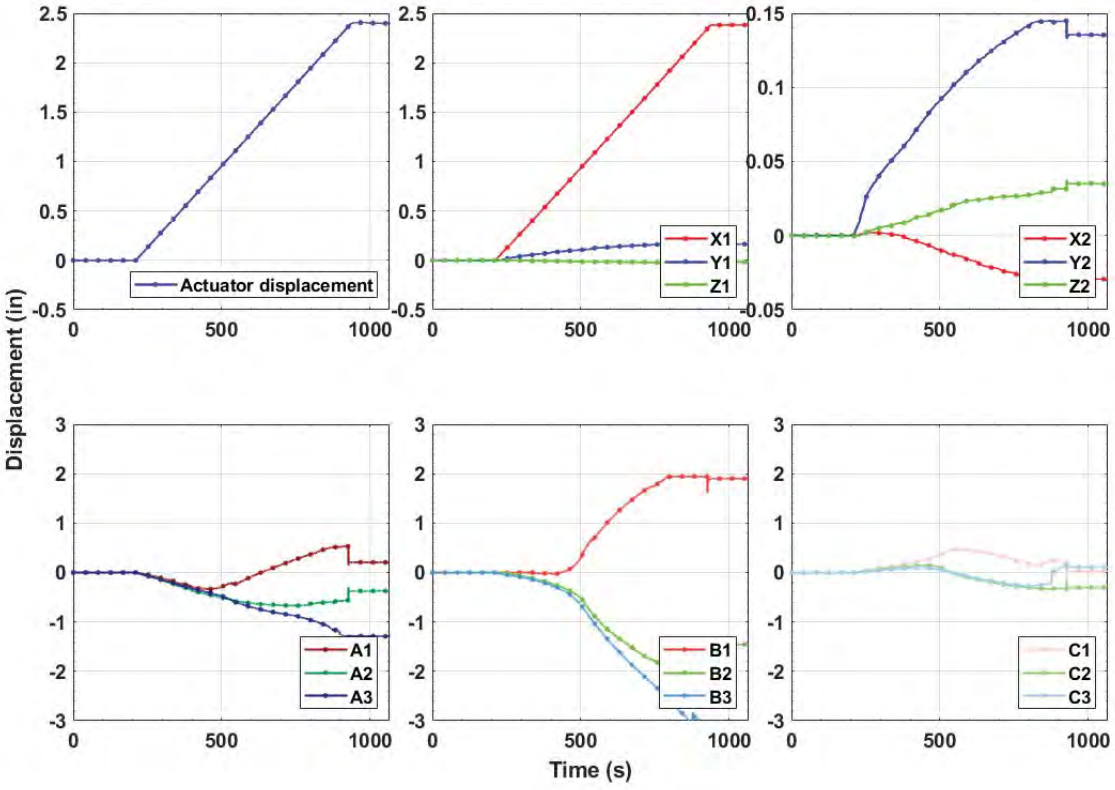

Figure 71: 36-4-R2: Actuator and Sensor displacement time data

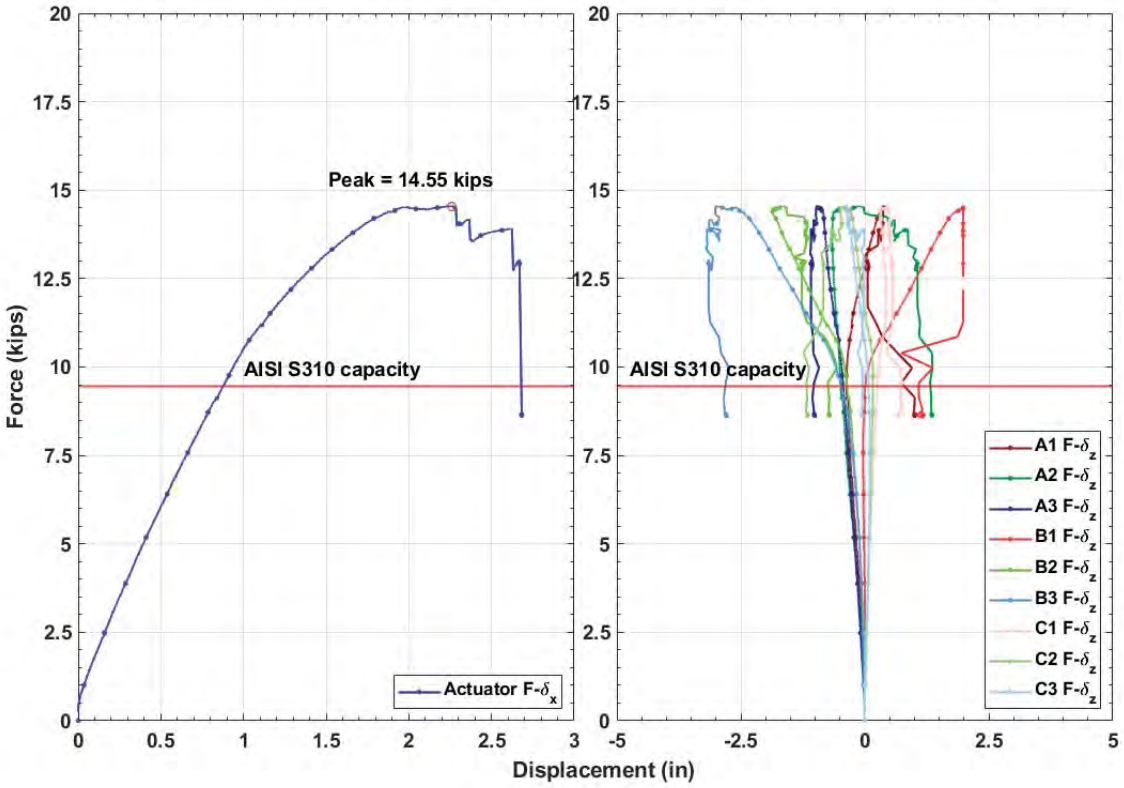

Figure 72: 36-4-R3: Actuator and Sensor force-displacement results

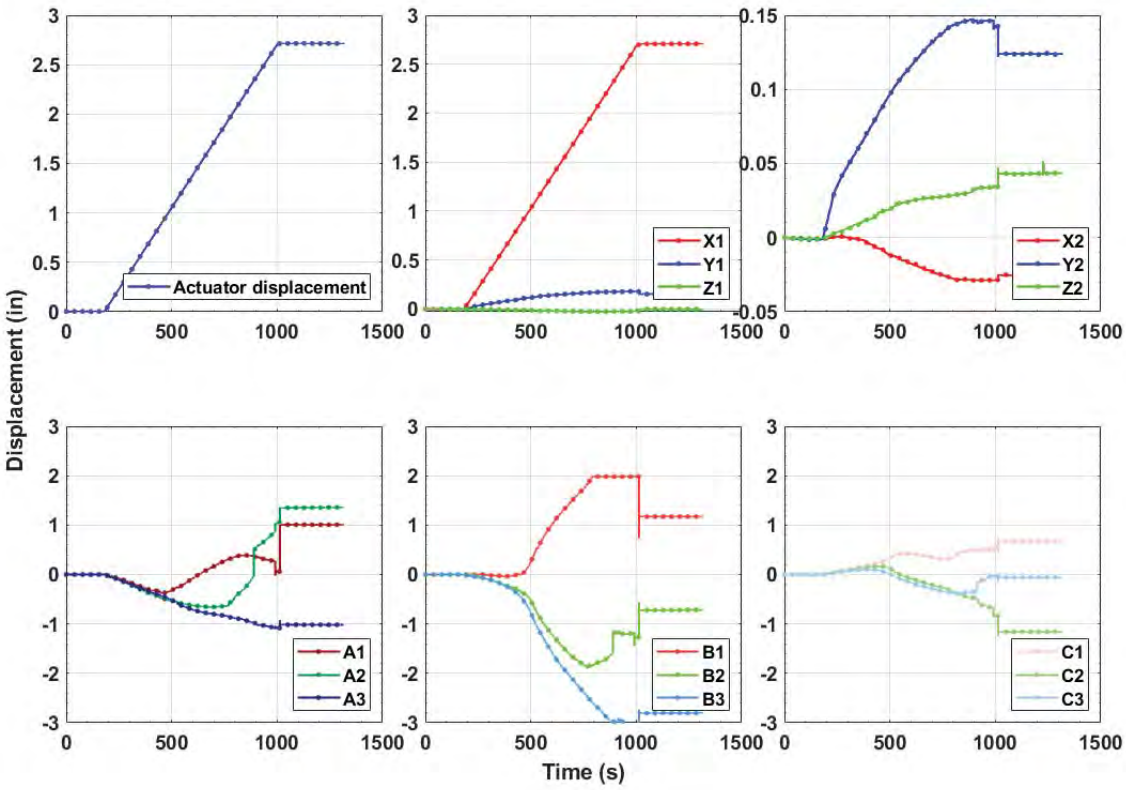

Figure 73: 36-4-R3: Actuator and Sensor displacement time data

D. Appendix D – Estimation of P_{nb}

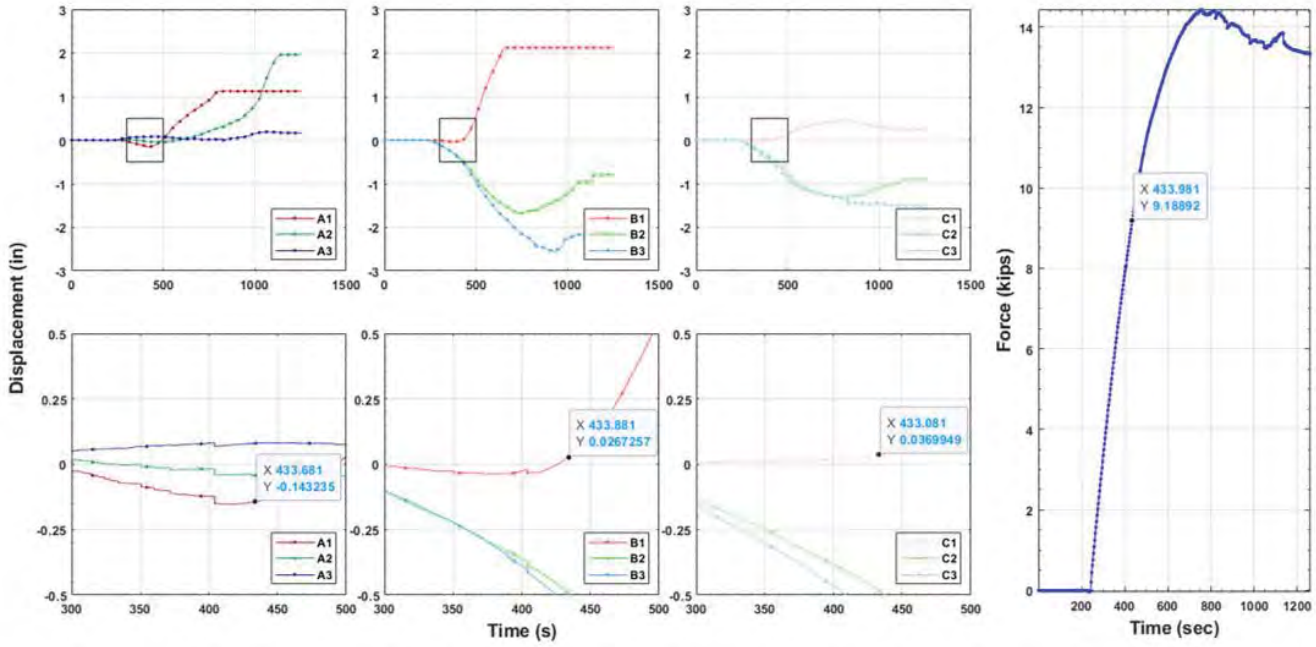

Figure 74: 36-5-R3: Determination of P_{nb}

E. Appendix E – Detailed numerical results

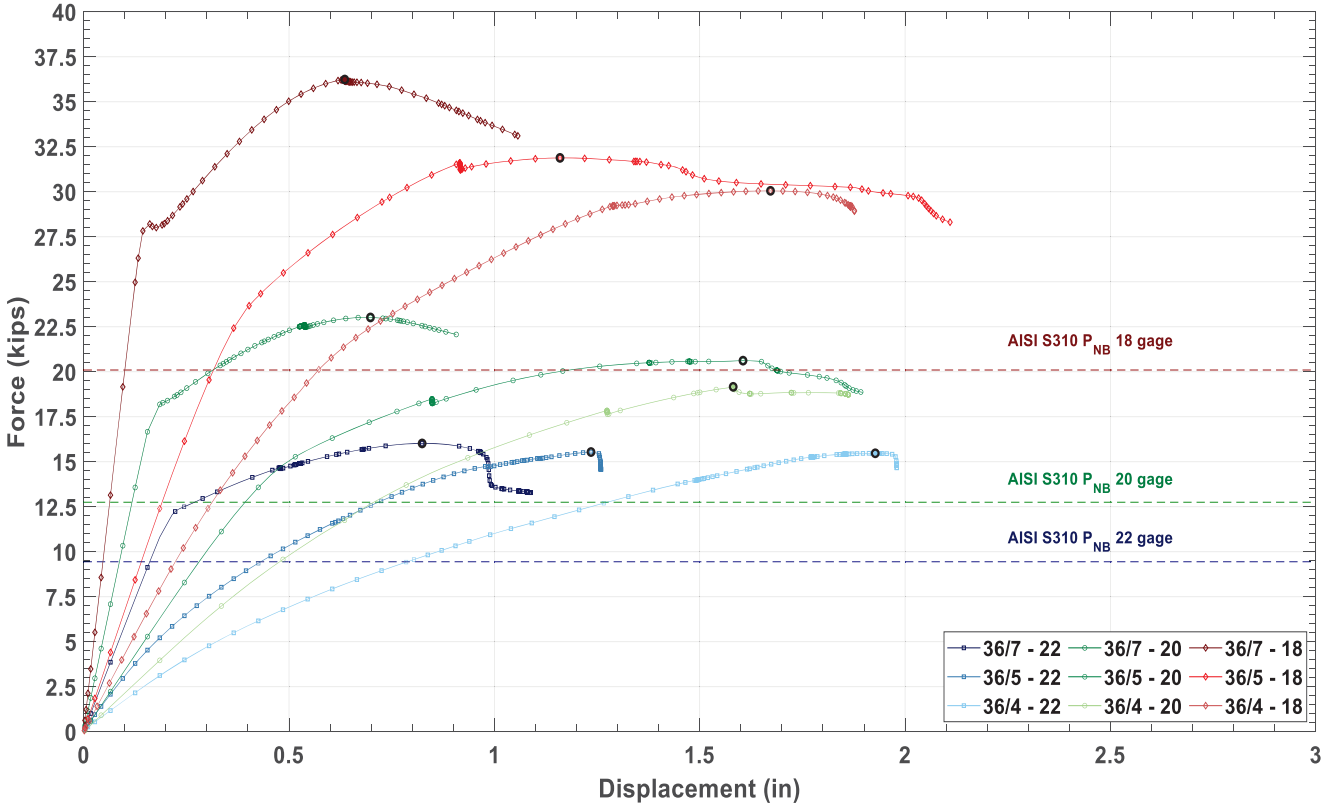

Figure 75: Force vs displacement results for parametric evaluation

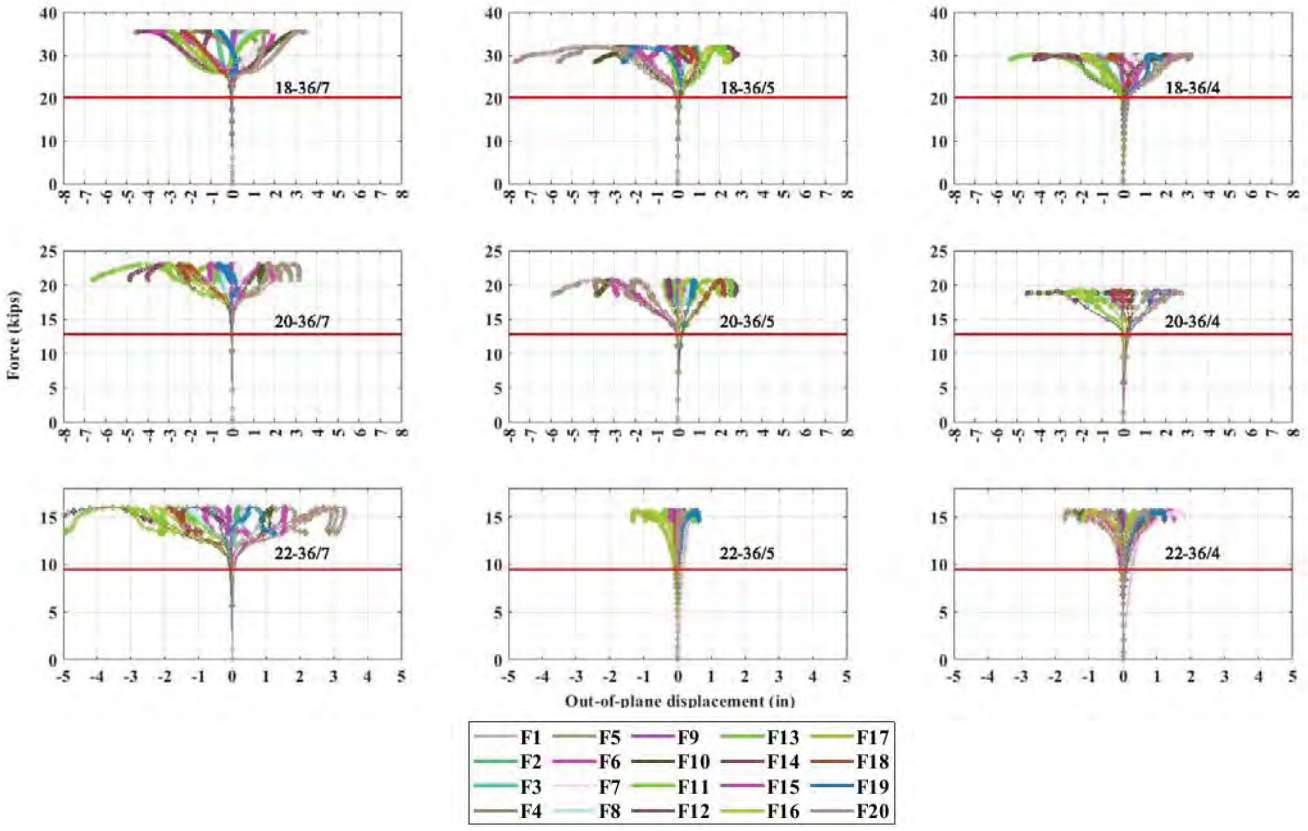

Figure 76: Force vs Mid-span out-of-plane displacement results for parametric evaluation


American
Iron and Steel
Institute


NUCOR®
VULCRAFT


CSC
CANAM STEEL CORPORATION


UMass Amherst
College of Engineering

American Iron and Steel Institute

25 Massachusetts Avenue, NW
Suite 800
Washington, DC 20001

www.steel.org

Research Report RP-23-02